Clean and Secure Energy from Coal

Final Report, Utah Clean Coal Program

Reporting Period Start Date: October 2008

Report Period End Date: August 2014

Principal Authors: Philip Smith, Lincoln Davies, Kerry Kelly, JoAnn Lighty, Arnold Reitze, Geoffrey Silcox, Kirsten Uchitel, Jost O.L. Wendt, Kevin Whitty

Issue date: February 2015

DOE Award Number: DE-NT0005015
Project Officer: David Lang

University of Utah
Institute for Clean & Secure Energy
380 INSCC
155 South, 1452 East
Salt Lake City, UT 84112

DISCLAIMER

ABSTRACT

The University of Utah, through their Institute for Clean and Secure Energy (ICSE), performed research to utilize the vast energy stored in our domestic coal resources and to do so in a manner that will capture CO_2 from combustion from stationary power generation. The research was organized around the theme of validation and uncertainty quantification (V/UQ) through tightly coupled simulation and experimental designs and through the integration of legal, environment, economics and policy issues. The project included the following tasks:

- Oxy-Coal Combustion – To ultimately produce predictive capability with quantified uncertainty bounds for pilot-scale, single-burner, oxy-coal operation.
- High-Pressure, Entrained-Flow Coal Gasification – To ultimately provide a simulation tool for industrial entrained-flow integrated gasification combined cycle (IGCC) gasifier with quantified uncertainty.
- Chemical Looping Combustion (CLC) – To develop a new carbon-capture technology for coal through CLC and to transfer this technology to industry through a numerical simulation tool with quantified uncertainty bounds.
- Underground Coal Thermal Treatment – To explore the potential for creating new in-situ technologies for production of synthetic natural gas (SNG) from deep coal deposits and to demonstrate this in a new laboratory-scale reactor.
- Mercury Control – To understand the effect of oxy-firing on the fate of mercury.
- Environmental, Legal, and Policy Issues – To address the legal and policy issues associated with carbon management strategies in order to assess the appropriate role of these technologies in our evolving national energy portfolio.
- Validation/Uncertainty Quantification for Large Eddy Simulations of the Heat Flux in the Tangentially Fired Oxy-Coal Alstom Boiler Simulation Facility – To produce predictive capability with quantified uncertainty bounds for the heat flux in commercial-scale, tangentially fired, oxy-coal boilers.

TABLE OF CONTENTS

LIST OF FIGURES

LIST OF TABLES

LIST OF ABBREVIATIONS

APS	Aerodynamic Particle Sizer
BFB	Bubbling Fluidized-bed
BJH	Barrett-Joyner-Halenda
BLPI	Berner Low Pressure Impactor
BSF	Boiler Simulation Facility
BT	Black Thunder
CAA	Clean Air Act
CAD	Computer Aided Design
CCS	Carbon Capture and Storage
CEA	Chemical Equilibrium with Applications
CLC	Chemical Looping Combustion
CLOU	Chemical Looping with Oxygen Uncoupling
CWS	Coal-Water Slurry
DO	Discrete Ordinates
DOE	Department of Energy
DOM	Discrete Ordinates Method
DQMOM	Direct Quadrature Method of Moments
DTF	Drop-Tube Furnace
EA	Environmental Assessment
EAB	External Advisory Board
EFG	Entrained-Flow Coal Gasifier
EFR	Entrained Flow Reactor
EIS	Environmental Impact Statement
EPA	U.S. Environmental Protection Agency
FTIR	Fourier Transform Infrared
GHG	Greenhouse Gas
HAB	Height Above Burner
HHV	Higher Heating Values
HPC	High-Performance Computing
HPFFB	High-Pressure Flat-Flame Burner
I/U Map	Input Uncertainty Map
ICSE	Institute for Clean and Secure Energy
IGCC	Integrated Gasification Combined Cycle
LED	Light Emitting Diode
LEFR	Laminar Entrained-Flow Reactor
LES	Large Eddy Simulation
MWIR	Mid-Wave Infrared
NAR	Narrow-Angle Radiometer
NEPA	National Environmental Policy Act
NETL	National Energy Technology Laboratory
NGCC	Natural Gas, Combined Cycle
NIST	National Institute of Standards and Technology
NMR	Nuclear Magnetic Resonance
NSPS	New Source Performance Standard
ODT	One-Dimensional Turbulence
OFC	Oxyfuel Combustor
OFV	Optical Flow Velocimetry

PDF	Pairwise Distribution Function
PIV	Particle Image Velocimetry
PPM	Parts Per Million
PRB	Powder River Basin
PSD	Particle Size Distribution
PSRI	Particulate Solid Research, Inc.
PSV	Particle Shadow Velocimetry
QOI	Quantity of Interest
R&D	Research & Development
RANS	Reynolds-Averaged Navier-Stokes
RBR	Rubblized-Bed Reactor
RFG	Recycled Flue Gas
RMCRT	Reverse Monte Carlo Ray Tracing
SAXS	Small-Angle X-Ray Scattering
SEM	Scanning Electron Microscopy
SKIPPY	Surface Kinetics in Porous Particles Code
SLPM	Standard Liters Per Minute
SMPS	Scanning Mobility Particle Sizer
SNG	Synthetic Natural Gas
TEM	Transmission Electron Microscopy
TF3D	TEM/Fringe3D
TGA	Thermogravimetric Analyzer
UCTT	Underground Coal Thermal Treatment
V/UQ	Validation and Uncertainty Quantification
WARs	Wide-Angle Radiometer

EXECUTIVE SUMMARY

The University of Utah, through their Institute for Clean and Secure Energy (ICSE), performed research to utilize the vast energy stored in our domestic coal resources and to do so in a manner that will capture CO_2 from combustion from stationary power generation. The research was organized around the theme of validation and uncertainty quantification (V/UQ) through tightly coupled simulation and experimental designs and through the integration of legal, environment, economics and policy issues. The work was organized into the following tasks.

Oxycoal studies. The objective of this task is to move toward the development of a predictive capability with quantified uncertainty using Large Eddy Simulations (LES) with Direct Quadrature Method of Moments (DQMOM) bounds for pilot-scale, single-burner, oxy-coal operation. The combination of simulation development and validation experiments was designed to lead to predictive tools for the performance of existing air fired pulverized coal boilers that have been retrofitted to various oxy-firing configurations. The simulations focused on understanding the factors affecting flame stability while the experiments on the University of Utah's OxyFuel Combustor (OFC) focused on the effects of different coals, operating conditions, and oxygen input configurations on flame stability. The simulation results suggested that wall temperature had a large effect on flame stability, while the experimental results suggested that oxygen partial pressure had a large effect on flame stability. Several optical diagnostic techniques were developed and refined to assist with the collection of validation data. The techniques included Particle Image Velocimetry (PIV) for identification of velocity fields, Particle Shadow Velocimetry (PSV) for identification of particle shape and size, and a high-speed visible imaging method for the simultaneous measurement of gas velocity, soot temperature, soot concentration and spectral heat flux. In support of the simulation efforts, the investigators identified the importance of steam and CO_2 gasification under oxy-combustion conditions and developed a detailed model for incorporation into the LES simulation. The effects of oxy-firing on particle formation and ash partitioning were also evaluated experimentally at the lab and pilot scale. At the pilot scale, various recycled flue gas (RFG) options and various RFG amounts were evaluated to identify the effects on ash aerosol particle size distributions (PSDs) and elemental compositions.

In addition, the task included novel research results related to oxy-combustion in circulating fluidized beds at the pilot and lab scale. For the pilot-scale CFB, the SO_2 emissions were substantially higher under the oxy-fired conditions in terms of concentration, compared to the laboratory-scale studies. The reason for the higher SO_2 concentrations during oxy-firing at pilot-scale were due to the use of flue-gas recycle, which allowed accumulation of sulfur species in the main combustion zone. The project also included an evaluation of limestone sulfation mechanisms under air-firing and oxy-firing conditions.

Gasification studies. The gasification activities focused on developing simulation tools for pressurized entrained-flow coal gasifiers (EFGs). The overall gasifier simulation tools combined submodels for fluid flow and heat transfer with fundamental understanding of the chemical processes that take place as coal particles are converted to synthesis gas. The fluid-flow models integrated several submodels into our one-dimensional turbulence model to address the fate of coal particles in combustion/gasification processes. The simulation activities also included development of the ARCHES tool for use in gasification simulations, and the collection and analysis of BYU and CANMET gasifier experimental data. Using an equilibrium model, three parameters were selected for the V/UQ evaluation matrix: O_2/coal feeding ratio, coal slurry concentration, and heat loss fraction. The refined heat-transfer model expanded the radiative heat-transfer algorithms in the University of Utah LES codes to include coal particles under entrained coal gasification conditions. This was accomplished by enhancing the legacy Discrete Ordinates Method (DOM) to model the combined effect of the gas-phase and particle-phase absorption coefficients.

Experimental efforts included smaller scale kinetic and char-slag transition experiments as well as collection of larger scale EFG data. Two aspects of coal conversion were considered (a) kinetics, which were developed for several coals in a high-pressure flat-flame burner (HPFFB) and (b) the char-slag transition for different coals, which indicated that at conversions higher than roughly 95%, the material is completely coalesced, resulting in limited accessibility of the remaining carbon. In an effort to obtain more detailed entrained EFG validation data, the University of Utah's EFG was refined to include a new feeder, an efficient, reliable coal-water slurry injector and a safe probe for sampling the gas environment in the reactor during operation. Successful operation of the University of Utah's gasifier was accomplished at a range of operating conditions with various solid fuels. The stability and duration of these runs increased substantially as experience with the system increased, as well as with improvements in the injector design.

Chemical Looping Combustion (CLC). This task focused on four complementary efforts with an emphasis on chemical looping with oxygen uncoupling (CLOU). First was the development of process and economic models to optimize important design considerations, such as oxygen carrier circulation rate, temperature, and residence time. This incorporated literature as well as experimental results from the other subtask. The results highlighted the importance of the copper carrier's lifetime. Second was the development of high-performance simulation capabilities for fluidized beds and the collection, parameter identification, and preliminary verification/uncertainty quantification. The simulation results compared favorably with the experimental results from the bubbling fluidized-bed (BFB). Third was the exploration of operating characteristics in the laboratory-scale bubbling bed reactor, with a focus on the oxygen carrier performance, including reactivity, oxygen carrying capacity, attrition resistance, resistance to deactivation, cost and availability. These laboratory-scale studies determined that both oxidation and decomposition (O_2 release) of the copper oxygen carrier depend on the so-called "driving force" associated with the difference between the O_2 partial pressure in the reactor environment and the equilibrium O_2 partial pressure. In addition, the investigators evaluated the attrition propensity of a variety of carriers, and the carriers produced by freeze granulation or impregnation of preformed substrates displayed the lowest rates of attrition. Fourth was the identification of kinetic data for copper-based oxygen carriers as well as the development and analysis of supported copper oxygen carrier material.

*Underground Coal Thermal Treatment***.** The goal of this task was to develop sufficient data to determine if underground coal thermal treatment (UCTT) is a feasible technology. The UCTT process slowly heats coal in the ground and produces substitute natural gas and liquid transportation fuels while leaving much of the coal's carbon in the ground. This process has the potential to convert coal to a high-efficiency, low-greenhouse gas (GHG) emitting fuel. The UCTT experimental team focused on experiments at two scales, bench-top and slightly larger, to develop data to understand the feasibility of a UCTT process. They found hydrogen did indeed partition to the gas and liquid products, while carbon tended to remain in the char. The simulation studies focused on the investigation of heat transfer and yield models, as well as various seam thicknesses, heater configurations and heater temperatures. These studies suggested the importance of developing an accurate yield model for the low temperatures. The CO_2 storage studies focused on developing adsorption isotherms on coals treated to 325, 450, and 600°C with slow heating rates for three types of coals. The study indicated that adsorptive capacity for the coals increased with treatment temperature and that coals treated to 325°C showed less or similar capacity to the untreated coals.

Mercury. Bench-scale experiments were conducted to understand the fate and speciation of mercury in oxy-coal combustion conditions. In the absence of sulfur dioxide, the oxy-firing environment caused a remarkable increase in oxidation of mercury by chlorine. The presence of 500 ppm SO_2 caused a dramatic decline in the levels of oxidation at all oxy-fired conditions examined.

Environmental, Legal, and Policy Issues. Despite the acknowledged inevitability of climate change and the attendant need for effective mitigation strategies, carbon capture and storage (CCS) has yet to gain much traction in the United States. The policy tasks focused on the role of federal and state regulation of CCS, assessing existing barriers to CCS deployment as prioritized by the CCS community, and examining how potential CCS regulatory models might address those barriers. The task identified four primary barriers to CCS deployment: (1) cost; (2) lack of a carbon price; (3) liability; and (4) lack of a comprehensive regulatory regime. The analysis of potential CCS regulatory models determined that: (1) a CCS-specific standard that incorporated flexibility, such as a technology performance standard or a particular type of market-based regulation, likely would promote CCS diffusion; and (2) in order to speed CCS deployment, any CCS diffusion policy should be combined with other measures, such as liability limits and a comprehensive CCS regulatory regime.

Validation/Uncertainty Quantification for Large Eddy Simulations of the Heat Flux in the Tangentially Fired Oxy-Coal Alstom Boiler Simulation Facility. The objective of this task was to produce predictive capability with quantified uncertainty bounds for the heat flux in commercial-scale, tangentially fired, oxy-coal boilers. Validation data came from the Alstom Boiler Simulation Facility (BSF) for tangentially fired, oxy-coal operation. This task brought together experimental data collected under Alstom's DOE project for measuring oxy-firing performance parameters in the BSF with this University of Utah project for LES and V/UQ. The Utah work includes V/UQ with measurements in the single-burner facility where advanced strategies for O_2 injection can be more easily controlled and data more easily obtained. The BSF and OFC simulations were consistent with the experimental results. Both simulation subtasks were able to identify key parameters affecting heat flux. Supporting the OFC simulations were measurements of heat flux made with a mid-wave infrared (MWIR) camera and with a high-speed, visible camera. These advanced measurements compared favorably with coincident radiometer measurements. In addition numerous replicate experiments were performed on the OFC to assess experimental uncertainty.

Several tasks associated with the University of Utah's Oil Sands and Oil Shale Program (DE-FE0001243) were managed under the University of Utah's Clean and Secure Energy from Coal Program (DE-NT0005015) during phase one of the Coal Program. The Oil Sands and Shale Program addressed barriers to oil sand and shale deployment through a research program that ranged from the atomistic level to full-scale reservoir simulation and encouraged coupling and integration among the various scales. It also addressed carbon capture and water issues for these resources. The final project reporting for these tasks is being included under the Oil Sands and Shale Program.

INTRODUCTION

The University of Utah, through their Institute for Clean and Secure Energy (ICSE), performed research to utilize the vast energy stored in our domestic coal resources and to do so in a manner that will capture CO_2 from combustion from stationary power generation. The research was organized around the theme of validation and uncertainty quantification (V/UQ) through tightly coupled simulation and experimental designs and through the integration of legal, environment, economics and policy issues. The project included the following research areas and associated objectives:

- Oxy-Coal Combustion – To ultimately produce predictive capability with quantified uncertainty bounds for pilot-scale, single-burner, oxy-coal operation. This research brings together multi-scale experimental measurements, advanced diagnostics and computer simulations. The efforts shall focus on ignition and coal-flame stability under oxy-coal conditions. This predictive tool developed under this effort will form the basis for application to full-scale, industrial burner operations.
- High-Pressure, Entrained-Flow Coal Gasification – To ultimately provide a simulation tool for industrial entrained-flow integrated gasification combined cycle (IGCC) gasifier with quantified uncertainty. This project's target is to develop a prototype simulation tool, perform preliminary uncertainty quantification on a pilot-scale gasifier, and to begin to predict heat transfer by radiation and convection, coal conversion, soot formation, and synthesis gas composition with quantified uncertainty.
- Chemical Looping Combustion (CLC) – To develop a new carbon-capture technology for coal through CLC and to transfer this technology to industry through a numerical simulation tool with quantified uncertainty bounds. The specific research target for this project is to quantitatively identify reaction mechanisms and rates, explore operating options with a laboratory-scale bubbling bed reactor, develop process models and economics and demonstrate and validate simulation tools for a pilot-scale fluidized bed. This task will focus primarily on CuO/Cu_2O.
- Underground Coal Thermal Treatment – To explore the potential for creating new in-situ technologies for production of synthetic natural gas (SNG) from deep coal deposits and to demonstrate this in a new laboratory-scale reactor. The systems concept for the SNG is to use this premium fuel produced from coal in natural gas, combined cycle (NGCC) power generation or compressed and used as a transportation fuel (compressed natural gas). UCTT leaves large portions of the carbon from the coal in the ground. The research will focus on the development of simulation tools, the collection of process thermo-chemical parameters, and the development of complementary CO_2 absorption isotherms.
- Mercury Control – To understand the effect of oxy-firing on the fate of mercury.
- Environmental, Legal, and Policy Issues – To address the legal and policy issues associated with carbon management strategies in order to assess the appropriate role of these technologies in our evolving national energy portfolio.
- Validation/Uncertainty Quantification for Large Eddy Simulations of the Heat Flux in the Tangentially Fired Oxy-Coal Alstom Boiler Simulation Facility – To produce predictive capability with quantified uncertainty bounds for the heat flux in commercial-scale, tangentially

fired, oxy-coal boilers. This task brought together experimental data collected under Alstom's DOE project for measuring oxy-firing performance parameters in the BSF with this University of Utah project for large eddy simulation (LES) and (V/UQ) as well as experimental measures in the University of Utah's Oxyfuel Combustor (OFC).

This final report summarizes the activities and key findings of this project. Additional detail about each research area and the associated tasks and subtasks can be found in the corresponding topical reports. Links to all of these reports are available online at
http://www.uc3.utah.edu/publications;jsessionid=CBB48879A0FCBCD8E3A5CCE0A302BE2C

METHODS

Task 1.0 – Project Management

Project management activities included financial management, reporting, and coordination with the program manager.

Task 2.0 – Education, Outreach and the Advisory Board

This task focused on the dissemination of project results, on industrial, academic and public outreach, student research opportunities as well as instituting an External Advisory Board (EAB) and considering their recommendations.

Task 3.0 – Oxycoal Studies

This report provides highlights of the project's oxycoal studies. Additional detail can be found in Wendt et al. (2011, 2014).

Subtask 3.1 – Oxy-Coal Combustion Large Eddy Simulations

In order to perform reliable LES of oxycoal flames, several improvements to the LES code were needed including (a) the implementation of particle modeling capabilities using DQMOM, (b) the inclusion of all the physical models related to coal particle combustion within the DQMOM approach, and (c) the coupling of the particle and particle-combustion models with the gaseous-phase models. Work under subtask 3.2 showed that stability of coal flames was sensitive to many factors such as coal type, inlet stream composition, temperature and velocities.

The simulations predicted flame stability in the University of Utah's OFC using a co-axial Type 0 (zero swirl) burner with a transport stream and pulverized coal in the center and a secondary stream in the annular sleeve. The coal employed was Utah bituminous pulverized coal. Both the primary and secondary streams were O_2/CO_2 mixtures, and the overall oxygen concentration was maintained to 40 vol%. In this study, we are interested in a specific set of experiments where the secondary stream preheat temperature was set to 544 K and the primary P_{O2} varied from 0% to 20.9%. Variations in primary P_{O2} were obtained by transferring oxygen flows from the primary to the secondary stream, with only small effects on jet momentum.

Sources of uncertainty in the operating conditions were identified during those experiments and included the wall temperature, which was measured with a thermocouple located on behind the wall heater. The reported wall temperature value of 1283 K is therefore the value measured behind a 2 inches thick layer and not the wall temperature inside the furnace. The later one could indeed be much higher. An infrared camera was used to determine the wall temperature inside the University of Utah furnace in other experiments with similar operating conditions and measured wall temperatures at about 1800 K. In addition, thermocouple measurements can be inaccurate and have up to 50K uncertainty. The primary stream was injected at room temperature, and its temperature was assumed to be 305 K but was not measured directly. Operators noticed that the tip of the burner was glowing red after the experiments. The burner penetrates inside the furnace by about 10 cm and its tip is therefore exposed to a high radiative flux. As a result, it is possible that the burner transfers heat to the primary stream and the coal particles, which would result in a higher primary stream temperature.

Simulation error or uncertainty arises from four types of uncertainties:

- Model uncertainty, or error in the mathematical description of the physical process being modeled. This error includes uncertainty in the parameters used in these models.
- Uncertainty in boundary conditions. This uncertainty derives from the uncertainty in the inputs and boundary conditions used for the simulation.
- Numerical error (verification error). This error arises from the numerical approximations used in producing the simulation (i.e. grid resolution, discretization error, convergence error, etc.)
- Experimental error in the validation data.

The experiments (subtask 3.2) suggested that the primary oxygen concentration has an influence on the flame stand-off distance, and this was therefore chosen as a parameter of interest. Two other parameters were chosen: the wall temperature T_{wall} and the temperature of the primary stream T_{pri}. The range associated with each parameter is reported in Table 1.

Table 1. Chosen parameters and their ranges.

Parameter	Range
Wall temperature (T_{wall})	1200 – 1800 K
Primary stream temperature (T_{pri})	305 – 544 K
Primary oxygen partial pressure ($P_{O2,pri}$)	0 – 20.9 %

The computational domain is a cylinder of diameter 0.6 m and length 0.9 m. The domain is decomposed into a Cartesian mesh with a cell size of 1.7 mm. The primary and secondary inlets are located at the center of the X=0 face, and outlet boundary conditions are applied at the X=0.9 m face. All other boundaries are set as walls with a fixed and uniform temperature T_{wall}. Each of the 13 simulations was run for 24 hours on 1,500 CPUs with time steps of about 9 microseconds, which resulted in a total simulation time of about 1.25 s. Time-averaging was done on the last second of data. The coal particles are injected with the primary stream at a mass flow rate of 4.84 kg/h and are assumed to have the same temperature and velocity as the gas phase at the inlet. The initial coal particle density is 1300 kg/m^3.

Subtask 3.2 – Near-Field Aerodynamics of Oxy-Coal Flames with Directed Oxygen and Minimum Flue Gas Recycle

This task focused on: (1) understanding the effects of preheat temperatures, oxygen concentration and coal composition on axial flame stability under oxy-coal combustion conditions, (2) understanding how advanced O_2 distribution strategies for co-axial burners in the University of Utah, 100 kW OFC might affect flame stand-off distances and flame stability, and (3) contributing to the V/UQ efforts of subtask 3.1.

The experiments were performed in the OFC (Figure 1). Flame stability was determined using photoimaging in partnership with subtask 3.3. Two types of coal were used in this research: Utah Skyline bituminous and Illinois #6 bituminous. The OFC studies of coal composition were supported by the thermogravametric analyzer (TGA) experiments and nuclear magnetic resonance (NMR) analyses.

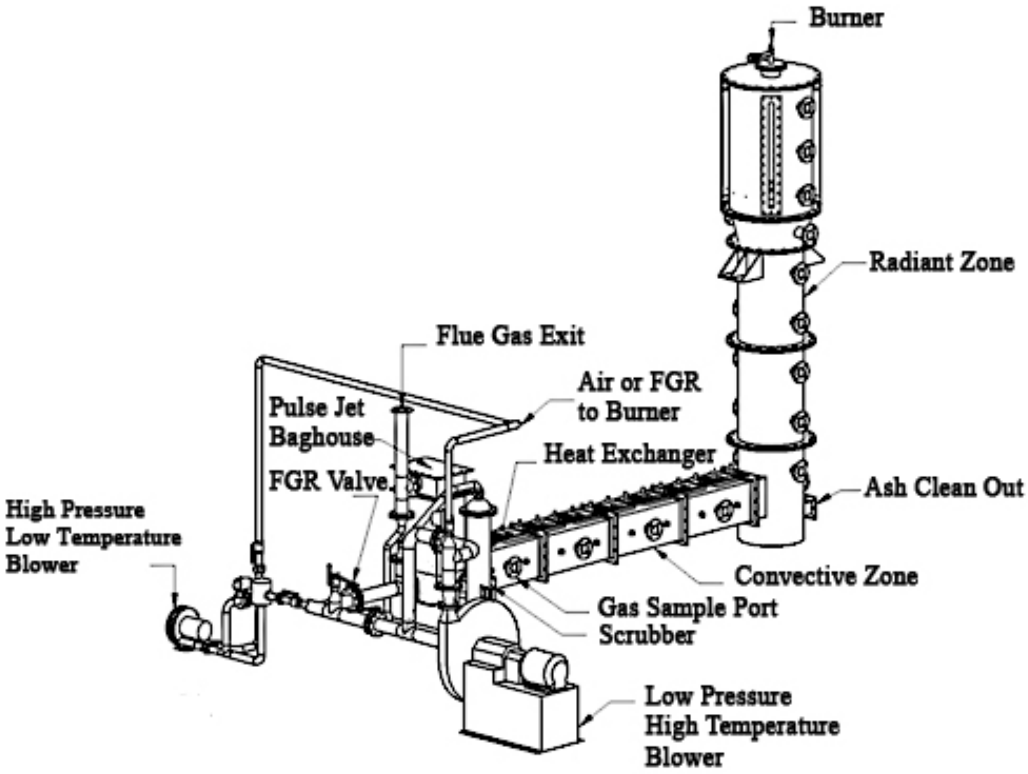

Figure 1. Oxy-fuel combustor.

Several types of burners were employed: (1) simple coaxial burners with only one annulus and two streams for studies of flame stability, and (2) triple concentric burners for studying directed pure oxygen. The triple concentric burners allowed a primary pulverized coal stream transported by CO_2 to exit from one opening, a pure O_2 stream to exit from another opening, and a stream containing both O_2 and CO_2 to exit from the third opening. The pure oxygen stream is denoted as the directed oxygen stream and was dedicated to contain a specific percentage, up to 100%, of all the oxygen required for combustion for the combustion operating condition being investigated. The primary stream is defined as the stream carrying pulverized coal particles into the chamber and, as noted above, contained only CO_2, with no oxygen. Directed oxygen and transport streams were at room temperature. The secondary stream was a mixture of O_2 and CO_2, and played a significant role in moderating the combustion temperature as well as aerodynamically controlling entrainment of the flame jet. Two directed-oxygen combustion configurations were examined. In Configuration A the primary coal stream was at the center. The directed oxygen stream exited from the inner annulus, and the secondary O_2/CO_2 stream was in the outside annulus. In Configuration B, the directed oxygen stream was at the center, and the primary coal stream was at the middle annulus and the secondary O_2/CO_2 stream at the outside annulus.

Subtask 3.3 – Advanced Diagnostics for Oxy-Coal Combustion

To fully understand the behavior of turbulent oxy-coal flames and to validate oxy-coal simulation models, accurate experimental data are needed on the details of the flow field and dynamics of pulverized-coal flames at multiple scales. A non-intrusive laser diagnostic technique, PIV, was evaluated for application to the OFC. Due to the limited resolution of the method when applied to coal flames, the investigators concluded that the PIV was not feasible for the OFC application.

The investigators also developed and evaluated PSV. To develop the PSV setup, a high-speed, high-power light emitting diode (LED) and long-range, high magnification microscope were purchased. A Matlab-based software framework was developed to determine the particles size, velocity, and shape. Testing the PSV method with glass beads of a known size showed that PSV slightly over-estimated the size, compared to the nominal size. However, the approximation was still good.

The PSV method was optimized for the OFC flame with a high-efficiency diffuser, and the Matlab analysis code was further refined to address the noisier images produced by the OFC.

In addition to PSV, the investigators evaluated the use of high-speed video to extract velocity fields from subsequent scalar image pairs of flows. This method is known as optical flow velocimetry (OFV). The advantage of this method is that the high-speed video has a much larger field of view than the PSV or PIV methods.

Subtask 3.4 – Oxy-Coal Combustion in Circulating Fluidized Beds

Oxy-fired pilot-scale circulating fluidized bed experiments were carried out in the University of Utah's pilot-scale CFB. In parallel, bench-scale experiments were carried out under subtask 3.5 to explore the behavior of SO_2 emissions at smaller scale and under more controlled conditions. The experimental setups used for the bench-scale experiments and the pilot-scale experiments are described in detail in Wendt et al. (2012).

Subtask 3.5 – Single-Particle Oxy-CO_2 Combustion

Single-particle CFB

This subtask explores the limestone sulfation mechanisms under air-firing (i.e., O_2/N_2) and oxy-firing (i.e., O_2/CO_2) conditions. The effects of CO_2 concentration on limestone calcination and carbonation were also investigated to help explain the observations under oxy-firing conditions. In addition, the effects of temperature, CO_2 concentration, and heating rate on CO_2 capture capacity of limestone during looping cycles were evaluated.

The sulfation experiments were performed in a bench-scale BFB reactor. The BFB reactor is a vertical, cylindrical, and stainless-steel furnace with a combustion chamber length of 771 mm and an inner diameter of 44 mm. A 2 mm thick perforated plate distributor with 60 holes was placed in base of the reactor. The gas flows were controlled by digital mass flow controllers and were premixed before being introduced into the furnace. The bed was heated by an electrical furnace to reach the desired reaction temperature. The temperatures of bed materials, furnace wall, and gas phase were measured by K-type thermocouples connected to a digital temperature controller. Downstream from the reactor, any unburned entrained fine particles and soot were removed by a glass wool filter. Then, the gas stream was analyzed by a Magna-IR^{TM} 550 Fourier transform infrared (FTIR) spectrometer. Before each test, the preheated furnace was purged by N_2/O_2 or CO_2/O_2 to maintain consistent reaction conditions. For each experiment, a background spectrum of the purged gas was collected after the combustion diluent was changed.

In a typical experiment, 1.0 g of limestone was charged into the reactor containing approximately 300 g of bed material (zirconium silicate). The limestone was then calcined under a N_2 atmosphere. Subsequently, a sulfur-containing gas stream (such as $N_2/O_2/SO_2$ or $CO_2/O_2/SO_2$) was charged into the reactor. Note that the SO_2 concentration was maintained identical in all the runs. The total reaction time was approximately 1 h. After reaction, the sulfated limestone samples were mounted and polished gently for scanning electron microscopy (SEM) analysis. Three operating temperatures were considered 765, 835, and 874°C.

A TGA–MS Q600 instrument was used to investigate the effects of temperature and CO_2 concentration on limestone calcination and carbonation, as well as the parametric effects of temperature, In limestone looping experiments, varying CO_2 concentrations (20%, 50%, and 100% in N_2) were provided by different calibration gas cylinders.

Single-particle char oxidation

The subtask focused on development of a detailed model of a single-char particle oxidation, and in particular to assess the impact of CO_2 and steam gasification reactions on the oxy-combustion of coal chars.

The investigators also evaluated two simplified char-combustion models and compared these to the detailed model. The most detailed and physically accurate model considered in this work is the Surface Kinetics in Porous Particles code (SKIPPY), also known as a continuous-film model. SKIPPY solves the steady-state mass, species, and energy conservation equations for a reacting porous particle and its reacting boundary layer. From this solution, SKIPPY predicts species concentrations and temperatures within the pores of the char, at the outer surface of the char, and within the boundary layer surrounding the char. Both heterogeneous (gas-solid) and gas-phase chemical reactions are considered. SKIPPY was compared to a single-film model and a dual-film model. The single-film model assumes there are no reactions in the boundary layer. A dual-film model assumes that there is an infinitely thin flame sheet at a point in the boundary layer that converts CO to CO_2 and H_2 to H_2O. At all other points in the boundary layer, the gases are unreactive. In contrast to a classical double-film model, the oxygen is not necessarily completely consumed in the boundary layer, and O_2, CO_2 and H_2O each react and consume the solid carbon.

Finally, an entrained flow reactor (EFR) was used to make measurements of single-particle temperatures under a wide range of conditions for three coal chars. The chars were generated in the University of Utah's Drop-Tube Furnace (DTF). The furnace was operated at 1200 °C while flowing 15 standard liters per minute (SLPM) nitrogen with approximately 1 vol-% oxygen to burn off any tars that might be generated during devolatilization. Three coals were considered: an Illinois #6, a low-sulfur western bituminous coal from the Utah Skyline mine, and Black Thunder sub-bituminous coal from the Powder River Basin (PRB). The char was then oxidized in environments that ranged from 24-60% O_2, 10-14% H_2O, with N_2 or CO_2 serving as the diluent. Collected chars were also analyzed for burnout and surface area. Kinetic parameters were found for the simplified model to fit the experimental data, for each of the coal chars, over the wide range of environments studied.

Subtask 3.6 – Ash Partitioning Mechanisms for Oxy-Coal Combustion with Varied Amounts of Flue Gas Recycle

Laboratory-scale studies

The focus of this study was to investigate the effects of furnace temperature, coal type, and gas-phase conditions, namely, CO_2 versus N_2, on ash particulate formation and refractory oxides composition under controlled conditions. The study utilized particle-sizing equipment allowing a wide range of particle sizes, from submicron to micron. In addition, composition was determined for the different size fractions.

A schematic diagram of the high-temperature, DTF is shown in Figure 2. Synthetic flue gas was used to simulate oxy-fuel conditions and compare these results with air. The furnace was heated by a pair of graphite electric heating elements. An alumina muffle tube (50 mm inside diameter, 40 cm long) served as the central reaction zone with an alumina honeycomb on the top to act as a preheater and flow straightener. The main gas flow rate was maintained at 0.2 L/s, and the coal feed rate was set at 1.5 g/hr. The coal feed rate is low enough that the drop tube operates with little change in gas environment (high excess oxygen conditions).

The DTF outlet stream was diluted by particle-free air while passing through a dilution tunnel for sampling with the particle sizing instruments. A stream (0.3L/min) was introduced into a TSI Scanning Mobility Particle Sizer (SMPS, Model 3080) and an Aerodynamic Particle Sizer (APS, Model 3321) to determine the PSDs. The SMPS has a theoretical measurement range of 14.3 to 673.2 nm, and the APS ranges from 532 nm to 20 µm. A Berner Low Pressure Impactor (BLPI) was utilized for ash size segregation and collection, which were analyzed for elemental composition.

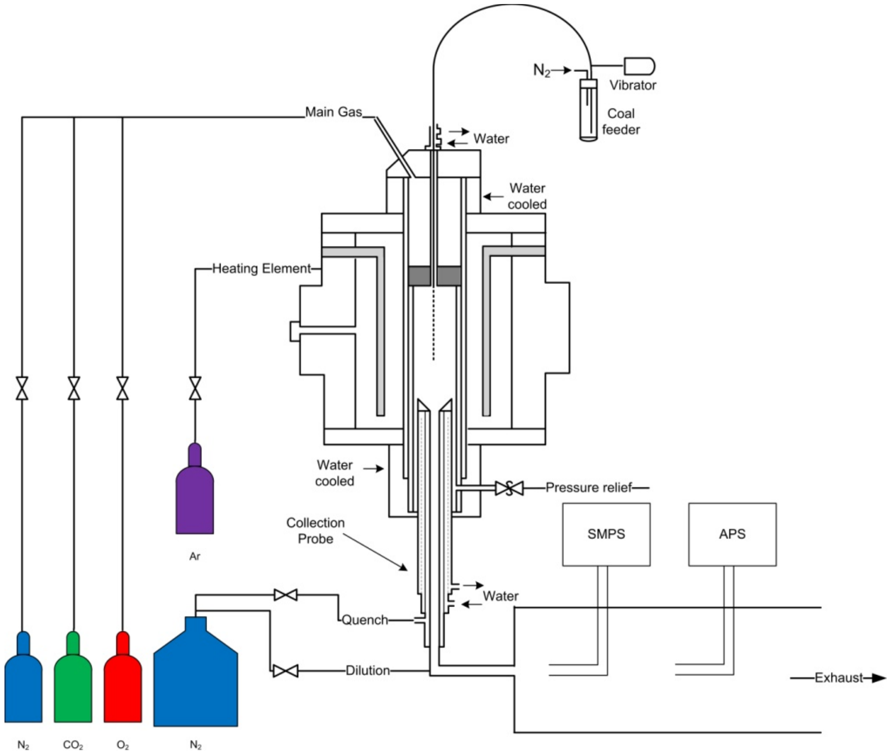

Figure 2. High-temperature DTF.

An O_2/CO_2 mixture was used as the oxidant in the high-temperature DTF experiments to simulate O_2/recycled flue gas combustion, and these results were compared with O_2/N_2 combustion conditions. Two oxygen concentrations, 21% and 31.5%, and furnace wall temperatures were studied. The gas temperature was measured and found to be relatively constant along the length of the reactor and under the different gas compositions. The higher gas temperature was approximately 1520 K while the lower was 1410 K.

Studies in the OFC

Experiments were conducted on a down-fired OFC, which was sufficiently small to allow for systematic control of inlet gas flow rates and wall temperatures yet large enough to simulate the self-sustaining combustion conditions of full-scale units, especially in terms of temperatures, coal particle concentrations, and mixing. As shown in Figure 1, the OFC was designed with three different zones: an ignition zone [0.61 × 0.91 × 1.22 m (inside diameter × outside diameter × height)], a radiation zone [0.27 × 0.61 × 2.60 m (inside diameter × outside diameter × height)], and a convection zone [0.15 × 3.66 m (inside diameter × length)]. In this work, ash aerosol samples were obtained from port 9.

A bag house system was used for fly ash removal. It utilized six fabric filters, which are made of nomex cloth and could work at temperatures as high as 473 K. A pulse system with gas-injection is designed to prevent ash particle buildup on the filters. Either CO_2 from the Praxair CO_2 tank (for oxy-coal combustion) or compressed air (for air combustion) could be injected into the bag house to shake off the ash particles. The pulse interval could be controlled at between 1-30 minutes and pulse lasts for 999 milliseconds. The filters could be removed for RFG with particle laden (dirty recycle). Bag house is installed after convection zone. A condenser was used to remove the moisture in the flue gas.

To obtain ash aerosol information, two groups of instruments were utilized: BLPI and Scanning Mobility Particle Sizer (SMPS) and aerosol particle sizer (APS). The BLPI consisted of 11 stages, with corresponding 50% aerodynamic cutoff diameters of 15.7, 7.33, 3.77, 1.98, 0.973, 0.535, 0.337, 0.168, 0.0926, 0.0636, and 0.0324 µm. Cellulose acetate membranes were used to collect ash aerosol samples for subsequent composition and morphology analyses. Aluminum filters coated with Apiezon grease were used for PSDs. A Mettler Toledo balance with a precision of 0.1 µg was used to obtain the aluminum filter mass. SMPS produces PSD in the size ranges of 0.0143 µm to 0.6732 µm and APS in the size ranges of 0.532 µm to 20 µm. SMPS and APS data are combined and shown in the same figure.

In this research, ash aerosol data was obtained from cases of oxy-coal combustion with four different RFG options and two different RFG amounts. The four different options were:

1) RFG with ash removed, which means recycling the flue gas after the bag house;
2) RFG with ash and moisture removed, which means recycling the flue gas after the condenser;
3) RFG with ash, moisture and sulfur removed, which means recycling the flue gas after the scrubber;
4) RFG with nothing removed, which means recycling totally dirty flue gas.

The two different recycle amounts were:

1) 27 vol. % O_2 / 73 vol. % RFG (overall) in oxy-coal combustion;
2) 50 vol. % O_2 / 50 vol. % RFG (overall) in oxy-coal combustion (except dirty recycle).

Beyond that, cases of air combustion and oxy-coal combustion of 27 vol. % O_2/ 73 vol. % CO_2 and 50 vol. % O_2 / 50 vol. % CO_2 were also conducted. All these cases were given an abbreviation as shown in Table 2.

Table 2. Experimental cases abbreviation and description.

Case abbreviation	Description
Air	air combustion
OXY50 Once	oxy-coal combustion with 50% inlet O_2 and once through CO_2
OXY27 Once	oxy-coal combustion with 27% inlet O_2 and once through CO_2
OXY50-Ash	oxy-coal combustion with 50% inlet O_2 and RFG after bag house
OXY27-Ash	oxy-coal combustion with 27% inlet O_2 and RFG after bag house
OXY50-Ash-H_2O	oxy-coal combustion with 50% inlet O_2 and RFG after condenser
OXY27-Ash-H_2O	oxy-coal combustion with 27% inlet O_2 and RFG after condenser
OXY50-Ash-H_2O-S	oxy-coal combustion with 50% inlet O_2 and RFG after scrubber
OXY27-Ash-H_2O-S	oxy-coal combustion with 27% inlet O_2 and RFG after scrubber
OXY27-Dirty	oxy-coal combustion with 27% inlet O_2 and dirty RFG

Powder River Basin (PRB) coal was used in this research.

Task 4 – Gasification Studies

This report provides highlights of the project's gasification studies. Additional detail can be found in Whitty et al. (2011, 2014).

A key objective of the Task 4 activities has been to develop simulation tools to support development, troubleshooting and optimization of pressurized entrained-flow coal gasifiers. The overall gasifier models (Subtask 4.1) combine submodels for fluid flow (Subtask 4.2) and heat transfer (Subtask 4.3) with fundamental understanding of the chemical (Subtask 4.4) processes that take place as coal particles are converted to synthesis gas and as char transitions to slag (Subtask 4.5). However, it is important to be able to compare predictions from the models against data obtained from actual operating coal gasifiers, and Subtask 4.6 aims to provide an accessible, non-proprietary system, which can be operated over a wide range of conditions to provide well-characterized data for model validation.

Subtask 4.1 – Entrained-Flow Gasifier Simulation and Modeling

This subtask focused on a preliminary evaluation of BYU and CANMET gasifier data, the development of an equilibrium model, LES tools for gasification modeling, and improved surrogate modeling.

Subtask 4.2 – Subgrid Mixing and Reaction Modeling

Efforts surrounding Subtask 4.2 focused on the implementation of several submodels into our one-dimensional turbulence (ODT) model to address the fate of coal particles in combustion/gasification processes, including: (1) moisture evaporation from coal; (2) devolatilization to describe the volatile species and their rates of evolution from the particle to the gas phase; and (3) char oxidation/gasification to calculate the char oxidation rate based on the particle temperature and oxygen partial pressure. For various furnace temperatures and particle sizes, predicted ignition delay was compared with experimental measurements for a single-particle laminar jet. The predicted and measured ignition delay in furnace temperature and particle size studies were compared.

Subtask 4.3 – Radiation Modeling

Subtask 4.3 focused on the expansion of radiative heat-transfer algorithms in the University of Utah LES codes to include coal particles under entrained coal gasification conditions. This was accomplished by enhancing the legacy (DOM) to model the combined effect of the gas-phase and particle-phase absorption coefficients. In addition, a reverse Monte Carlo ray tracing (RMCRT) method was developed to compute accurately and efficiently the radiative heat exchange in LES combustion simulations. To ensure the optimization of the RMCRT algorithm under production-scale conditions, measurements of execution time as well as accuracy were collected. The production-scale simulation was for a large furnace with a computational domain of 24 million cells, run to 70,000+ time steps, using 1300+ processors.

Subtask 4.4 – Char and Soot Kinetics and Mechanisms

Work on Subtask 4.4 development of the development kinetic data for char-steam gasification for various coal chars using the (HPFFB). The investigators also used advanced analysis techniques to understand the structure of soot produced from gasification, including transmission electron microscopy (TEM), nuclear magnetic resonance (NMR), small-angle x-ray scattering (SAXS), and atomic pairwise distribution function (PDF).

Subtask 4.5 – Slag Formation and Slag-Wall Interactions

Experiments were designed to investigate physical changes of coal char during the char-slag transition and to provide data for an ash deposition model that can be incorporated into CFD modeling of entrained-flow slagging coal gasifiers. Therefore, experiments were mainly focused on the ash deposition behavior as well as the changes in physical characteristics of char particles during the char-slag transition.

Three coals were selected for the experiments: Illinois #6, Pittsburgh #8 and Black Thunder from the (PRB). Two types of experiments were carried out: char and ash formation experiments and ash deposition experiments. The purpose of the char and ash formation experiments was threefold: (1) prepare and collect char and ash particles with different conversions that cover the range of the char–slag transition, (2) evaluate the physical changes of char and ash particles and the transformations of mineral–carbon association in the char–slag transition, and (3) identify an indicator for the char–slag transition. The goal of ash deposition experiments was to assess the intrinsic propensity of particle deposition during the char–slag transition. This is valuable for determining whether a particle is inclined to "stick" upon contacting a surface such as a refractory wall or injector face.

All the experiments were conducted in a high-temperature laminar entrained-flow reactor (LEFR). This type of device has been widely used for studying coal conversion and ash deposition behavior because it can provide well-controlled experimental conditions while closely representing the environment in a practical combustion or gasification system.

Subtask 4.6 – Acquisition of Validation Data in an Entrained-Flow Gasifier

Under this subtask, the University of Utah developed an EFG that offers unique opportunities to acquire new performance data to aid with validation of simulation models under development. While there are many operational issues that impact EFG performance and operation, performance of the coal-water slurry (CWS) injector is one of the most critical. In addition to development and refinement of the EFG and operating conditions, efforts focused on slurry spray characterization and modeling, and associated development of an efficient injector for the EFG. The other component of this work characterized the environment within the gasifier itself.

Task 5 – Chemical Looping Combustion

The following sections provide highlights of the CLC tasks. Additional detail can be found in the CLC topical reports (Sarofim et al. 2011, 2014).

Subtask 5.1 – Process Modeling and Economics

The detailed rate analysis for CLOU, utilizing reported experimental data for combustion of Mexican petcoke particles in the presence of a CuO/ZrO_2 oxygen carrier, was performed. Using the Law of additive reaction times, the activation energy for petcoke oxidation was estimated and the apparent kinetic rate constants for Cu_2O oxidation. The kinetics of CuO reduction and petcoke oxidation determined from the rate analysis of CLOU process were utilized in developing a fluidized-bed model for the fuel reactor.

ASPEN PLUS process models were developed for a solid-fuel based chemical-looping process development unit using a copper-based oxygen carrier for CLOU. An oxygen carrier circulation rate for CLOU of and copper loading CuO on ZrO_2 were determined based on an optimum conversion of 54% in the fuel reactor and 50% in the air reactor. The results of an ASPEN PLUS model for CLC were based on the transition from Fe_2O_3 to Fe_3O_4 and a circulation rate of 98 kg oxygen carrier /kg coal for combustion with 60% Fe_2O_3 on Al_2O_3 oxygen carrier.

Finally, a relative economic analysis was performed between the CLOU process with a copper-based oxygen-carrier and CLC with an iron based oxygen-carrier.

Subtask 5.2 – LES-DQMOM Simulation of a Pilot-Scale Fluidized Bed

This subtask focused on developing high-performance simulation tools for CLC applications. Work included a sensitivity analysis for various simulation parameters, namely CLC bed height, fluid velocity, and particle size for non-reacting CLC systems, available from experiments conducted by Particulate Solid Research, Inc. (PSRI) in conjunction with the National Energy Technology Laboratory (NETL). In order to accomplish this, the investigators developed a computer-aided design (CAD) and mesh details, the sensitivity analysis methodology and comparison of our simulation results with experimental results.

Subtask 5.3 – Laboratory-Scale CLC Studies

Oxygen carrier development is critical to the development and design of a commercial CLC system. This subtask focused on attrition resistance and fluidization quality. Of most practical interest for design of demonstration and full-scale systems is the rate of oxygen carrier oxidation and reduction as relates to temperature, conversion and gas environment. This subtask considered performance and evaluation of several copper-based CLOU carriers with different loadings of CuO and were manufactured by different techniques. The carriers are summarized in Table 3.

Table 3. Copper-based oxygen carriers used.

Carrier Code	Source	Production Method	Mass % CuO
12_Al2O3_IW	Sigma Aldrich, USA	Incipient Wetness	12
50_TiO2_MM	ICPC, Poland	Mechanical mixing	50
45_ZrO2_FG	Chalmers, Sweden	Freeze granulation	45
50_SiO2_IW	University of Utah	Incipient Wetness	50
70_SiO2_IW	University of Utah	Incipient Wetness	70
20_FeTiO2_IW	University of Utah	Incipient Wetness	20

The rates of carrier oxidation and oxygen liberation were evaluated under a variety of temperatures, reactor gas oxygen concentrations and degrees of conversion to quantify the influences of these variables and to develop mathematical models to describe conversion rates. Performance of the CLOU system for conversion of several solid fuels was evaluated, and the degree of oxygen carrier particle attrition was quantified in the bubbling bed CLC reactor system that was built for this subtask.

Subtask 5.4 – CLC Kinetics

The investigators focused on two aspects of CLC, understanding kinetics in TGA experiments and development of a supported oxygen carrier.

The kinetic looping experiments were carried out using two TGA instruments: a TA Q500 and a TA Q600. The TA 500 is a vertical design, and the TA Q600 instrument is a horizontal design. Looping experiments were executed using both a copper powder (Sargent-Welch Scientific Co., 150 mesh, reported average particle size 9 µm) and a cupric oxide powder (Johnson Matthey Chemicals, having a determined particle size range of 1-10 µm). These results were used to identify the appropriate temperatures for the air and fuel reactor.

Oxygen carrier development is critical to the development and design of a commercial CLC system. This subtask considered performance and evaluation of several copper-based CLOU carriers. The rates of carrier oxidation and oxygen liberation were evaluated under a variety of temperatures, reactor gas oxygen concentrations and degrees of conversion to quantify the influences of these variables and to develop mathematical models to describe conversion rates. Performance of the CLOU system for conversion of several solid fuels was evaluated, and the degree of oxygen carrier particle attrition was quantified.

Task 6 – Underground Coal Thermal Treatment

The following sections provide highlights of the UCTT subtasks. Additional detail can be found in the UCTT topical report (Smith et al. 2015).

Experimental studies

The UCTT process was evaluated at two scales, laboratory in the fixed-bed reactor and larger scale in the rubblized-bed reactor (RBR). Both the scoping tests and the RBR experiments were performed with Utah Sufco coal in a nitrogen environment. This high-volatile bituminous coal (38.6% volatile matter, as received) has a relatively low moisture content and is expected to provide a better volatile yield than some other coals. Table 4 shows the average ultimate and proximate analyses of the coal (before pyrolysis) and char (after pyrolysis) samples. The moisture content was on average 3.2 ± 0.15 % before pyrolysis and 1.31 ± 0.27 % after pyrolysis. The ash content was more variable with an average of 5.04 ± 1.82 % before pyrolysis and 5.32 ± 2.13 % after pyrolysis, which could indicate that inclusions in the coal are affecting the composition. The coal's heating value was 14,078 btu/lb (as received).

Table 4. Ultimate and proximate analyses for the coal (average of 6 samples) and char (average of 11 different samples). The results are in weight percent on a dry ash free basis.

	Proximate analyses		Ultimate analyses				
	FC	V	C	H	N	O	S
Coal	54.8 ±0.62	45.3±0.62	78.5±0.22	5.61±0.06	1.72±0.06	13.6±0.28	0.65±0.08
Char	90.9±3.10	9.07±3.10	91.8±1.89	2.19±0.55	2.09±0.17	3.34±1.30	0.62±0.15

FC: fixed carbon; V: volatile content; C: carbon; H: hydrogen; N: nitrogen; O: oxygen; S: sulfur.

Experimental scoping studies used the University of Utah's FBR, which has a ¾" diameter and a 6" bed length. The FBR can be operated at pressures up to 300 psi and temperatures up to 800°C. The scoping studies were used to identify the most promising conditions prior to the RBR studies. The reactor can operate at pressures up to 1500 psi and temperatures up to 600^{o}C. The RBR utilizes a unique two-vessel design to achieve its severe operating thresholds. The outer vessel is an 18” diameter pressure vessel that is built to withstand the maximum operating pressure at temperatures up to 300^{o}C. Housed inside the pressure vessel is a 6” diameter vessel that contains the rubblized coal bed. The inner vessel has an electrical heat source that conductively heats adjacent coal blocks and induces convective currents in the free spaces between blocks. External lines through both vessels permits a steady purge of nitrogen so that gas samples can be collected during pyrolysis. In addition to providing a more realistic heating profile, the RBR can allow examination of the effect of coal rubblization. Because the high-pressure experiments were so difficult to perform, the team was only able to perform a limited number of these.

Simulation studies

The investigators completed HPC simulations of UCTT using realistic coal properties, based on the experimental studies, and realistically sized domain representative of an actual coal field located in Utah (Figure 3). These studies focused on the investigation of heat transfer and yield models, as well as various seam thicknesses and heater temperatures/configurations.

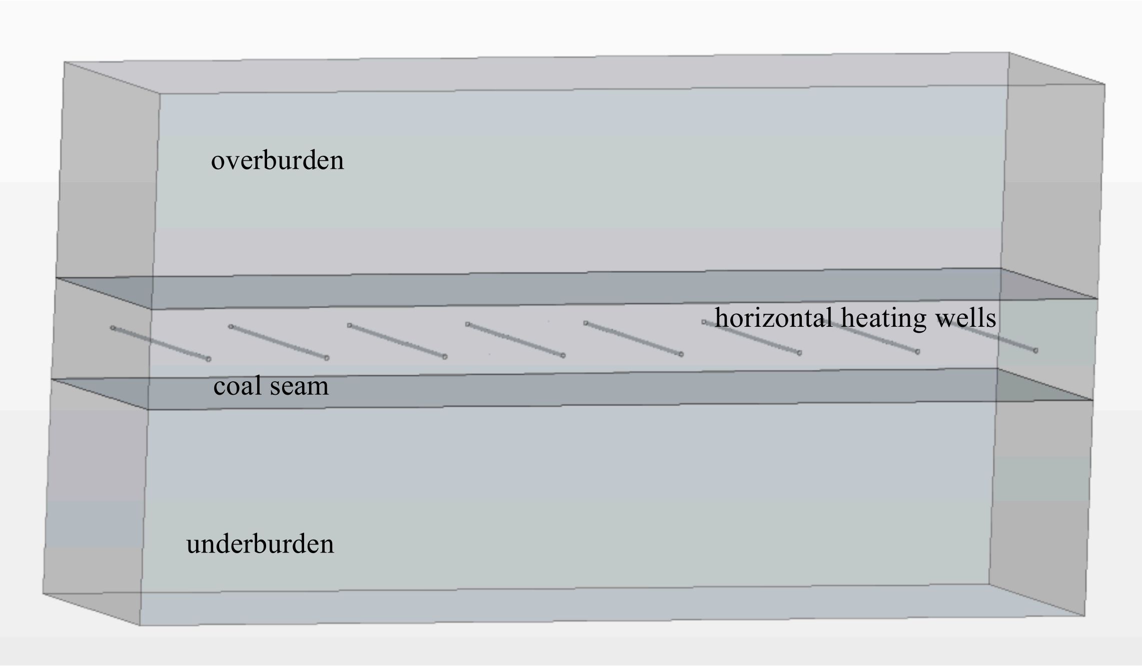

Figure 3. New simulation geometry representing Wasatch Plateau coal field with horizontal heating wells surrounded by overburden and underburden.

The results section used the following yield model:

$$Yield = Yield_{max} / (1 + \exp(0.02096\,(T_{fit} - T)))$$

where: T is temperature in degrees K, $Yield_{max}$ is the maximum yield (0.4525), and T_{fit} is the temperature constant determined from the experimental runs (745 K).

CO_2 storage studies

The goal of this subtask is to describe the adsorption of methane and carbon dioxide on a coal that has undergone pyrolysis with slow heating rates. Three different coals were examined in this study: a Utah bituminous coal from the Sufco/Skyline mine in Utah, an Illinois bituminous coal from the Carlinville mine, and a Powder River Basin (sub-bituminous) coal from the North Antelope mine near Gillette, Wyoming. All of the coals used for this study were already crushed to approximately 20 mm chunks.

Pyrolysis of the coal samples was performed in a 64mm clamshell-style tube furnace 24 inches (61 cm) in length. The tube furnace used was a Thermo Scientific Lindberg Blue controlled using an Omega CN1504 programmable process controller. Ultimate pyrolysis temperatures of 325, 450, and 600°C were chosen as likely temperatures encountered with UCTT.

The isotherm measurement apparatus was designed using custom machined reference and sample cells rated to 690 bar at 100°C made out of polished stainless steel. All of the isotherm measurement units were placed in a custom-made stainless steel bath filled with Xiameter, a Dow-Corning silicone-based fluid selected for its low vapor pressure and high temperature stability. The temperature of the bath was controlled using a VWR 1122s immersion heater/circulator.

Measurement on each coal sample involved two different gasses (CO_2 and CH_4) at two different measurement temperatures (50°C and 70°C) resulting in four isotherm measurements for each sample. Measurement temperatures were chosen as reasonable approximates of an unmineable coals in situ temperature.

Task 7 – Mercury

This section provides highlights of the mercury task methods; additional detail can be found in the mercury topical report (Buitrago et al. 2010).

The fate and speciation of mercury in oxy-coal combustion processes are of particular interest because trace amounts of mercury lead to the embrittlement and cracking of aluminum heat exchangers that are used in the cryogenic separation and compression of CO_2. Mercury exists in three forms in coal-derived flue gas: particle-bound (Hg^p), oxidized (Hg^{++}), and elemental (Hg^o). The oxidized form is desirable because it is more readily removed by adsorption on solids and is more readily captured by absorption in wet flue gas desulfurization scrubbers. The adsorbed, particle-bound mercury is removed by electrostatic precipitators or fabric filters.

Oxidized mercury is primarily mercuric chloride ($HgCl_2$) and its formation depends on the halogen content of the coal and the existence of catalytic surfaces that enable oxidation. The latter include unburned carbon and selective catalytic reduction reactors. The mercury work focused on the homogeneous, gas-phase oxidation of mercury by bromine and chlorine under oxy-firing conditions.

Bench-scale experiments were conducted in a quartz-lined, natural gas-fired reactor with the combustion air replaced with a blend of 27 mole percent oxygen, balance CO_2. Quench rates of 210 and 440 K/s were tested. A 300-W, methane-fired, premixed burner made of quartz glass supplied realistic combustion gasses to the reactor. All reactants were introduced through the burner and passed through the flame to create a radical pool representative of real combustion systems. The burner provided 3.7 SLPM (standard liter per minute) of combustion gases. To study the effects of flue gas components, such as SO_2, NO, NO_2, HCl, and HBr, different concentrations of these or related species were introduced through the burner.

A Tekran 2537A Mercury Analyzer, coupled with a wet sample conditioning system designed by Southern Research Institute (SRI), provided measurement of total and elemental mercury in the exhaust gas. Details of the sampling system can be found in Buitrago et al. (2010).

The experiments were performed with different dopants added through the burner. All species that were added to the reactor (SO_2, NO, Cl_2, Hg^0, and Br_2) passed through the flame. Their subsequent speciation depended on flame chemistry as well as on the temperature profile in the reactor. Before adding these, the baseline mercury level at the furnace outlet was checked using a material balance. Experiments were generally repeated at least three times. The effects of oxy-firing on flue-gas composition were not independently measured with gas analyzers as they were for the air-fired results. For the oxy-fired experiments, the air was replaced with a mixture of 27 percent oxygen and 73 percent CO_2, and the amount added was calculated to give the same oxygen level, 1.0 percent, as in the air-fired tests. Additional details of the experimental methods can be found in Buitrago et al. (2010).

Task 8 – Strategies for Coal Utilization in the National Energy Portfolio

The following sections provide highlights of the policy subtasks. Additional detail can be found in the in Davies et al. (2012, 2013, 2014), Reitze (2011a, 2011b) and Reitze and Durrant (2011a, 2011b, 2011c).

Coal-fired power plants face increasing challenges, both from litigation and from regulatory uncertainty. Nonetheless, coal is certain to be a paramount resource, even in a carbon-constrained world, as the nation's population and power demands continue to expand. Thus, a critical question is the legal and socio-economic position that coal will assume as we move toward climate regulation. This task addressed that question by analyzing existing regulatory approaches to promoting CCS technology, as well as emerging legal challenges to deploying CCS technology.

Subtask 8.1 – Existing Regulatory Framework and Emerging Policy Issues

This subtask explored the technical and legal barriers that must be addressed in order to have a viable carbon sequestration program. As addressed by this subtask, CCS deployment activities are potentially subject to the regulatory authority of several federal agencies, including the U.S. Environmental Protection Agency (EPA) and the Departments of Energy, Transportation and Interior. The subtask further considered the relevance of the Safe Drinking Water Act, the Clean Air Act (CAA), the National Environmental Policy Act (NEPA), the Endangered Species Act, and other applicable federal laws. Finally, the subtask evaluated the CCS provisions included in Congressional efforts to address climate change in 2009 and 2010.

The subtask also explored how regional bodies and state government are addressing the technical and legal problems that must be resolved in order to have a viable carbon sequestration program. Several regional bodies have formed regulations and model laws that affect carbon capture and storage, and three bodies comprising twenty-three states—the Regional Greenhouse Gas Initiative, the Midwest Regional Greenhouse Gas Reduction Accord, and the Western Climate initiative—have considered or developed cap-and-trade programs. State property, land use and environmental laws affect the development and implementation of carbon capture and sequestration projects, and unless federal standards are imposed, state laws on torts and renewable portfolio requirements will directly affect the liability and viability of these projects.

Subtask 8.2 – Barriers to and Regulatory Promotion of Emergent CCS Technology

To gain a better understanding of the most significant barriers to commercial- scale use of CCS—and how government entities might best act to alleviate those barriers — the subtask investigators conducted an anonymous opinion survey of parties with expertise in the CCS field. Specifically, the survey included six overlapping classes of recipients:

- those working directly in the CCS industry;
- those who provide professional (e.g., engineering, legal, or financial) services to the CCS industry;
- CO_2 emitters;
- those who conduct research involving CCS technology and policy;
- non-profit advocacy organizations; and
- government regulators.

The survey examined three questions:

- What are the most significant obstacles to broad-scale CCS use?
- What incentives might best overcome those obstacles?
- How should CCS regulation be shaped to close the gap between the state of the CCS industry today and its realization as a full-fledged climate change solution?

Details of the survey development, survey methods and the complete survey can be found in Davies et al. (2012). Using commercially available survey software, the investigators distributed the survey via email. Survey participants responded anonymously via the internet, with 229 responses, 195 of which were complete and 34 of which were partially complete.

The subtask also evaluated barriers to CCS commercialization that were identified in the survey, and considered them in the context of potential models for CCS regulation and promotion. Various regulatory models could be applied to incent CCS technology diffusion, including design standards, performance standards, and market-based regulatory mechanisms. Briefly, design standards mandate the use of a particular technology, whereas performance standards utilize a numerical limit to set a pollution limit that is equivalent to the pollution reduction capacity of a given technology. Market-based regulatory regimes attempt to harness economic forces to reach a given regulatory result; those potentially applicable to CCS include a carbon tax, a cap and trade system, and subsidies.

This subtask examined options for promoting CCS through regulation including technology-based design standards, technology-based performance standards, market-based regulatory mechanisms, such as a carbon tax, cap and trade, and subsidies as well as a case study of policies governing SO_2 and NO_x emissions. The investigators also examined the results of other studies that used mathematical models to predict the CCS adoption inducement potential of:

- differentiated CO_2-trading schemes;
- a combination of differentiated CO_2-trading schemes and an adoption subsidy;
- a combination of differentiated CO_2-trading schemes and a directed research and development (R&D) subsidy; and
- a combination of differentiated CO_2-trading schemes and differentiated R&D subsidies.

Finally subtask investigators considered the EPA's proposed new-source performance standard (NSPS). At the time this task concluded, EPA had not issued its proposed NSPS for new coal-fired power plants or its proposed NSPS for existing power plants.

Task 9 – Validation/Uncertainty Quantification for Large Eddy Simulations of the Heat Flux in the Tangentially Fired Oxy-Coal Alstom Boiler Simulation Facility

Details of the methods used for this task can be found in Smith et al. (2014).

Subtask 9.1 – LES Simulation and V/UQ for Heat Flux in Alstom Oxy-coal-Fired BSF

The objective of this subtask was to work directly with Alstom Power Inc. (Alstom) to apply the large eddy simulation (LES) and V/UQ strategies developed under this research program to Alstom's 15 MW_{th} BSF. Developing these simulation capabilities required improvements in numerous of the supporting models as well as code efficient. Efforts focused on modeling turbulence, multiphase flow, coal particle reactions, and radiation, which grew out of subtask 4.3.

This study targeted a formal validation and uncertainty quantification using 50 different measurements of the heat flux, temperature and O_2 concentration as the specific quantity of interest (QOI) as a function of wall thermal conductivity, fuel feed rate, and coal reactivity. The validation approach identified the region of simultaneous consistency between all experimental and simulation data, according to the consistency constraint, $u_e \geq [y_m(x) - y_e] \geq l_e$, where the defect between the QOI as predicted by the model and as measured by the experiment is bounded by the measurement uncertainty. The experimental measurements were collected in the BSF, owned and operated by Alstom Power in Windsor Connecticut.

To identify the most sensitive parameters affecting these QOI, the Simulation Team drew on the collective prior knowledge of the University/Alstom team. An input uncertainty map (I/U map) was created with the various numerical, modeling and scenario parameters that might affect heat transfer, with estimated bounds or uncertainty intervals added for those parameters where prior knowledge was available. The parameters were prioritized based on their projected impact on temperature and wall heat flux. The highest priority parameters are the scenario boundary conditions, and the scenario parameters selected that have the greatest impact on the wall heat flux are the wall's thermal resistance and the flow rates -- the coal, oxygen and recycle flow rates. Model parameters with lesser impacts are postulated to be radiation and homogeneous and heterogeneous reaction parameters. Prior research indicated that the devolatilization rates are likely the most important model parameters. Various simulations were performed to explore the sensitivity of these parameters for the BSF heat flux. Ultimately the wall thermal conductivity of the main furnace was selected as the parameter to be explored in the VUQ analysis.

There are four different wall-insulation zones as a function of vertical height in the BSF, with the upper furnace wall being un-insulated, bare steel, as shown in Figure 5. This figure also shows the location of the three levels (L1, L2, and L3) where the average plane temperature was experimentally measured for the V/UQ study. The thermal boundary conditions for the simulation specified the backside temperature of heat transfer surface at 375 K, corresponding to the boiling water temperature in which the BSF sits. The wall thermal resistance is the ratio of the parameters $\Delta x/k_w$, where Δx is the thickness of the resistance material(s), and k_w is the wall thermal conductivity. For this study, the uncertainty in k_w for the main combustor was considered to be the most sensitive parameter of the QOIs.

Table 3 shows the formal V/UQ matrix, indicating the simulations that were run and used in the final analysis. The simulations were then performed spanning the range of the uncertain thermal conductivity of the main furnace. A few surfaces, such as the nozzles themselves and a portion of the corner plate through which the nozzles protrude, were prescribed with adiabatic thermal boundary conditions. All of the superheater platens and the tubes in the economizer bank in the backpass were individually represented, made possible by the HPC simulation.

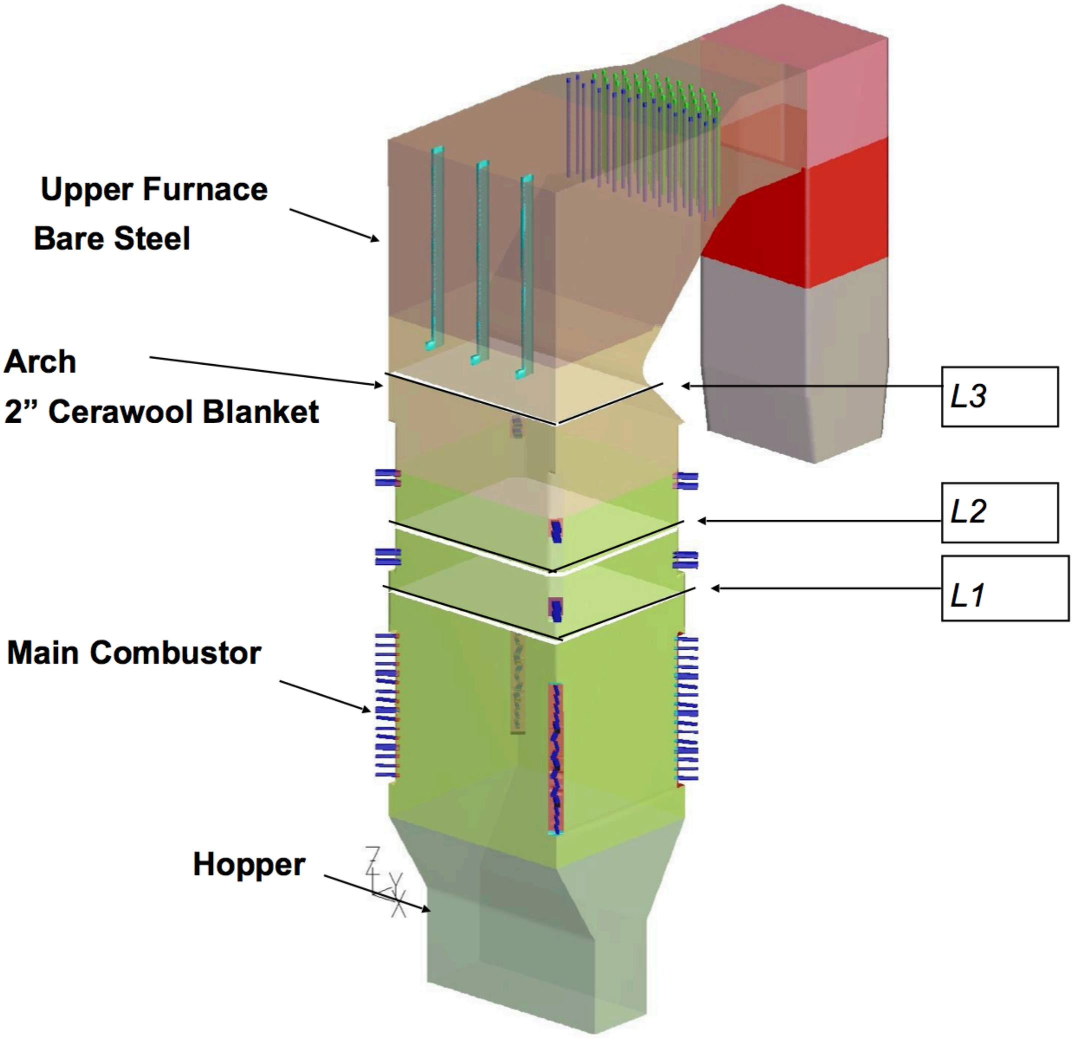

Figure 4. Schematic of thermal boundary conditions in the BSF.

Table 5. VUQ matrix indicating that values used in the various simulations of the BSF.

Case ID	Main Furnace Thermal Conductivity [W/m-°C]
Case 1	2
Case 4	1.5
Case 5	2.5

Each of the simulations performed to map out the uncertainty space was constructed with 2 cm resolution and had 17.414 million cells. Based on a preliminary investigation of the computing efficiency and associated wall clock time for the baseline case on a supercomputer cluster, about $(20.4)^3$ cells/processor was selected for the simulation runs. Each computation was run on 2,008 processors. One large case was constructed with a resolution of 1 cm, resulting in 137.216 million cells. This latter case required 9,920 processors to run in parallel. After the code optimization analyses and several necessary initial tests, the final version of the baseline case was started in July of 2013 on the Oak Ridge National Laboratory's

Titan machine. The typical time step in the LES simulations was about 3.0×10^{-5} seconds. It took 2,930,850 CPU hours to acquire a physical time of 22 seconds of simulation results. Accordingly, the estimated simulation cost is about 2.5~3 million hours for each of the V/UQ cases (to achieve the requisite 22 seconds of real time). The physical time of about 22 seconds is about 3 times longer than the boiler residence time. The initial testing showed that the evacuation time of the boiler was about 8 seconds (depending on the wall boundary conditions and the initial conditions). After each case was run, the results were time-averaged over the last 5 seconds of the simulation and then further post-processed for use in the V/UQ studies.

The V/UQ was based on the consistency approach of Frenklach and Packard from University of California at Berkeley.

Subtask 9.2 – LES Simulation and V/UQ for Heat flux in Subscale UofU Oxy-coal-Fired OFC

This subtask focused on evaluation of the University of Utah's OFC. The multi-phase aspect of the system is modeled using DQMOM, allowing a representation of the particle size segregation and clustering in the system. The validation approach, like subtask 9.1, identifies the region of simultaneous consistency between experimental and simulation data.

Modeling strategy

An illustration of the OFC geometric representation in Arches is shown in Figure 5. Only the burner zone of the OFC is represented in the simulation. The OFC burner zone consists of a cylindrical reactor with a converging section that leads to the radiant zone. The primary inlet is located at the top of the burner, and injects the coal entrained in a carrier gas downward into the burner. The secondary stream is an annulus inlet, surrounding the primary inlet, injecting the secondary gas downward into the burner. Three side inlet streams are also represented because of their use with the radiometer instruments. The reactor is lined with Insboard refractory, and has two windows installed opposite each other on the walls of the reactor.

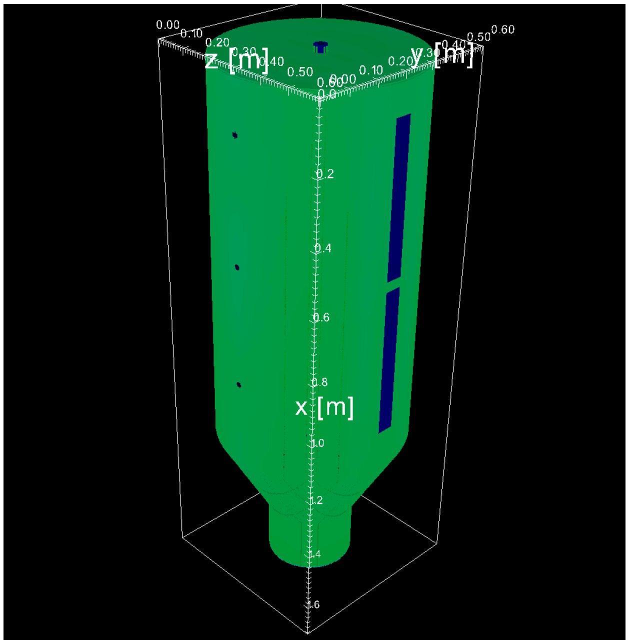

Figure 5. Illustration of the OFC in Arches.

The OFC burner mesh consisted of a structured mesh with cell dimensions of 4x3x3 mm in the x, y, and z directions. Running conditions for the OFC simulation varied slightly from the experimental values, because of the selected mesh resolution, Table 6 highlights these differences. Significant differences in area and velocity of the inlet streams are observed, because of the mesh resolution. However, the mass flow rates of the experimental are consistent with those in the simulation, in order to ensure that the same amount of mass is entering in domain, albeit at a slightly different velocity.

Table 6. Comparison of running conditions during experiment, and those used in the simulation.

Measurement	Experiment	LES	% diff.
Primary inlet area [m^2]	2.32e-4	2.88e-3	24.0
Secondary inlet area [m^2]	5.56e-4	5.40e-4	2.8
CO_2 purge inlet area [m^2]	3.05e-4	2.40e-4	21.2
Primary velocity [m/s]	4.56	3.68	19.3
Primary mass rate [kg/s]	1.79e-3	1.79e-3	0
Secondary velocity [m/s]	4.69	4.82	2.89
Secondary mass rate [kg/s]	2.08e-3	2.08e-3	0
Purge stream velocity [m/s]	0.52	0.67	27.0
Purge stream mass rate [kg/s]	2.86e-4	2.86e-4	0

The particle size distribution (PSD) of the coal particles have been characterized according to several different measurement techniques. Details of the various PSD measurements can be found in the results section of subtask 9.4. For the current study the following particle sizes and number densities were selected to represent the number density of the particles:

Table 7. Particle size distribution approximation.

Particle Size [µm]	Number density
3	0.66
6.4	0.33
12.5	0.01

Multiphase physics play a crucial role in the combustion process of the system. DQMOM is used in the present analysis. This approach attempts to represent the joint number density function of the system by transporting the weights and weighted abscissa from the Gaussian quadrature approximation of the joint distribution.

Gas-phase reactions in the system are modeled using a three-stream mixture fraction approach, in conjunction with equilibrium assumptions. The discrete ordinates (DO) method is used to account for the radiation within the simulation. Several simulations were run in order to determine the sensitivity of the solution to the number of ordinates used in the DO model. For the current case, eight ordinates proved to be sufficient to avoid error from ray effects.

The experiment uses narrow-angle radiometers for the heat flux measurements. In order to compare to the heat flux a 'virtual radiometer' was needed. The radiometer uses a reverse-Monte Carlo ray tracing approach, to estimate the flux for a narrow spectrum of rays.

Uncertainty quantification

Uncertainty in the experimental analysis as well as the simulation exists. In order to compare the simulation with the experiment it is important to be able to quantify these uncertainties, and attempt to account for these uncertainties in the modeling approach.

Several sources of error exist which make the comparison challenging. These sources of error come from experimental measurements, from models used in the simulation, and from numerical sources found in the code. In general, these sources are generated from unknown parameters, which, when changed can have a large impact on quantities of interest. These parameters include experimental or scenario parameters, modeling parameters, and numerical parameters. Depending on the (QOI) the unknown parameters may or may not have a significant impact. Because heat fluxes to the walls of the boiler are essential to power generation, the heat flux to the walls is the QOI for the current system.

Parameters within the experimental setup, can contribute to uncertainty in the simulation. These parameters are called experimental or scenario parameters. These parameters have an assigned range based on prior knowledge or experience. Smith et al. (2014) describes the parameters and associated uncertainties.

Subtask 9.3 – IR camera diagnostics & V/UQ for temperature measurements in UofU OFC

System development and optimization

Over the course of this project, multiple diagnostic techniques were optimized to provide the best possible temperature and heat flux data for the simulation team (subtask 9.2). The final setup discussed in this report includes heat flux and blackbody temperature data from the MWIR camera and temperature and soot concentration data from the high-speed, visible camera. A total of 3050 unique images were taken on each camera for each repetition, and these 3050 were analyzed. Table 11 summarizes the camera settings for the MWIR and high-speed visible camera during the February 2014 campaign.

Table 8. MWIR and high-speed camera settings for the February 2014 campaign.

MWIR camera settings	
Integration Time (ms):	0.1
Frame Rate (Hz):	1000
Aperture:	2.8
Filter Band (nm):	3825-3975
Gain:	1

High-speed camera settings	
Integration Time (ms):	1
Frame Rate (Hz):	1000
Aperture:	8
Filter Band (nm):	481-519 & 661.5-691
Gain:	1

MWIR method to calculated heat flux and temperature

To process the MWIR images into an infrared heat flux measurement, the MWIR camera was calibrated using a blackbody source of known temperature and emissivity.

Before analysis, each of the 15 sets of images from both cameras were registered so that the images "viewed" the same area despite the difference in location of the cameras. Once the visible images were registered, the MWIR image was overlaid onto the green high-speed image and transformed by an affine transformation until the flame contours again matched. Once the registrations for each camera and each repetition were complete, every image was cropped, rotated and stretched according to the transformations. In the visible images, this means that the red and green images were correlated to each other and then the ratio between the two pixel responses could be found, which provided valid two-color pyrometry data. The infrared registration enables easier comparison to the visible images. This registration was performed for each of the fifteen repetitions, in order to account for any accidental shifting of the cameras over the three-day experimental campaign.

Once the images were properly registered, the data in each pixel of the 3050 images were fit with a lognormal distribution. The mean of each lognormal distribution at each pixel gave a two-dimensional map of the average pixel response for each repetition. The calibration curve was then used to convert from pixel count to the infrared heat flux (W/m^2). To calculate the temperature from the infrared images, an assumption had to be made. Since the flame was not a perfect, blackbody radiator (unlike the calibration source), a spectral emissivity term, ε_λ, must be included in the equation for emissive power.

Comparison of broad-spectrum radiometer to narrow spectrum MWIR measurements

Both the narrow-angle radiometers (NARs) and the MWIR camera measure the radiative heat flux from the flame. However, the radiometers measure the heat flux in the full wavelength spectrum (from 0 to infinity) and the MWIR camera measures in a narrow, 150 nm band in the infrared spectrum (3825-3975 nm). Smith et al. (2014) (subtask 9.3) describe the conversions necessary to perform this comparison.

Visible, two-color method to calculate temperature and soot concentration

The method for finding temperature and soot concentration with the high-speed visible images is fairly similar to that for the MWIR images. The images are imported and registered. The green and red images were separately fit with a lognormal distribution at each pixel for each of the 15 sets. This provided separate red and green, two-dimensional, pixel response maps.

To calibrate the high speed, visible camera, a National Institute of Standards and Technology (NIST) standard calibrated tungsten filament lamp was used. Since there is data from both colors, the emissivity of the flame may be taken into account, unlike with the MWIR camera, where we must assume the flame is a blackbody radiator. Smith et al. (2014) (subtask 9.3) describe the conversions necessary to perform determine temperature and soot concentration.

Subtask 9.4 – Heat flux profiles of UofU OFC using advanced strategies for O_2 injection

Thermal radiation heat transfer in gaseous media can be an important mode of heat transfer in high-temperature combustion systems, such as combustors, furnaces and fires. Growing concern with the modeling of exhaust gases in high-temperature combustion systems has underlined the need for evaluation of the effect of radiative heat transfer. To fully understand thermal radiation in turbulent oxy-coal flames and to validate simulation models, accurate experimental data are needed.

Radiometers are widely used to measure the radiative flux incident at a position corresponding to the front face of the radiometer. In the present work, NAR are used to provide heat flux measurements at three locations in the reaction zone of the oxy-fuel combustor. The experimental data will be used for validation/uncertainty quantification of existing simulation models.

Additional measurements using both NARs and wide-angle radiometers (WARs) subsequently showed that even at very high inlet O_2 concentrations, corresponding to minimum flue gas recycle, it was possible not to have to manage extremely high heat fluxes in the combustion chamber, provided that O_2 injection strategies were judiciously applied.

Experimental set-up

A detailed description of the 100 kW down-fired OFC facility is given in Wendt et al. (2012). The modifications to the experimental system that allowed for the work performed in conjunction with subtask 9.3 included:

- Installation of a type-B thermocouple to measure the gas temperature in the burner zone (reaction zone), this temperature was taken as the reference to establish system stability. The thermocouple was placed at a height near the middle port and few centimeters into the reaction zone, measured from the inner wall of the OFC.
- The internal heaters in the burner zone were removed. Some of the heaters in the reaction zone were damaged, and some had fallen off from the inside wall of the furnace, days before the

planned experimental campaign. There was not sufficient time to replace them, and it was necessary to remove the ones that were still attached to the inside wall in order to provide a uniform boundary condition in order to facilitate the modeling work.

Three NARs were used to measure the radiant heat flux of the flame at various locations in the burner zone of the OFC. The NARs were placed in the top, middle and bottom ports of the OFC reaction zone, which are located at 17.5 cm, 55.6 cm and 93.7 cm below the burner tip, respectively. The radiometers were aligned with the inside wall of the furnace.

The NAR measures the incident radiation emitted from a location in the narrow view of the probe (about 2.74 degrees). The narrow angle probe is essentially a long water-cooled jacket with a sensing element at the receiving end. The long probe collimates the light in the field of view, which is focused onto a thermistor, and as the thermistor changes temperature the resistance changes.

Cooling water is required to lower the temperature of the NAR probe and CO_2 is used as purging gas to prevent any particles or contaminants (condensing ash, tars, etc.) from entering the probe. Water and CO_2 flow rates for each radiometer were 2 L/min and 2.27 lb/hr, respectively.

Both NARs and WARs were used to measure radiant heat fluxes of some of the advanced oxygen injection configurations tested. One NAR and three WARs were applied to measure the radiant heat flux of the flame in various combustion operating conditions.

The radiometers were calibrated using a blackbody radiator at different temperatures. The temperatures were close to the furnace temperature to simulate the environment of the furnace.

A double concentric-burner consisting of two streams (named primary and secondary streams) was used in this study to obtain an aerodynamic simple axial flame and facilitate its modeling. The primary stream consists of a CO_2/O_2 mixture and goes through the center of the burner. The secondary stream consists of O_2 and flows around the primary jet. In this study CO_2 was used as carrier gas to transport the coal from the coal feeder into the reaction chamber through the primary stream of the burner.

Oxy-coal experiments were performed in the OFC reactor using pulverized bituminous Sufco coal as the fuel. Fifteen tests were carried out during a three-day period. All the tests were run under the same experimental conditions for evaluation of data repeatability.

Table 9 presents the summary of the OFC running conditions and coal characteristics.

At the beginning of each test, the windows located in the reaction zone of the OFC were cleaned with high-pressure air in order to ensure optimum conditions for optical measurements. Measurements were taken when the gas temperature inside the furnace reached steady conditions, which was achieved at about 1780 °F (this temperature was monitored with the type-B thermocouple).

Table 9. Experimental conditions and coal characteristics.

Firing rate (Btu/hr)	100000
Coal	Sufco
Coal feeding rate (Lb/hr) Std dev.	8.4 0.039
Primary O_2. Mass flow rate (Lb/hr) Std dev.	2.3 0.0017
Primary CO_2 Mass flow rate (Lb/hr) Std dev.	11.9 0.043
O_2 in primary stream (Vol. %)	21
Secondary O_2 Mass flow rate (Lb/hr) Std dev.	16.5 0.036
O_2 - Overall burner (Vol. %)	68.5
CO_2 for each radiometer (Lb/hr)	2.27
P inside reactor (in H_2O)	0.1
Burner excess O_2 (Vol. %)	5.4
Overall excess O_2 (Vol. %)	4.5
Gas Temp. type-B thermocouple (°F)	about 1780

Coal composition	(%)
C	67.87
H	4.77
N	1.09
S	0.36
O	11.44
Moisture	6.11
Ash	8.36
High heating value (Btu/lb)	11899

Minimization of CO_2 diluent and its effect on radiant heat flux in the combustion chamber

This portion of the subtask focuses on the effects of the reduction of CO_2 as much as possible on the heat of radiation in a 100 kW pilot-scale oxy-coal combustor using burners with *directed pure* oxygen in a *segregated* stream. It is important to note that in this study, the RFG is not recycled, and CO_2 is supplied from a tank. Reduction of the amount of CO_2 in the OFC resembles the reduction of RFG recycle ratio in oxy-coal combustors. This study explores how changes in the composition and temperature of gaseous products of combustion due to different recycle ratio can have impacts on the total emissivity of gas and ultimately the radiation heat of oxy-furnaces.

The burner employed for the advanced O_2 injection tests was the triple concentric burner (configuration A) described in detail in a previous Topical Report (Wendt et al. 2012). The triple concentric burner allowed a primary pulverized coal stream transported by CO_2 to exit from one opening, a pure O_2 stream to exit from another opening, and a stream containing both O_2 and CO_2 to exit from the third opening. The pure oxygen stream is denoted as the directed oxygen stream and was dedicated to contain a specific percentage, up to 100%, of all the oxygen required for combustion for the combustion operating condition being investigated. The primary stream carries pulverized coal particles into the chamber and, as noted above, contained only CO_2, with no oxygen. Directed oxygen and transport streams were at room temperature. The secondary stream was a mixture of O_2 and CO_2, and played a significant role in moderating the combustion temperature as well as aerodynamically controlling entrainment of the flame jet. The secondary stream temperature is controlled at 489K using a gas preheater. Coal feed rate, primary stream CO_2 (30% of the total CO_2 required), stoichiometric ratio (1.15), and wall temperature (1283K) were all kept constant. The overall inlet O_2 varied from 40% to 60%.

Three WARs were employed in three different locations along the flame zone of the OFC to measure the heat flux from the flame and furnace wall. In parallel with these measurements, three thermocouples were installed in the furnace to measure the gas temperature. The change in total gas emissivity was investigated, and a radiation model was applied to relate the heat of radiation and the average gas temperature. Illinois #6 coal was used in these tests. Details of these tests can be found in Smith et al. (2014).

Tasks 17 - 22 – Oil Shale and Sands Program

Several tasks associated with the University of Utah's Oil Sands and Oil Shale Program (DE-FE0001243) were managed under the University of Utah's Clean and Secure Energy from Coal Program (DE-NT0005015) during phase one of the Coal Program. The Oil Sands and Shale Program addressed barriers to oil sand and shale deployment through a research program that ranged from the atomistic level to full-scale reservoir simulation and encouraged coupling and integration among the various scales (Tasks 17 - 20). Issues specific to carbon capture and water for these resources were addressed in Task 21 and 22, respectively. The tasks included:

- Task 17 – Kerogen/asphaltenes atomistic modeling. This task developed a representative three-dimensional model of the Green River oil shale kerogen. These computational results were correlated with experimental data that may include solid and liquid state 13C nuclear magnetic resonance spectroscopy, magnetic resonance imaging, thermogravametric data on pyrolysis kinetics, small angle x-ray scattering data on mineral matter and kerogen structure, and mass spectroscopy data.
- Task 18 – Multiscale thermal processing (pyrolysis) of shale. This task focused on developing kinetic and compositional data available for in-situ and ex-situ processing models and other applications. Experimental systems for both bench-scale pyrolysis and TGA experiments were developed. Comprehensive characterization was performed.
- Task 19 – Pore scale analysis of oil sands/oil shale pyrolysis by X-ray micro computed tomography and Lattice-Boltzman simulation. The significance of transport limitations in the recovery of oil by pyrolysis of oil sand/oil shale is an important consideration in the developing technology for utilization of these fossil energy resources. Computer tomography characterization of the pore network structure for selected oil sand/oil shale resources was performed. In addition, Lattice-Boltzmann simulations of flow through pore network structures were performed.
- Task 20 – Basin-wide characterization of oil shale resources in Utah and examination of in-situ production models. Using information on reservoir heterogeneity from core analysis, the task

evaluated how heterogeneity impacts resource production. This task also evaluated potential in situ production processes for further study.

- Task 21 – Oxy-gas combustion for CO_2 capture in thermal processing and upgrading of oil shale and oil sand. This task established a multi-scale, multi-physics, simulation-based, predictive tool aimed at quantifying predictive capability for oxy-gas burner simulations for CO_2 capture technology. The main outcome was the creation of enabling simulation technology to allow transition from air-fired furnace and heater operations to oxy-gas fired applications.
- Task 22 – Effect of oil shale processing on water compositions. The work involved performing pyrolysis experiments of Green River oil shale under different conditions (with representative of the amounts of water) and studying the resulting water chemistry. Emphasis was on the composition of the water generated. Hydrocarbons in the water phase were analyzed using gas chromatographic analyses.

The final project reporting for these tasks is being included under the Oil Sands and Shale Program.

RESULTS AND DISCUSSION

Task 3.0 – Oxycoal Studies

This report provides highlights of the project's oxycoal studies. Additional detail can be found in Wendt et al. (2011, 2014).

Subtask 3.1 – Oxy-Coal Combustion Large Eddy Simulations

Ignition mechanisms

LES coupled with DQMOM is able to capture complex particle behaviors such as particle dispersion or particle clustering. Figure 6 shows the normalized particle concentration (weight) profile for several different particle sizes. The small particles were strongly influenced by the gas-phase turbulence, and their jet spread faster than the medium and large particles. The large particle jet is only affected by the largest eddies and remains concentrated along the centerline. However, particle-clustering effects are observed for each particle size and play an important role in predicting flame characteristics as shown further.

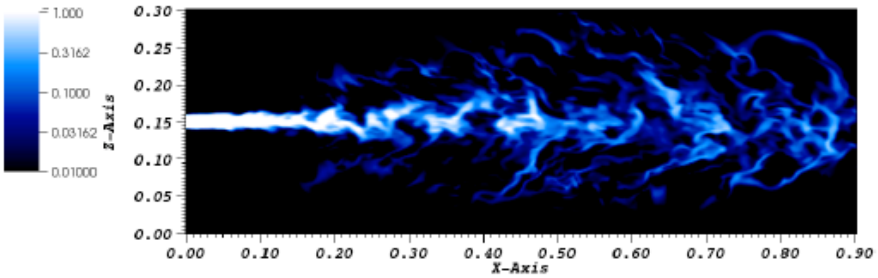

(a) Quadrature node 0 (40-micron particles)

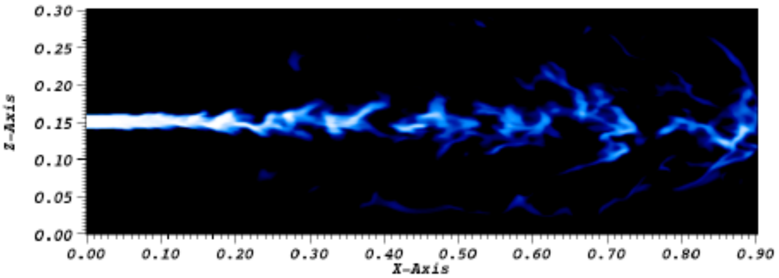

(b) Quadrature node 1 (63-micron particles)

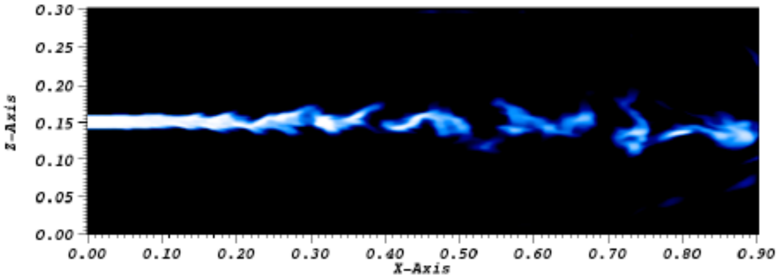

(c) Quadrature node 2 (100-micron particles)

Figure 6. Normalized weight (number of particles/m^3) of each quadrature node at a given time step of simulation 1.

V/UQ analysis

When considering flame stability, gas temperature was assumed to be a good indicator for flame ignition in the simulations. In the experiments, flame ignition was determined by optical measurements. Comparing optical measurements with the CFD results is a challenging task since the CFD code ARCHES does not predict emission in visible light. Nevertheless, the coal jet is assumed to be ignited when the gas temperature reaches 1850K, which is an increase of 50K from the highest wall temperature.

The simulation results showed that the wall temperature had a strong influence on the flame stand-off distance, whereas the primary oxygen concentration had no effect and the primary stream temperature had a moderate effect.

The consistency analysis revealed that the dataset was consistent. Therefore, there exists parameter values of H for which the model predicts all the experimental observations of the dataset within their specified experimental uncertainties. The collection of those values constitutes the feasible region and is shown in Figure 7a. The feasible region is a small subset of the hypercube with wall temperatures near 1200 K and primary stream temperatures below 400 K. Figure 7b compares the experimental uncertainty ranges to the model predictions. The uncertainty bars in red correspond to the image of the whole hypercube under the surrogate model, whereas the uncertainty bars in green correspond to the image of the feasible set. The red bars cover a large part of the experimental uncertainty range, which suggests that the uncertainty ranges chosen for the active variables were appropriate. On the other hand, the model prediction within the feasible set of parameter values (green bars) had a small uncertainty. According to the LES simulations and the data collaboration analysis, short stand-off distances can only be explained by high wall temperatures, whereas long stand-off distances require low wall temperatures.

Overall, data collaboration of experiment and simulation indicates that the ignition stand-off distance in this oxy-coal jet was not a strong function of the oxygen content of the primary stream as the experimental data alone would indicate but was predominately a function of the wall temperature in this small laboratory apparatus. Given the experimental data that were provided, the simulations and experimental data are consistent within the uncertainties of the experimentally measured stand-off distances and the uncertainties in the wall temperatures.

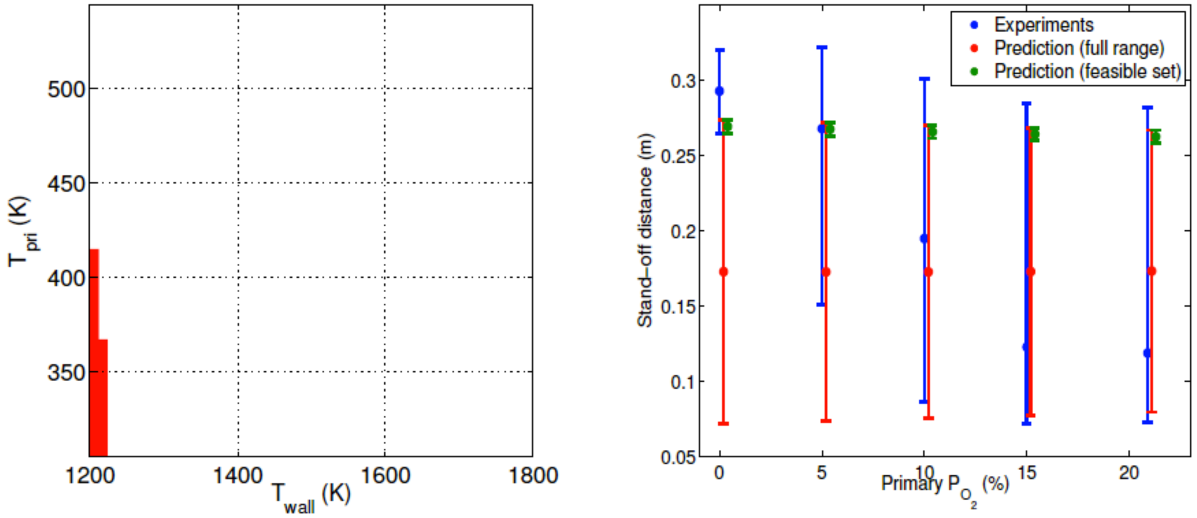

(a)

(b)

Figure 7. Feasible set of parameter values (a) and model predictions compared to experimental values (b).

Subtask 3.2 – Near-Field Aerodynamics of Oxy-Coal Flames with Directed Oxygen and Minimum Flue Gas Recycle

Effect of coal composition on flame stability

Several experiments explored the effects of coal composition changes on flame stability. The experiments were designed to understand the effect of oxygen in the primary stream for two coals at two different secondary preheat temperatures, 489K and 544K. The overall oxygen concentration was kept at 40%;

however, as the primary oxygen concentration changed, the amount of oxygen was deducted from the secondary stream and added to the primary stream. The flow rates in all the experiments of set A and B were identical. Comparing combustion of Utah Skyline and Illinois #6 coals at 489 K preheat secondary stream temperature and overall 40% oxygen concentration, showed that an attached flame was obtained from Illinois #6 coal at $P_{O2}=0.144$ in the primary stream. However, for Utah Skyline coal, the attached flame was obtained at $P_{O2}=0.207$ in the primary stream

When the temperature of the secondary stream was kept at 544 K during the experiment, the Utah Skyline flame was semi-attached flame w at P_{O2}=0.054, and it was fully attached at P_{O2}=0.099 in the primary stream. However, Illinois #6 coal had an attached flame at P_{O2}=0.144. Also, it is noticeable that the results of the Illinois #6 coal at 544 K preheat temperature did not change considerably compared to the results at 489 K of the secondary stream preheat temperature.

Additional experiments were devised to look at the importance of overall oxygen concentration in the furnace. The primary stream oxygen concentration was zero; however, the amount of oxygen in the secondary stream increased. The overall oxygen increased until an attached flame was obtained. The secondary stream temperature was kept at 489 K.

The TGA results supported the OFC findings. For example, Illinois #6 pyrolysis occurred at lower temperatures than Utah Skyline. Consequently experiments carried out at 489 K secondary stream preheat temperature showed increased flame stability for Illinois #6 with increasing the primary stream oxygen concentration. However, this effect was not significant for Utah Skyline coal.

Stability criteria for turbulent diffusion oxy-coal flames in an advanced triple concentric co-axial burner allowing directed streams of pure oxygen

In both configurations, placing increased amounts of the total oxygen in the directed pure oxygen stream amplifies the stability of the flame; however, this effect is considerably more significant when oxygen is located in the middle annular stream (Configuration A), rather than in the central pipe (Configuration B). For Configuration A, the stand-off distance of the flame does not change appreciably until F_{O2} = 64%. At F_{O2} = 75%, the first indications of a stable attached flame appear. The flame attachment is in a transient status at this point. However, at higher fractions of oxygen 85% and 100%, extremely stable and attached flames were generated. It is important to note that in the last condition, all the oxygen was located in a single stream.

For configuration B, flame stand-off distance diminishes with increasing F_{O2} in the central oxygen stream. However, the flame never became fully attached even when F_{O2} = 100%. These data show that injection of oxygen in the inner annulus creates more flame stability that when it is injected in the center of the burner.

For both configurations, flame length increased as the fraction of total oxygen placed in the directed pure oxygen stream increased. This increase in flame length was more significant with burners containing directed oxygen injection in the inner annulus (Configuration A). Although the stand-off distance for the cases F_{O2} = 85% and F_{O2} = 100% do not manifest a difference, the flame length PDFs show significant changes in the flame length for these two cases. By increasing oxygen fraction, the probability of the flames with a length longer than the window increased.

Subtask 3.3 – Advanced Diagnostics for Oxy-Coal Combustion

Small-scale particle PSV results

The PSV technique was successfully applied to a laboratory-scale coal burner, and it clearly identified the significant effect of altering the fuel-air equivalence ratio in that laboratory flame. For example, while flames with both equivalence ratios showed similar particle size distributions close at the burner surface, the distributions became quite different further away from the burner. The pulverized coal was a size-separated fraction between 70 and 90 mm. The fuel-lean flame ($\phi=0.25$) produced slightly bimodal particle size distributions above HAB=40 mm (HAB is height above burner). The coarser fraction corresponds to particles formed during pyrolysis. These particles were very elongated, thus the reasonably large diameters. The finer fraction corresponds to particles formed by the breakup of the elongated particles. Velocities generally increased with HAB. The fuel-lean flame produced faster moving particles in higher regions. In addition to particle size distribution and size, the PSV technique also was able to identify particle shape in the experiments.

Larger scale particle PSV results

Figure 8 shows the probability distributions of particle size, velocity and shape for Utah Skyline coal particles in two different combustion conditions and four different axial locations in the flame.
No apparent shrinking of the particles was indicated by the particle size distributions over the studied axial distance. Some swelling occurred indicated by slightly shifted modes in the distributions. The location where the highest mode occurred was affected by the oxygen concentration in the primary stream: the largest particles were detected around 20 cm below the burner in the 20% O_2 concentration case, while with 0% O_2, this location shifted to around 35 cm. In each case, after the swelling, particles began to shrink, indicating burnout and fractioning, but within the imaged portion of the flame axis, they did not shrink below their original sizes.

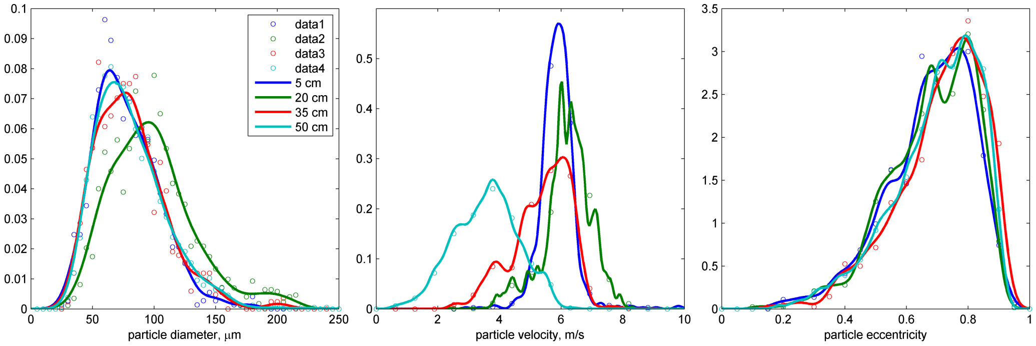

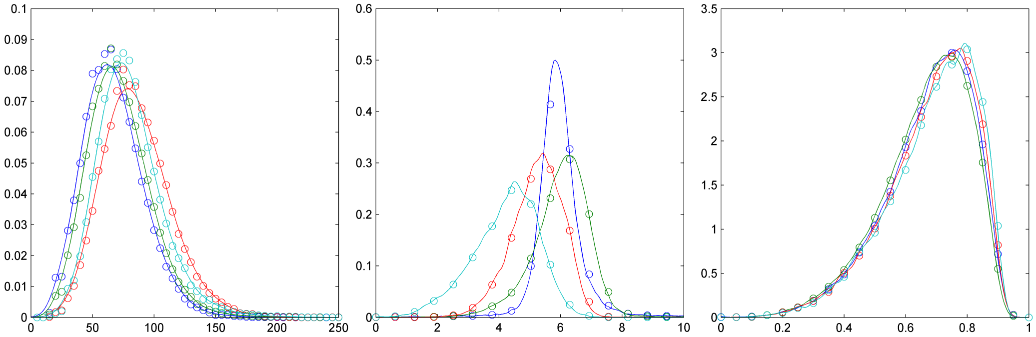

Figure 8. Particle size (first column), particle velocity (second column) and particle shape (third column) distributions in four different locations in the flame (denoted by the colors) and two different combustion conditions (top row – 20% O_2 in primary stream, bottom row – 0 % O_2 in primary stream). Fits are kernel density fits.

Particle velocities showed the same trend in both cases shown here: velocities started at around 6 m/s and increased slightly up to a maximum, from which they decreased to 4 m/s on average, as the axial coordinate increased.

There were no identifiable differences in the particle shape distributions. This means that the coal particles retained their initial shapes regardless of oxygen concentration and axial position. There were no identifiable elongated particles present in the flames, which we found in smaller scale flames. At this point, we hypothesize that the high shear rates in the turbulent flame disintegrated these elongated char particles before they could form.

Bivariate probability distributions of particle size and velocity indicated that there were no apparent correlation between particle size and velocity, which can be an effect of isotropic turbulence. Bivariate particle size – particle shape statistics indicated a slight correlation between the two in all cases, indicating that less spherical particles traveled slower, on average, than more spherical ones.

Figure 9 shows examples of PSV images taken of the OFC flames.

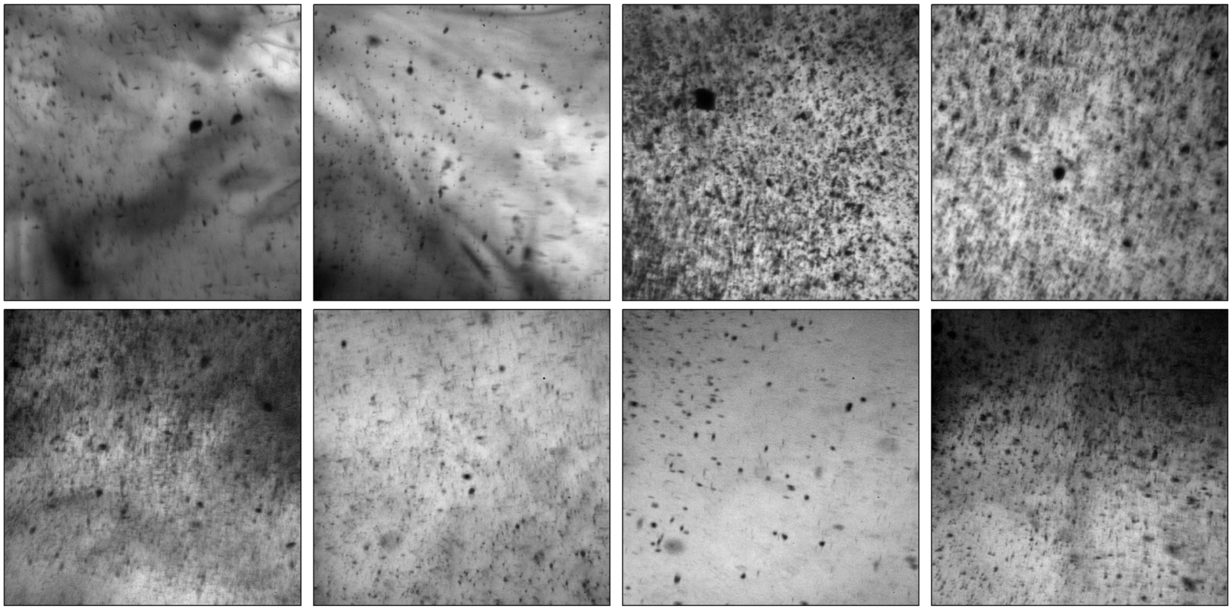

Figure 9. Examples of PSV images. Contrast and definition is much less ideal than that of small-scale images.

Flame velocity in the OFC

The high-speed camera tests consisted of analyzing flames of three different coals (Illinois #6, Powder River Basin (PRB) and Utah bituminous) with many different burners and many different operating conditions (for details of the burners, see subtask 3.2). An oxy-coal diffusion burner was used in the experiments presented here. For each coal type, the oxygen content was varied in the primary stream. The tested values were: 0%, 10% and 20% O_2.

From the displacement, the velocities were computed by multiplying the pixel displacements with the mm per pixels ratios of the images (computed separately for each set) and dividing by the interframe time. The results suggested that the velocity fields were strong functions of the coal type. While this may seem counterintuitive, the investigators noted that the velocities measured by our high-speed imaging method are the flamelet velocities. In other words, the measured the apparent travelling speed of luminous features in the images. This means that in order to have reliable measurements, many instances need to be photographed in which at a particular location a luminous flamelet can be observed. Furthermore, flamefront velocities are much more effected by local heat release than particle velocities, thus the effect of coal type (and differences in volatile content, volatile yield and moisture content) is understandable. Flamelet velocity follows gas velocity the most faithfully among the observable features.

Subtask 3.4 – Oxy-Coal Combustion in Circulating Fluidized Beds

SO_2 emissions in a pilot-scale CFB

The investigators compared the SO_2 emissions from the pilot-scale CFB with those from the bench-scale BFB for both air-firing and oxy-firing cases. Pilot-scale SO_2 concentrations (in ppm) are compared for both air- and oxy-fired cases in Figure 10. It is apparent that the oxy-fired experiments (26% O_2)

produced higher SO_2 concentrations (600-1400 ppm) relative to the air-fired case (200-400 ppm). The SO_2 emissions are 2-4 times higher during the oxy-fired combustion. Since a large fraction of flue gas recycle (FGR) is utilized in the oxy-fired case, SO_2 in the flue gas is recycled into the CFB, which increases the SO_2 concentration (ppm).

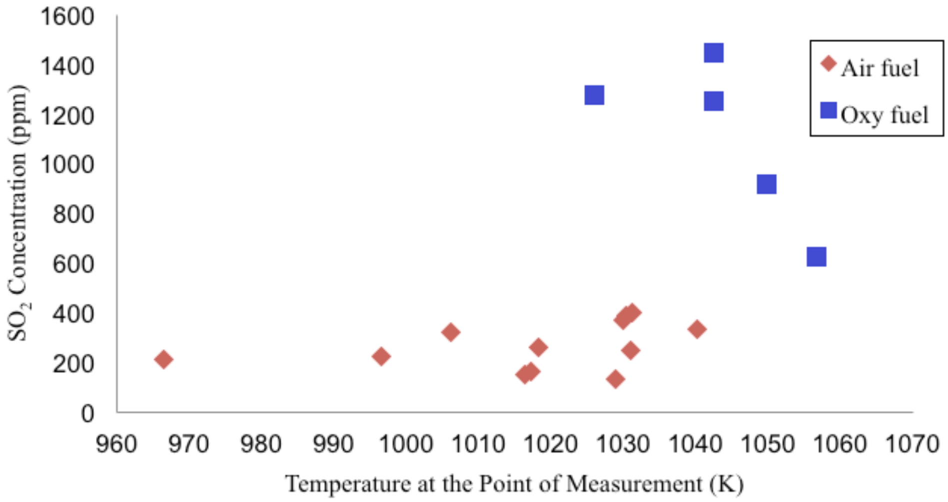

Figure 10. A comparison of SO_2 concentration (in ppm) in a pilot-scale CFB.

The mass-based SO_2 emissions for oxy-fired combustion are slightly lower than air-fired combustion. In general, one would expect about the same total mass of SO_2 produced in both cases since the same amount of fuel sulfur is introduced to the system. There are several possible explanations for the decrease in SO_2 mass emissions under oxy-firing, as there are a number of differences between air- and oxy-firing in a circulating fluidized bed combustor. The primary diluent in the oxidant stream is changed from N_2 to CO_2, which may have an impact on the sulfur conversion during combustion. The use of flue gas recycle increased SO_2 concentrations, which might have also affected the net sulfur conversion.

To address the impact of the primary diluent in the oxidant stream, the investigators utilized the results obtained from carefully controlled bench-scale experiments that were designed to evaluate this. In addition, a series of chemical equilibrium calculations were performed to provide further insights.

With regard to the impact of increased SO_2 concentration due to flue gas recycle, it is possible that the increased SO_2 concentration (part per million, ppm) in the oxy-firing case could enhance the ability of SO_2 removal by ash material in the fluidized bed. Data obtained during a bed temperature excursion in oxy-firing mode, clearly indicated an accumulation of sulfur capture by residual ash mixed with the bed material, as demonstrated by a sudden spike in SO_2 concentration when the bed was heated to a substantially higher temperature (high enough for the decomposition of any sulfate or sulfites formed with ash minerals). The SO_2 concentration was being monitored by two different analyzers during this test, and both of the analyzers exceeded their concentration limits. After some time at the elevated bed temperature, the SO_2 concentration started to decrease once again, after the captured sulfur had been released. This behavior clearly indicated that sulfur was being retained by ash minerals in the fluidized bed. With regard to observations of these phenomena at bench-scale, the investigators are unable to gain additional insights on this mechanism from those experiments, as the residual ash material from those tests was not analyzed for sulfur.

SO_2 emissions in the bench-scale BFB

In this bench-scale work, the impact of CO_2 versus N_2 on SO_2 evolution was investigated, as a means of elucidating any fundamental differences between those two gases as the "background" or combustion diluent with O_2 levels at 10, 20 and 30%. Highlights of the 30% O_2 case are provided, but the overall observations were similar for the 10 and 20% cases.

The results show that SO_2 is released mainly within the first minute of the BFB experiment; however, the full burnout of the char requires a few minutes, depending on experimental conditions. It is interesting to note that sulfur evolves more rapidly than carbon during single particle fluidized bed coal combustion. The SO_2 emission reaches a maximum level between 6 to 12 seconds, and decreases when sulfur is depleted. SO_2 emissions were similar between the two atmospheres (CO_2 versus N_2). Note that the bench-scale tests were performed in the absence of any recycle of combustion products, in contrast to the pilot-scale oxy-firing tests. Results at other oxygen concentrations, also at the same 4 temperatures, showed similar results.

The SO_2 evolution curves were integrated for each of the 4 temperatures and 3 oxygen concentrations investigated, and that information was used to determine the total amount of SO_2 evolved during each experiment. Total SO_2 emissions increased with temperature for both air and oxy-fired combustion in the bench-scale bubbling fluidized-bed reactor (in the absence of recycle). The lower emission values at lower temperatures may be a result of higher sulfur capture by the ash in the bed. However, some sulfur can remain in the char if the particles are not completely burned out at lower temperatures.

SO_2 emissions estimated by an equilibrium model

The investigators used the NASA Chemical Equilibrium with Applications (CEA) program to calculate SO_2 emissions under conditions representative of the bench-scale tests. The impact of the two combustion diluent mixtures of CO_2/O_2 or N_2/O_2 on SO_2 emissions were evaluated over the temperature range 600-1100 ºC and oxygen concentrations of 10, 20 and 30%. These equilibrium predictions support the conclusions derived from the bench-scale tests, that the diluent species (CO_2 or N_2) had no impact on the SO_2 emissions. The equilibrium predictions also provided information on the effect of temperature on SO_2 concentration. SO_2 emissions increased with an increasing temperature in the temperature range of 600-1100 ^{o}C, while SO_3 emissions decrease with increasing temperature in this same temperature range. SO_3 is thermodynamically favorable at lower temperatures; however, kinetic limitations prevent formation at such significant concentrations. SO_3 levels in the bench-scale experiments were below our detection limits, and in the pilot-scale tests the emissions were in the range of 0-7 ppm for air-fired conditions (no recycle - as with the bench-scale tests) and 8-63 ppm for oxyfiring (due to the use of recycle).

Subtask 3.5 – Single-Particle Oxy-CO_2 Combustion

Single-particle CFB

Experiments for limestone sulfation were carried out under air-firing and oxy-firing conditions at different temperatures. Under air-firing conditions, limestone sulfation displayed insignificant temperature dependence in the range of 765–874 °C, suggesting that SO_2 diffusion limitations could be significant. In sharp contrast, under oxy-firing conditions the degree of limestone sulfation was a much stronger function of temperature, implying that the reaction is under more of a kinetic control regime. At 765 °C, the sulfation rate under oxy-firing conditions is lower than under air-firing conditions. In contrast, at 874 °C, the sulfation rate under air-firing conditions is higher in the range of 0–2000 s but decreases slowly, and was observed to be lower afterwards, as compared to oxy-firing conditions. A possible explanation is that under air-firing conditions, limestone calcination is favored and indirect sulfation mechanism dominates with higher sulfation rate, such that a dense surface product layer was formed as barrier causing a SO_2 diffusion limitation. Hence, the results display insignificant temperature dependence. In sharp contrast, under oxy-firing conditions, limestone calcination appeared to give way to direct limestone sulfation. Direct sulfation displays a lower reaction rate and would lead to less product formation on the particle surface, and thus SO_2 could penetrate more effectively into the particle. Therefore, the reaction is more kinetically controlled and would show more noticeable temperature dependence. This hypothesis is consistent with the observation that the sulfation reaction under oxy-firing conditions (i.e., direct sulfation) displays a higher reaction rate than that under air-firing conditions (i.e., indirect sulfation) after a long period (i.e., 2000 s), due to the ability of SO_2 to continue to diffuse into the particle in the absence of the dense surface product layer that is formed under air-fired conditions (indirect sulfation).

SEM analysis was used to identify the microstructures of sulfated limestone and further clarify limestone sulfation mechanisms under air-firing and oxy-firing conditions. Under air-firing conditions a clear product layer (i.e., $CaSO_4$) was observed on the edge of the particle surface, while under oxy-firing conditions, the SEM image did not show any distinct product layer. For oxy-firing conditions, the limestone appears fairly uniform throughout the particle, with some apparent porosity.

Single-particle char oxidation

Effect of gasification rate coefficients on particle temperature and species profiles

The investigators considered the char carbon consumption rates for a 100 μm diameter char particle burning in oxy-fuel combustion environments as functions of the H_2O and CO_2 gasification rate coefficients. For both wet and dry combustion cases, the carbon consumption rate was strongly dependent on the CO_2 gasification rate coefficient, whereas the steam gasification rate coefficient only has a significant influence for a relative rate coefficient greater than one. For the wet-recycle cases, the contours have a greater dependence on the H_2O gasification rate coefficient because the higher steam concentration increases the steam gasification rate. The steam gasification rate coefficient (relative to the CO_2 gasification rate coefficient) has less influence on carbon consumption as the oxygen concentration increases, for both the dry- and wet-recycle cases. Because the activation energy of the CO_2 gasification reaction is higher than that of the steam gasification reaction, at high oxygen concentrations (resulting in high particle temperatures), the CO_2 gasification rate will increase faster than the steam gasification rate. Thus at higher oxygen concentrations the steam gasification reaction becomes relatively less important.

The relative contributions of oxidation, CO_2 gasification and steam gasification to carbon consumption are shown in Figure 11. With 12% oxygen in the bulk gas (which yields relatively low reaction temperatures), gasification reactions (with CO_2 and H_2O) are responsible for about 20% of the carbon consumption. At 36% O_2 in the bulk gas, these gasification reactions account for about 31% of the overall carbon consumption. Inspection of the right panel as compared to the left shows that exchanging some (0.11 atm) of the CO_2 for H_2O causes the relative carbon consumption due to steam to nearly double while only slightly decreasing the relative consumption from CO_2, and results in a net increase in the relative carbon consumption from gasification reactions. The relative consumption from oxygen also decreases slightly while the surface temperature increases by a few degrees as the steam concentration increases.

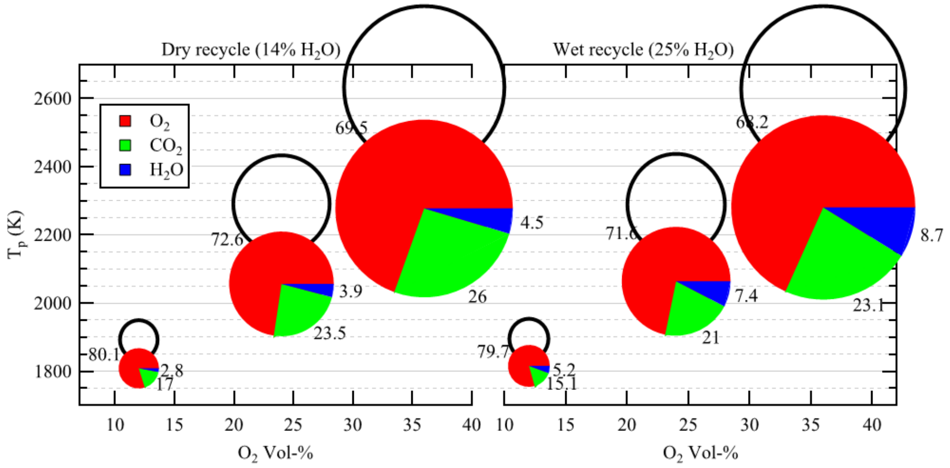

Figure 11. Relative contributions to carbon consumption by reactions with oxygen, carbon dioxide, and steam. Size of circle is proportional to overall carbon consumption rate, and percentages of contributions are shown on the chart. Open circles show particle surface temperature and relative carbon consumption rate without gasification reactions (only oxidation), and filled circles include gasification reactions at our best-guess rate coefficients.

Figure 11 highlights the complex interplay between the heterogeneous reactions occurring during the oxy-combustion of pulverized coal. If gasification reactions are not considered, nearly 400 kJ/mol_C is released by the oxidation reaction, leading to predictions of high particle temperatures shown by the open circles in Figure 11. When the endothermic gasification reactions are included, the enthalpy released by the heterogeneous reactions drops significantly, resulting in considerably lower predicted particle temperatures.

Comparison of detailed SKIPPY model to simplified models

Using the same char parameters for the single-film, the dual-film and continuous-film (SKIPPY) models, small differences were identified in temperatures and mole fractions between the single-film model and SKIPPY were identified, likely due to simplifications made in the single-film model. One simplification is that an effective diffusivity rather than a multi-component diffusion description allowed the species diffusion equations to be decoupled. Secondly, diffusivity and other transport properties are evaluated at a mean temperature, which may not be representative of the entire boundary layer temperature. Finally, the Thiele description for reactant penetration is only valid for one species reacting in a cylindrical pore, whereas in these simulations, three species are reacting with the solid carbon, and CO_2 is both a product and a reactant. Nonetheless, under these conditions, the two models agree well. In addition, the carbon consumption rates predicted by the continuous-film model (SKIPPY) are most closely matched by the single-film model over the entire range of conditions studied. The SKIPPY model without homogeneous chemistry also agrees well with the full SKIPPY model at low oxygen concentrations, but both the temperature and carbon consumption rates begin to diverge at the higher oxygen concentrations. The errors between the single-film models and the full SKIPPY model are larger with nitrogen as a diluent as compared to CO_2 and as the bulk O_2 concentration increases, but the differences between the models are not a strong function of particle size. The largest error in temperature between the single-film model and the continuous-film model is 270 K for a 60 μm particle with 60% O_2 in the bulk gas and N_2 as the diluent. The largest relative error in carbon consumption rate between the single-film and continuous-film models is 15.3% for a 135 μm particle with 36% O_2 in the bulk gas and N_2 as the diluent.

The double-film and continuous-film models also showed some similar trends. Reactions in the boundary layer release heat. For the continuous-film model, the temperature still decays away from the particle surface but is higher than the single-film model temperatures throughout the boundary layer. Meanwhile the double-film model has a temperature peak at the flame front. Boundary layer reactions increase the concentration of CO_2 and decrease the concentration of O_2 available to react at the particle surface. These reactions drive the concentrations of H_2 and CO to zero at a point closer to the particle surface than the single-film models.

Experimentally measured temperatures

The gas temperatures were measured in each of the different environments. As particles were reacting, temperature measurements were made at 3-7 heights of roughly 100 char particles. The results showed a significant spread in the particle temperatures, caused partially by measurement error (estimated at ± 20 K), but mostly by different reactivities, and variations in size of individual char particles. As the residence time in the reactor increases, there is a heat up of the particles, and then they tend to react at a fairly steady temperature, if not decreasing slightly as the residence time gets longer. Comparing all of the chars reacting in all of the environments, the maximum temperatures for a given particle size tended to correlate with higher combustion reactivity.

The more reactive sub-bituminous PRB char burns at a higher temperature than either of the two bituminous chars, which burn at about the same temperatures in all of the different environments. There is some dependence of temperature on particle size. For the Black Thunder char, the temperature seems to peak around 80 μm, while the Utah Skyline and Illinois #6 char temperatures increase (although they appear to level off) up to the largest particle size. A trade off exists between heat losses and available reactive surface area, leading to the dependency of temperature on particle size.

At both 24 and 36% O_2, there is an obvious influence of diluent on particle temperature. Particles combust about 100 K hotter with the N_2 diluent than with the CO_2 diluent. However, at 60% O_2, there are no obvious trends in temperature either due to diluent or steam concentration.

Kinetic fits

Optically measured temperatures were used to find kinetic fits for each of the chars. The kinetic parameters were able to match the experimental data reasonably well for the Black Thunder char, but the temperature predictions for the two bituminous chars were significantly lower than the experimentally measured values.

For the oxidation reactions, the activation energy found for the two bituminous chars is near the lower bound of 150 kJ/mol for oxidation to CO and significantly lower than the activation energy found for the sub-bituminous char. The lower activation energy is a lower barrier for a reaction to occur, `turning on' the reaction at a lower temperature. However, pre-exponential factors for the oxidation reaction of the bituminous chars were also nearly an order of magnitude lower than the pre-exponential factors for the sub-bituminous char, meaning the reaction proceeds at a lower rate at higher temperatures.

The oxidation rate coefficients for the three chars had the same value around 1200 K, and faster for the Black Thunder char at higher temperatures. The bituminous chars have an order of magnitude lower CO_2 gasification rate coefficient than the sub-bituminous char, and very similar H_2O gasification rate coefficients.

Comparing the maximum combustion temperatures to the experimental data, many of the experimentally observed trends in temperature also occur during the simulations, although the magnitudes of the temperatures show some disagreement. All of the char particles react at higher temperatures when N_2 is the diluent as compared to CO_2, and the differences in temperatures between the two diluents are similar, perhaps with the exception of the reactions in 60% O_2. Secondly, the maximum measured temperatures peak at a similar size in the simulations and the measured data. Finally, the predicted temperatures for the sub-bituminous char are higher than the predicted temperatures of the bituminous chars. Predictions for temperatures in 60% O_2 are high and for 24% O_2 are low, but overall, these kinetics capture the experimentally observed trends.

Parametric analyses

With the kinetics in hand, comparisons can be made between the temperatures and burnout characteristics across the parameters varied in these studies. As expected due to their ranks, the sub-bituminous Black Thunder char reacts at the highest temperatures and burns out in the shortest residence time. With the same kinetic parameters, the simulated temperatures and burnout characteristics of the Utah Skyline and Illinois #6 chars are very similar. Fairly good agreement between the experiments and simulations were found. The particles take more time to heat up in the simulations than experimentally, this is likely due to the large uncertainty in the heat capacity of the chars, and the fixed value of this parameter.

Subtask 3.6 – Ash Partitioning Mechanisms for Oxy-Coal Combustion with Varied Amounts of Flue Gas Recycle

Laboratory-scale studies

Comparing O_2/N_2 and O_2/CO_2 combustion conditions, the particle temperature in O_2/N_2 was estimated to be higher than that in O_2/CO_2 at the same gas temperature and oxygen concentration conditions. The most likely reason is that the mass diffusivity of O_2 in CO_2 is lower than that of O_2 in N_2 which inhibits the oxygen at the particle surface.

Typical PSDs for the higher gas temperature condition, 1520K, are shown in Figure 12 for the three coals. As seen in this figure, there were three modes of particles: ultrafine, less than 0.1 micron; fine, 0.1 to 1.0 micron; and coarse, greater than 1 micron. Illinois #6 had the most defined segregation between modes. The mean size of each particle mode was determined and the SMPS and APS PSD data were integrated to obtain total mass for ultrafine, fine, and coarse modes. Results were normalized to 1000 mg of ash. As illustrated in Figure 12, the diameter and mass for the coarse modes (particles greater than 1 micron) did not change for the three coals. This result is expected since particles in this size range are usually the result of particle attrition. Changes in the ultrafine and fine modes were found for all three coals under the different conditions. In these ranges, particles are formed from volatilization and subsequent condensation and/or nucleation and coagulation (Khatami, et al. 2011). These steps are more dependent upon the temperature and gas-phase environment.

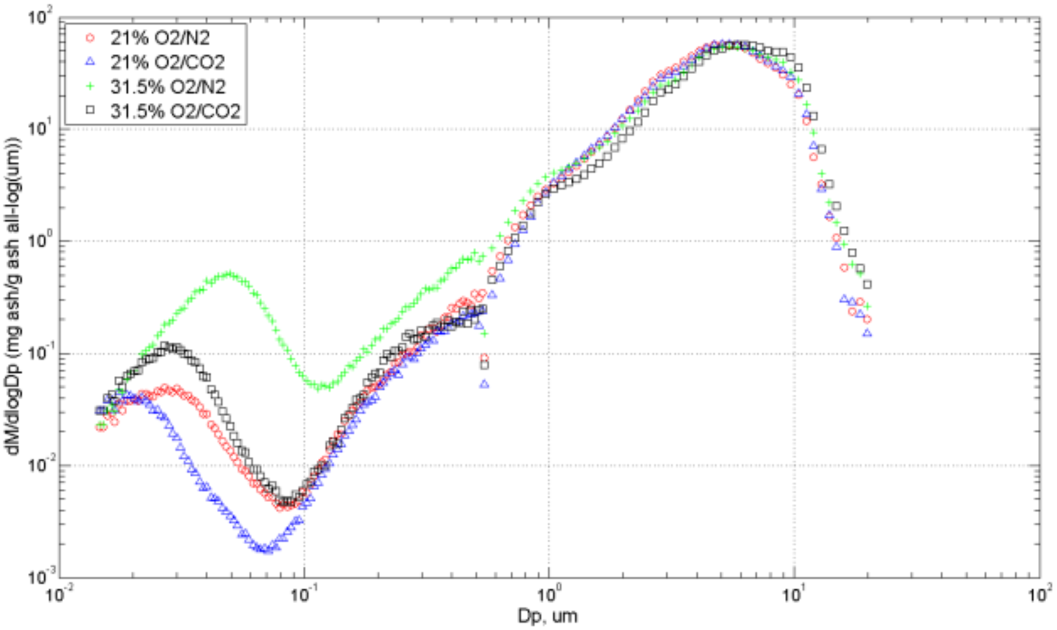

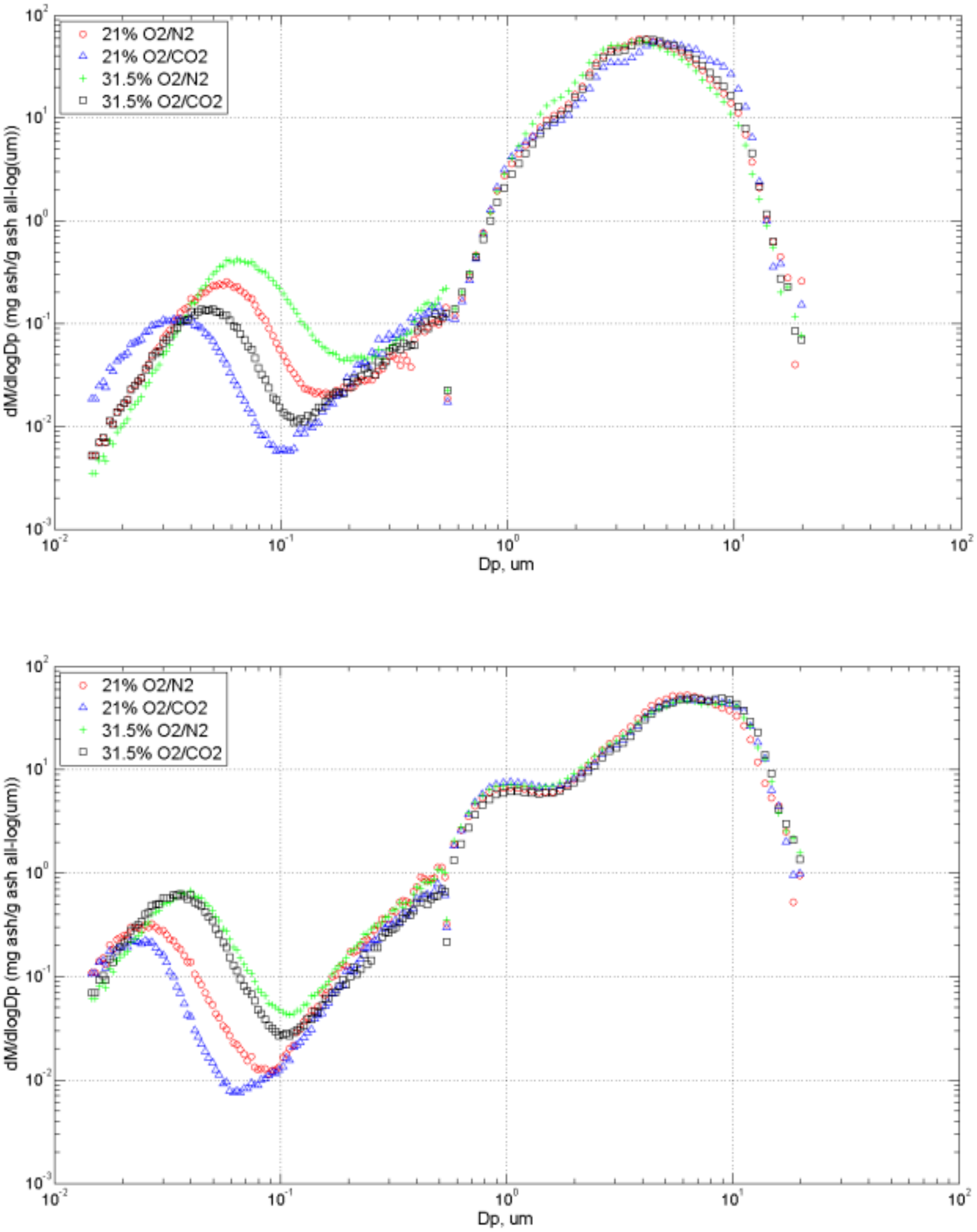

Figure 12. PSDs of Utah Skyline (top), PRB (middle) and Illinois #6 (bottom) at higher furnace temperature with a gas temperature of 1520K.

Utah Skyline showed a significant increase in ultrafine particle mass concentration with temperature. The data for PRB are more scattered but also show a slight increase with temperature. Illinois #6 had the highest ultrafine mass concentration of the three coals. This coal had a high concentration of sulfur, and the ultrafine mass was relatively consistent over all conditions, with the exception of one point. This is likely due to the vaporization of the sulfur, which would be independent of temperature and gas environment at these conditions. Both Utah Skyline and PRB coals show a second-order effect of CO_2 at the higher temperatures where, for the same temperature, the mass of ultrafine was lower for the CO_2 condition versus the N_2 (comparing dark and light bars). This result is due to the high content of silica in the Utah Skyline and calcium and silica in the PRB. These compounds would be expected to have the hypothesized relationship with CO_2 where the reaction is driven toward the solid oxide not a reduced vaporized oxide.

The mass concentration of the fine mode did not vary significantly except at the highest temperature for the Utah Skyline coal. The fine mode mass concentrations of Illinois #6 were much higher than the other two coals in this mode.

Figure 13 shows the results from the BLPI and energy-dispersive spectroscopy analysis for the Utah Skyline coal with the three modes, ultrafine (< 0.1 micron), fine (0.1-1.0 microns), and coarse (greater than 1 micron) indicated by the lines. The shapes are similar to the SMPS/APS PSD data of Figure 12. As previously discussed, Utah Skyline contains a high Si content. The mass fraction of SiO_2 was the highest in the coarse mode (from 1.98 to 7.33 µm). As expected, the amount is relatively consistent in this size range. The highest temperature is for the 31.5% oxygen/nitrogen environment. As seen in the figure, the amount of ultrafine is higher across the stages and silica is in higher concentrations for this condition. The fine mode also shows enrichment in silica for the highest temperature case.

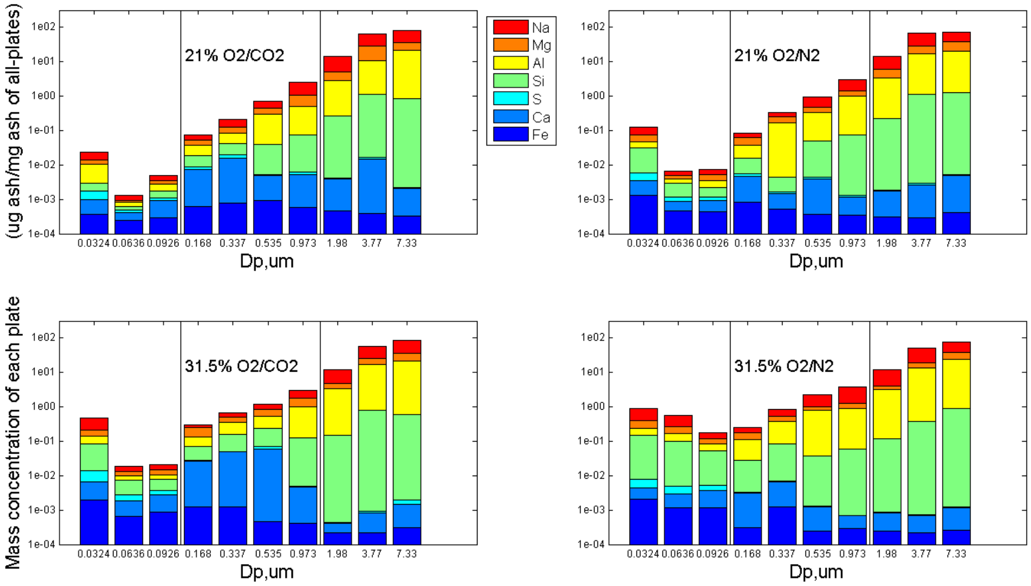

Figure 13. Elemental mass fraction size distribution of Utah Skyline at 1520K gas condition. The lines show the three modes: ultrafine, fine, and coarse.

PRB coal has a high content of Ca and Si, and Ca is the predominant ash compound, as Ca is more easily vaporized than Si. Again, the highest amount of calcium was seen at the conditions of the lower, right graph. There is also slightly more silica in this case. The coarse fraction concentrations are also relatively constant.

Illinois #6 coal has a high content of sulfur, Si, and Fe. Large concentrations of sulfur were found in the ultrafine and fine particles, with almost no sulfur in the coarse mode. Si and Fe showed more dependence on O_2 concentration versus the combustion environment (N_2/CO_2) for all stage samples. These results are consistent with the fact that the sulfur was easily vaporized at the temperatures studied.

The results suggest that the vaporization is controlled by temperature. Existing nucleation and coagulation models can be used to account for the effects, and a separate submodel was not developed due to time and funding constraints.

OFC studies

Ash aerosol PSD

For comparison and validation purposes, both the BLPI and SMPS/APS were employed for ash aerosol PSD measurement. An example of the ash aerosol PSDs is shown in Figure 14, which shows input-ash based PSDs (aerosol mass per unit input-ash (µg/g_ash) versus particle size (µm)), which helps elucidate ash aerosol formation mechanisms. Consistency in absolute concentration, relative concentration, and PSDs was observed between the data obtained through BLPI and SMPS/APS, which indicated high-quality data.

As shown in Figure 14, ash aerosol PSDs have three modes in all tested cases, these are: (i) vaporization-mode for particles that have nucleated from the metal vapor and are normally less than 0.5 µm in diameter, (ii) the fine fragmentation mode normally centered around 1 µm, and (iii) the coarse fragmentation mode normally centered around 10 µm. The figure suggests that switching from air combustion to oxy-coal combustion with different RFG options and amounts may not affect the ash aerosol formation mechanisms. However, the vaporization-mode peak shifts from 0.06 µm to 0.17 µm when switching from air and OXY27 to OXY50, whereas the other modes remain the same. This phenomenon could be caused by the higher combustion temperature in OXY50 because higher combustion temperatures enhance vaporization of minerals and subsequently increases the concentration of vaporization-mode particles. Consequently, the coagulation rate of the vaporization-mode particles will be largely increased because the turbulent coagulation rate is proportional to the square of the particle concentration. This process could help shift the vaporization-mode peak to a larger size. Although this process is difficult to observe in the DTF because of the large dilution, the lab-scale studies portion of this subtask obtained a similar result for PRB coal.

The results indicate that the total amounts of ash aerosol formed in OXY50 cases are not necessarily larger than those in air and OXY27 combustion, as demonstrated by Figure 14(c). Figure 14(c) shows that for the same amount of input-ash, OXY50 produces slightly more particles in the size ranges of 0.0926 µm to 0.535 µm (vaporization-mode) and similar for the rest size ranges. Therefore, compared with air and OXY27 combustion, OXY50 cases increase the formation of vaporization-mode particles due to higher combustion temperature from the perspective of ash-based ash aerosol formation.

Although different RFG amounts have an apparent effect on vaporization-mode particle formation, the RFG with different cleanup options seems to have an insignificant effect on ash aerosol formation, and they all show similar concentrations and PSDs.

Ash aerosol elemental compositions

The results show that for the same RFG amounts the elemental MSDs are similar for various RFG cleanup options, which implies the RFG cleanup options have no significant effect on ash aerosol chemistry. However, for different recycle amounts, the elemental MSD do show significant differences.

The mass fraction of Na is higher in OXY27 than in OXY50. This is due to the effect of high silicates in PRB coal and the higher combustion temperature in OXY50. Sodium reacts with aluminum silicates or silicates, forming sodium aluminum silicates or sodium silicates. High silicates and high temperature could enhance these reactions, which remarkably reduce the fraction of sodium in the vapor and submicron fume.

Sulfur is rich in vaporization-mode, and its mass size distribution is similar in both OXY27 and OXY50. However, its concentration is lower in submicron size range in OXY50. Typically, sulfur in ash aerosol is in the form of alkali and alkaline earth metal sulfates. Therefore, higher alkali and alkaline earth metal concentrations in air combustion could help retain sulfur; besides, elevated CO_2 partial pressure in OXY50 combustion may restrain sulfate formation.

The mass size distribution of silicon is similar in both OXY27 and OXY50 combustion, except for higher concentrations in OXY50 in the vaporization-mode, which is the consequence of the higher combustion temperature in OXY50. The mass size distribution of Mg is almost the same in both OXY27 and OXY50, which suggests the different RFG amounts do not affect Mg transformation. The distribution of Ca shows that Ca is higher in OXY50 than in OXY27, especially for the vaporization-modes, which may be caused by the higher combustion temperature in the OXY50 cases.

The distributions of Fe and Al present an apparent discrepancy between OXY27 and OXY50 combustion: they are evenly distributed in OXY27 but increase with particle size and concentrate at approximately 1 μm in OXY50. These results suggest a preferred chemistry status of Fe and Al compared with OXY27.

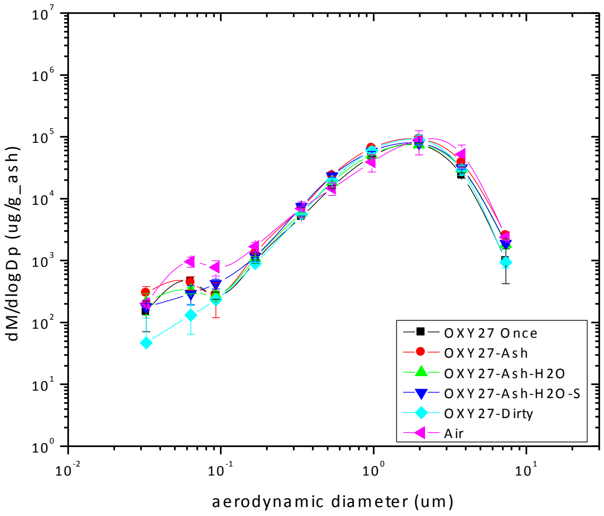

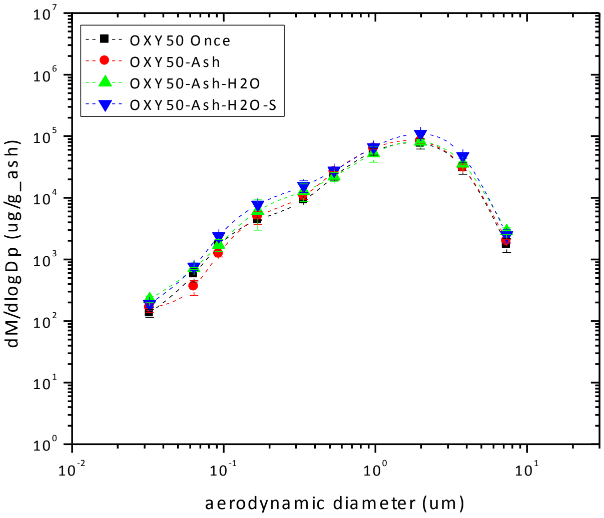

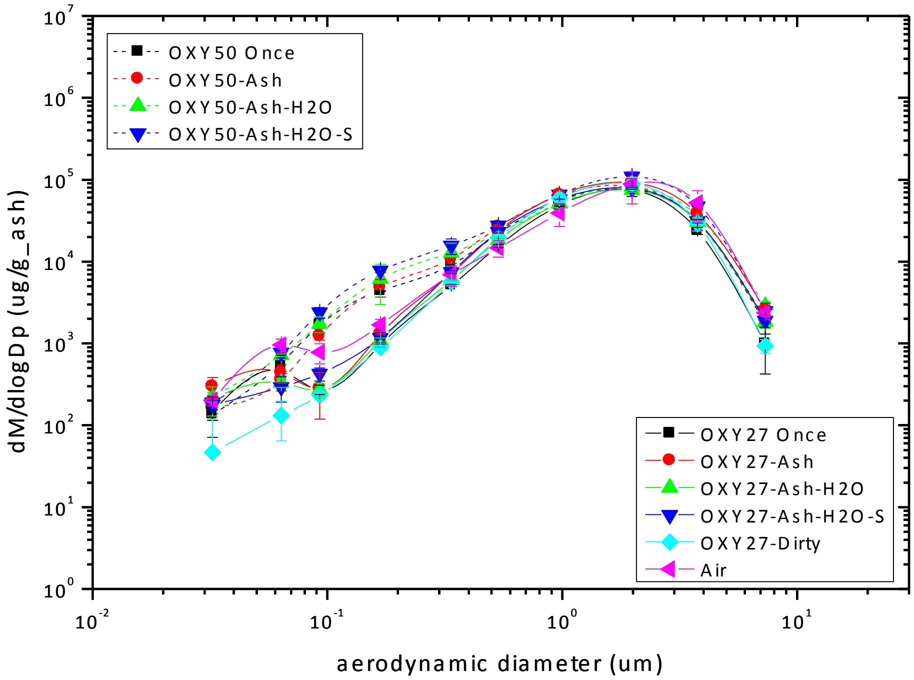

Figure 14. Ash based PSD from BLPI: (a) OXY27 and Air cases; (b) OXY50 cases; (c) all cases.

Task 4 Gasification Studies

This report provides highlights of the project's gasification studies. Additional detail can be found in Whitty et al. (2011, 2014).

<u>Subtask 4.1 – Entrained-Flow Gasifier Simulation and Modeling</u>

LES simulations for the BYU gasifier

After evaluating variables expected to be significant for BYU gasifier performance, four of these parameters were very clearly significant (devolatilization, reaction activation energy, wall temperature, coal mass flowrate, and mean particle size), while devolatilization reaction pre-exponential constant and char oxidation reaction activation energy were insignificant. Perhaps the most important observation was that the devolatilization reaction activation energy was not only significant near the inlet in the devolatilization zone, but that its effect propagated throughout the system, and it was the single most significant parameter throughout the entire gasifier.

LES simulations for the CANMET gasifier

The investigators completed a cold-flow LES simulation for the CANMET gasifier (Figure 15).

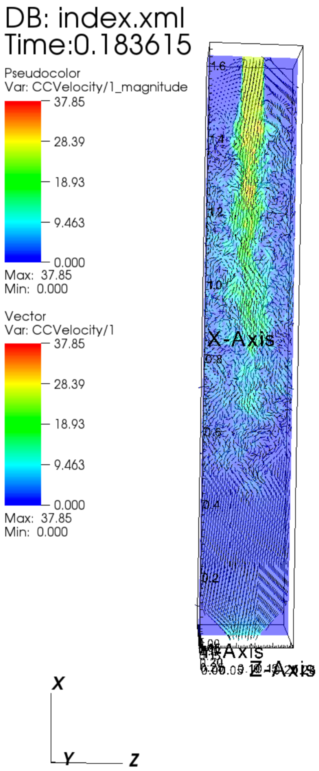

Figure 15. Flow fields and velocity vectors in the CANMET gasifier.

Equilibrium model for coal gasification

An equilibrium model was developed to study the effects of important operating parameters, such as carbon conversion, heat loss ratio and coal slurry concentration, on the gasifier performance. Figure 16, Figure 17 and Figure 18 show the effects of these operating parameters.

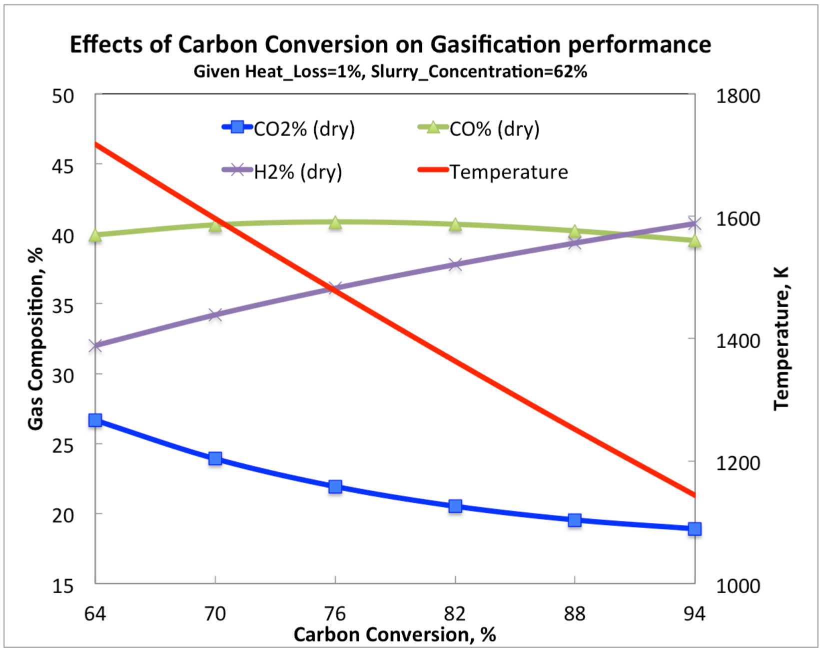

Figure 16. Carbon conversion effects on gasification.

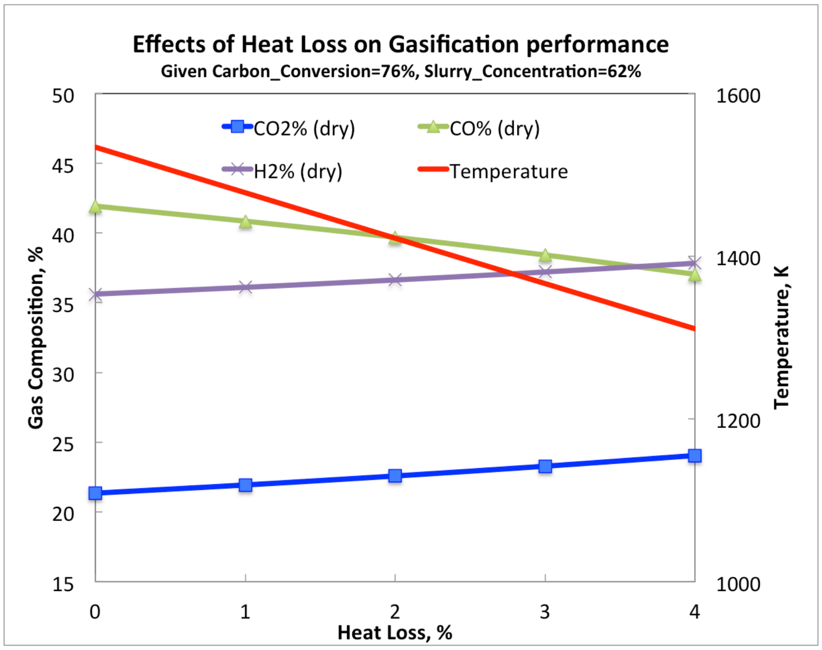

Figure 17. Effect of heat loss on gasification.

- 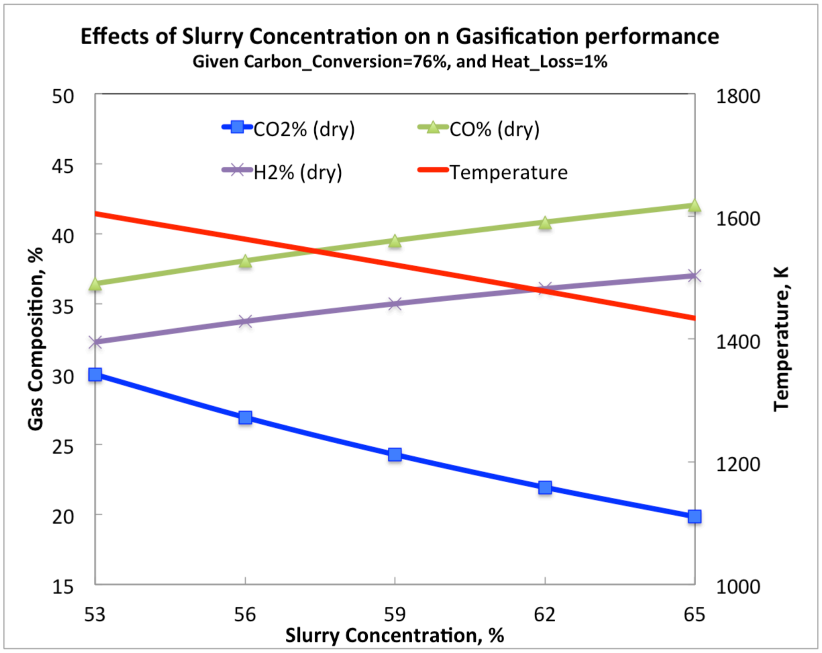

Figure 18. Effect of coal slurry concentration on gasification.

Comparison of these results with experimental data show that the results agree reasonably well with carbon conversion in the range of 64% to 84% and temperatures ranging from 1400 to1750 K.

Subtask 4.2 – Subgrid Mixing and Reaction Modeling

Simulations were performed to investigate the effect of furnace temperature, particle size and coal type on the predicted ignition delay of coal particles.

Ignition delay

There are different ways to validate the simulation predictions such as comparing the species profiles, flame stand-off, ignition delay, *etc*. In this work, the validity of models was examined by comparing ignition delay predicted by simulation and experimental data. An example of the ODT results show that furnace temperature has a significant impact on the particle's heating rate, which is illustrated in Figure 19. Black Thunder coal contains 11% moisture, which is almost one order of magnitude more than Pittsburgh coal's moisture content. Vaporization of this much moisture delays Black Thunder coal ignition compared to Pittsburgh coal. Considering the uncertainty contributed by the definition of ignition delay, the agreement between simulation predictions and experimental data is satisfactory.

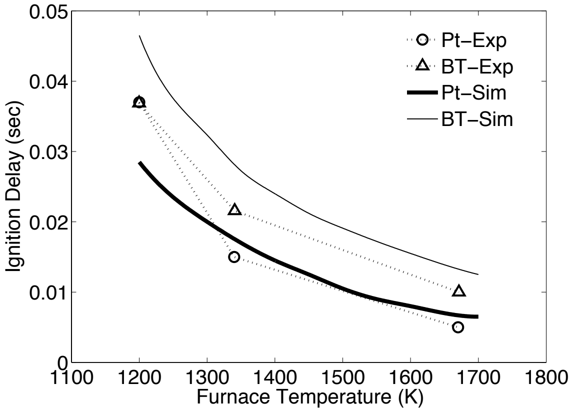

Figure 19. Ignition delay vs. furnace temperature for Pittsburgh (Pt) and Black Thunder (BT) coal particles injected into 20 vol% O_2 in N_2 diluent. Thick and thin lines represent Pittsburgh and Black Thunder coal types and simulation results, respectively. Dashed and solid lines show experimental and simulation results, respectively.

Subtask 4.3 – Radiation Modeling

Highlights of this subtask include the comparison of RMCRT with DOM in an industrial scale methane-fired boiler simulation. Results indicated that for a given level of accuracy, and a given level of parallelism, RMCRT calculations may require less computational time than the discrete ordinates method (see Table 10).

Table 10. Timing and accuracy of RMCRT and DOM SN8.

	Computational Time (s)	divQ L1 error norm	Q L1 error norm
Filtered RMCRT calculations	1033	1.07	.0311
DOM SN8 calculations	2949	2.05	.0271

Enhancement was carried out to allow the gas-phase absorption coefficients to be modified to include the effect of the coal-particle absorption coefficients. An oxy-coal furnace simulation was selected as a demonstration case for the new capability. Results are shown in Figure 20.

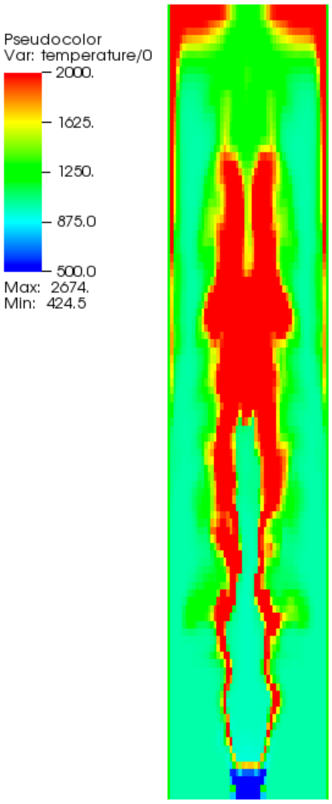

Figure 20. Temperature field of a center-slice of an oxy-coal furnace simulation. The radiation model used in this simulation incorporates entrained coal particles.

Subtask 4.4 – Char and Soot Kinetics and Mechanisms

First-order gasification model

Although more complicated models exist, the coal char mass release data from the gasification experiments in the HPFFB reactor were modeled with a first-order global and experimentally generated kinetic parameters. Figure 21 shows the prediction of mass loss of Illinois# 6 char due to CO_2 and H_2O after the first collection height at 1" at the 15 atm 1830 K steam condition. Published CO_2 gasification rates were used to account for the mass loss due to CO_2 at this condition. From the figure, it is easily seen that most of the mass loss of IL#6 coal char was due to steam gasification. The 15 atm 1830 K steam condition resulted in the highest mass loss due to CO_2 of all four steam conditions. Therefore, the mass loss due to CO_2 in any of the other 3 steam conditions would be less than that shown in Figure 21. Predictions of mass loss were also made for Utah Skyline coal.

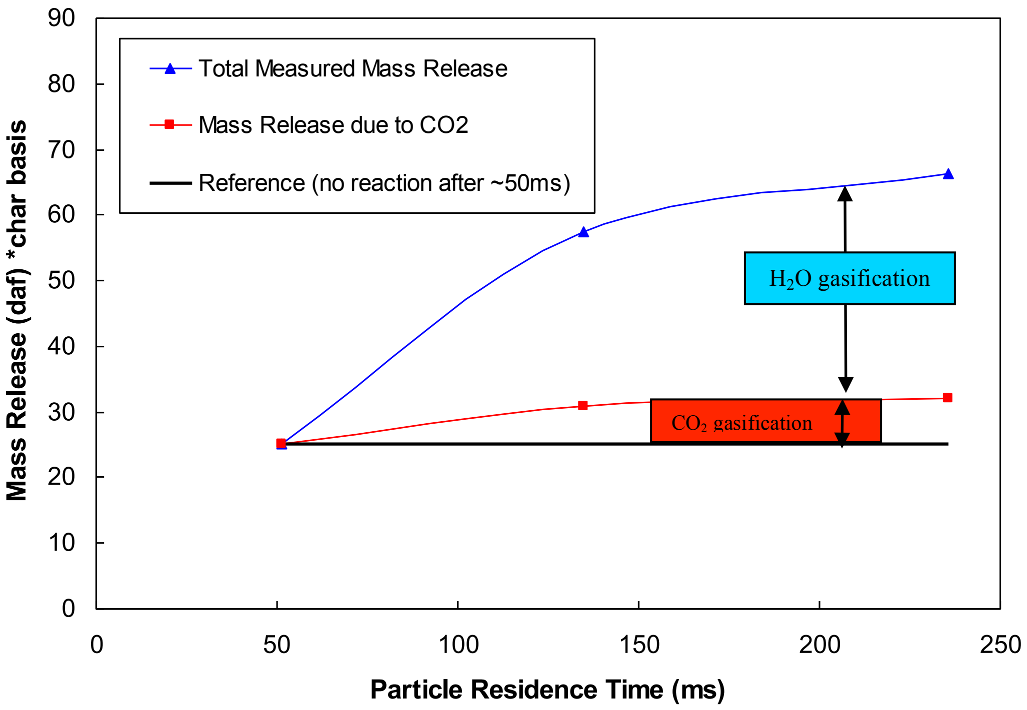

Figure 21. Effect of mass loss by H_2O and CO_2 gasification when feeding 75-106 µm IL #6 coal char in the HPFFB reactor at the 15 atm 1830 K steam condition.

The mass loss predicted for CO_2 gasification was accounted for using the first-order model, and any remaining mass loss was attributed to steam gasification, which was then used to regress first-order steam gasification kinetic parameters. The steam gasification data included mass release values from four gas conditions in the HPFFB at three residence times per gas condition, excluding the 15 atm 1611 K condition that only used 2 residence times. The maximum particle residence time of the measured data was about 240 ms. The activation energy, *E*, for steam gasification was kept at 121.3 kJ/mol for both Utah Skyline and Illinois #6 coal chars since changing *E* did not make any significant improvements to the model fit.

The parity plots shown in Figure 22 show how the measured mass release data (on a char basis) due to steam compared with that predicted by the first-order gasification model. The fits of the first-order model in Figure 22 are very reasonable considering the simplicity of the model.

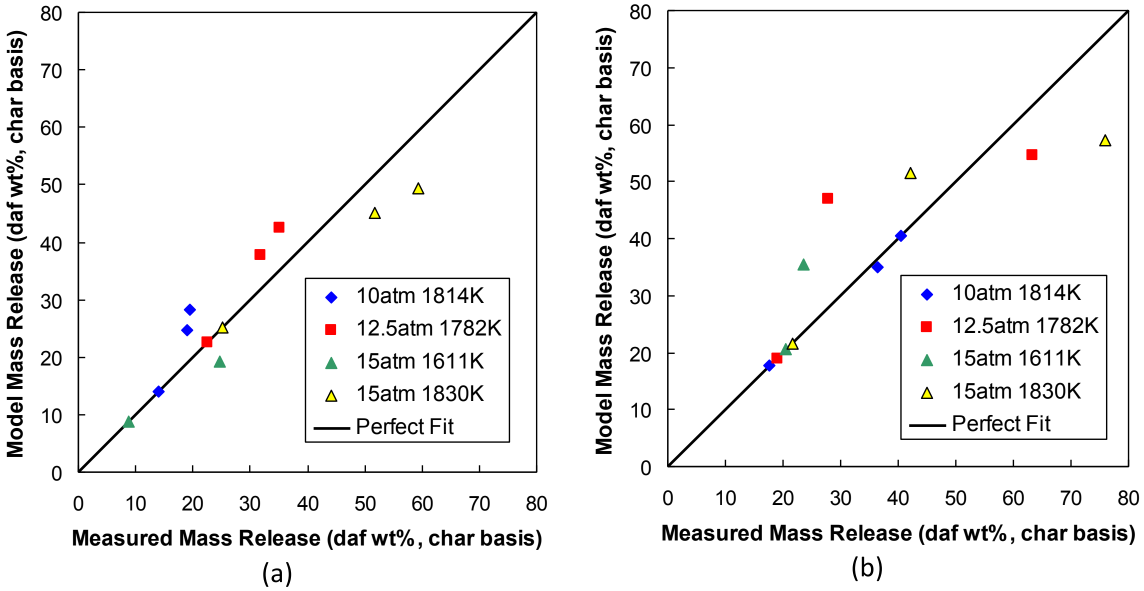

Figure 22. Parity plots of HPFFB H_2O gasification data for (a) Illinois #6 and (b) Utah Skyline coal chars using mass loss data attributed to H_2O gasification.

The gasification of a single coal char (75-106 µm Illinois#6) was studied in order to gain insight about the mass loss of coal char in the presence of both H_2O and CO_2. These conditions differed from the HPFFB steam conditions since CO_2 was present in much larger concentrations in these second set of conditions, which allowed CO_2 to account for a much higher fraction of the total mass release when compared to the steam conditions. Measured and predicted mass release values of the IL#6 coal char at the two H_2O/CO_2 conditions of the HPFFB reactor is shown in Figure 23. The prediction of the mass release values agreed well with the measured values at the 15 atm 1812 K condition.

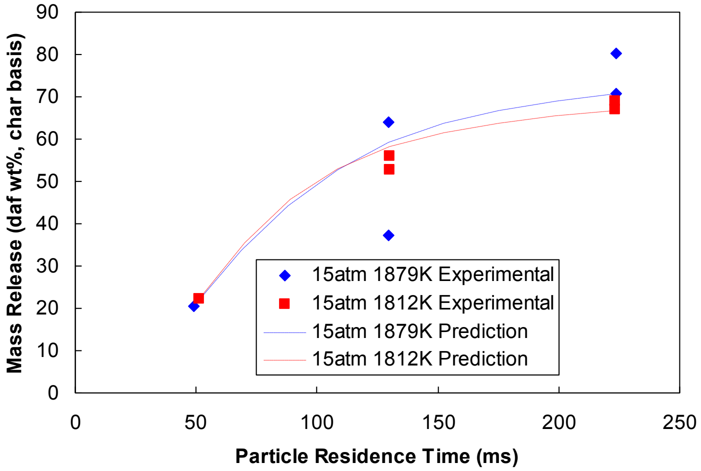

Figure 23. Measured and predicted values of daf mass release of IL#6 coal char at the H_2O/CO_2 conditions of the HPFFB reactor.

Although there was more experimental scatter in the 15 atm 1879 K data set (see Figure 23), the predictions of the first-order model seemed to agree well with the measured IL#6 mass release (excluding

1 data point at ~ 130 ms). Although the partial pressure of CO_2 at the 15 atm 1812 K condition was 2.5 times higher than at the 15 atm 1879 K condition, similar mass release values were measured at both conditions (see Figure 23) since rates are exponential with temperature and the 15 atm 1879 K condition was hotter. In conclusion, good approximations of mass release were obtained when using the first-order model and the kinetic parameters with the assumption that CO_2 and H_2O rates are additive.

Figure 24 shows the predictions of the first-order model for the distribution of mass loss due to H_2O and CO_2 gasification 15-atm pyrolized 75-106 µm IL#6 coal char was re-injected at the 15 atm 1812 K and 15 atm 1879 K H_2O/CO_2 HPFFB condition. Although the first-order model predicts similar *total* mass release of IL#6 coal char, it predicted that 62% of the total mass loss is due to CO_2 at the 15 atm 1812 K condition when compared to only 43% at the 15 atm 1879 K condition at particle residence times near 220 ms.

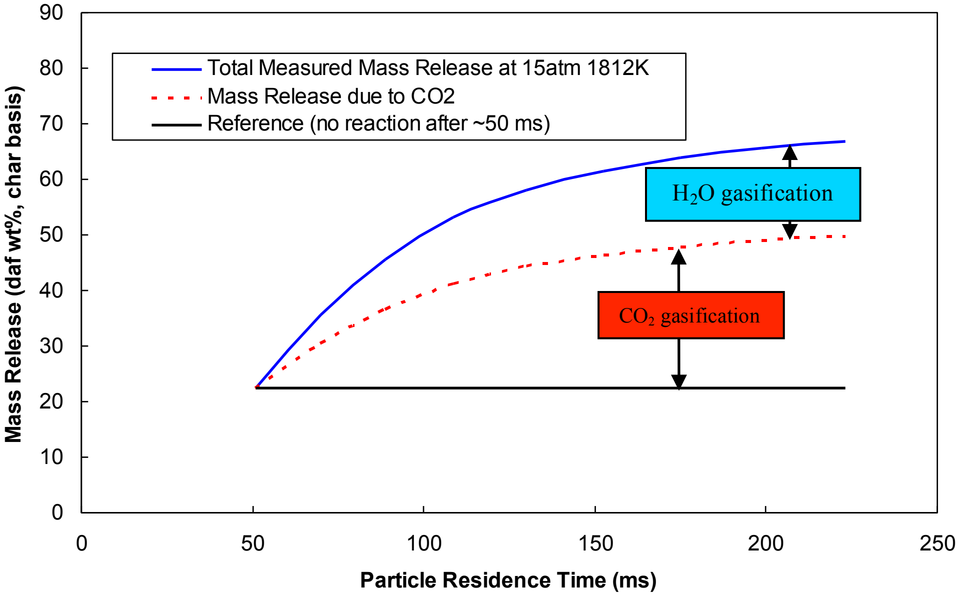

Figure 24. First-order model predictions for the distribution of mass loss caused by H_2O and CO_2 gasification using kinetic parameters for IL#6 char reacting at the 15 atm 1812 K H_2O/CO_2 HPFFB condition.

Coal swelling model

A first-generation atmospheric coal swelling model has been developed. The model was able to predict the trends in swelling with heating rate for bituminous coals. It is also able to predict shrinkage for subbituminous coals and lignites. It is important to note that no coals of ranks higher than low volatile bituminous were used to develop the correlation. Since the basic rank model for swelling is specifically targeted at providing reasonable estimates for high heating rates, comparison of the model to data from electrically heated experimental facilities requires that the effect of heating rate be considered. The heating rate exponent c_5 should be set to zero for anthracites, lignites, and most subbituminous coals to avoid predicting unrealistic swelling of these coals at heating rates near 10^4 K/s. The results of the regression are shown in Figure 25.

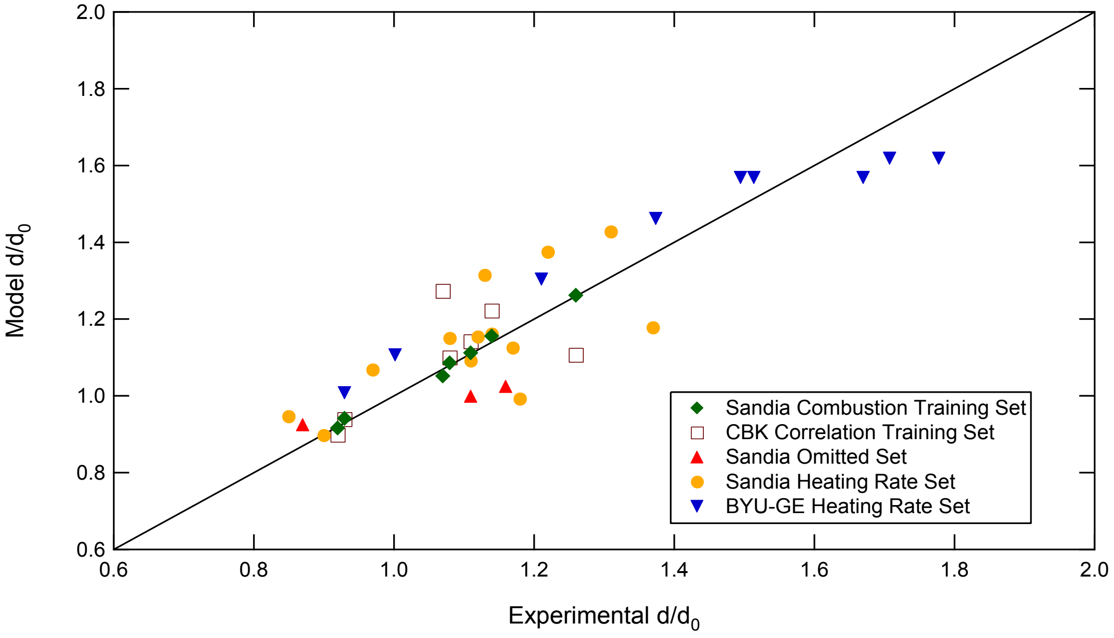

Figure 25. BYU swelling model with BYU and Sandia data. CBK swelling model shown for comparison.

Comparison of NMR and TEM/fringe3D analyses of coal soot

Table 11 shows a comparison between the results of NMR and TF3D analyses. The two tar/soot columns in the table for the TF3D analysis were from two separate high-resolution TEM photos of the same sample. In general, the TF3D analysis did not have impressive agreement with the NMR measurements. The TF3D method did not detect the aliphatic material, so the comparison of aromaticity was not a real test. Comparisons of types of aromatic carbon, such as protonated (f_a^H), non-protonated with alkyl attachment (f_a^S), or bridgehead or inner carbon (f_a^B) were not satisfactory for either the tar or the char. The most desired parameter to be able to predict accurately using TF3D analysis is the aromatic carbons per cluster (C_{cl}). However, the average number of aromatic carbons per cluster (C_{cl}) in the tar/soot was 11.2 by NMR analysis, yet predictions of 11.3 and 13.5 were made by TF3D analysis. The values of C_{cl} in the char were 18.7 (NMR) and 8.2 (TF3D), which values have drastic disagreement. This discrepancy was especially discouraging, although it may have been caused by the difficulty in getting good edge plane images for char particles in the 50 to 100 μm diameter range.

Table 11. Comparison of NMR* and TEM/Fringe3D (TF3D) analyses of tar/soot and char samples from eastern bituminous coal 'A' pyrolized at 1350 K and 1 atm after ~35 ms using a collection height of 1.275" above the burner.

Structure Parameters	**NMR^f**		**TEM/Fringe3D**		
	Tar/ Soot	Char	Tar/ Soot	Tar/ Soot	Char
Aromatic carbon, $f_a = f_a' + f_a^C$	0.91	0.92	1.0	1.0	1.0
Carbonyl and Carboxylic acid, f_a^C	0.01	0.02	0	0	0
Carbonyl, f_a^O	0	0.01	0	0	0
Carboxylic acid, f_a^{OO}	0.01	0.01	0	0	0
Aromatic carbon, carbonyl subtracted, f_a'	0.9	0.9	1.0	1.0	1.0
Protonated aromatic carbon, f_a^H	0.45	0.3	0.697	0.758	0.797
Non-protonated aromatic C, $f_a^N = f_a^P + f_a^S + f_a^B$	0.45	0.6	0.302	0.242	0.203
Aromatic carbon with O attachment, f_a^P	0.05	0.05	0	0	0
Aromatic carbon with alkyl attachment, f_a^S	0.19	0.21	0.001	0	0
Aromatic bridgehead and inner carbon, f_a^B	0.21	0.34	0.301	0.242	0.203
Aliphatic carbon, f_{al}	0.09	0.08	0	0	0
Aliphatic CH and CH$_2$, f_{al}^H	0.05	0.06	0	0	0
Aliphatic CH$_3$ and non-protonated carbon, f_{al}^*	0.04	0.02	0	0	0
Aliphatic with oxygen attachment, f_{al}^O	0.02	0.04	0	0	0
Bridgehead Carbons, χ_b	0.233	0.378			
Lattice Parameters					
Total carbons per cluster (C_{cl})	11.2	18.7	13.5	11.3	8.2
Total attachments per cluster, $\sigma+1$	3.0	5.4			
Bridges and loops per cluster, B_C	2.5	5.0			
Side chains per cluster	0.5	0.4			
Fraction of intact bridges per cluster, p	0.83	0.92			
Average cluster molecular weight	393				
Side chain molecular weight	32				

Subtask 4.5 – Slag Formation and Slag-Wall Interactions

Under this subtask the investigators developed a model for ash sintering and melting and collected validation data from a series of coal chars with varying carbon contents corresponding to various degrees of conversion. At temperatures in excess of the coal's ash fusion temperature, a significant decrease in internal surface area was observed at a conversion of roughly 92%. This is a result of the char transitioning ("collapsing") from a highly porous, solid material into a melted, much less porous slag-type material. This collapse appears to be associated with migration of mineral inclusions to the surface of the char. No such collapse was observed when the temperature of the system was below the ash fusion temperature. Previous particle sintering models divide sintering rates into several regimes depending mainly on surface curvature. A closed-form and explicit model was developed that describes particle neck size, neck radius of curvature, neck length, and essentially all other geometric properties for the idealized case of two equally sized spheres sintering without change in sphere diameter but with change in neck size and overall shrinkage.

Experimental data describing sintering for both surrogate and ash deposits indicate that ash deposits sinter unlike randomly packed particles in several important ways. Specifically, ash deposits maintain porosity longer, develop strength more slowly and to a lesser extent, and maintain anisotropic structure longer compared to random sphere structures. Random sphere experiments, which are common, can provide useful information on sintering rates and extents, but they are poor representations of deposit structures and cannot generally simulate them directly. In general, low-rank fuels sinter to a lesser extent than high-rank fuels under similar conditions. This fuel-rank dependence is much larger than any detectable dependence on local stoichiometry (gasification vs. combustion) in the limit of no melting or slag formation. The dependence agrees well with known and general properties of deposit composition and particle size between these two fuels. Thermal conductivity provides a quantifiable estimate of the degree of sintering.

Subtask 4.6 – Acquisition of Validation Data in an Entrained-Flow Gasifier

This subtask focused on extending the range of conditions for operation and characterization of the University's 1 ton/day pressurized, oxygen-blown, EFG, including detailed characterization of the slurry injector and associated atomization efficiency, and the development of a safe, flexible system to measure gas composition at various positions in the gasifier.

Subtask 4.6a – Injector design, characterization and performance

Injector design and atomization performance

Experience at the University of Utah and elsewhere shows that overall performance of an EFG is very closely tied to performance of the slurry injector. A finely atomized slurry results in better mixing between the fuel and oxygen, a more-well attached, compact flame and overall better conversion. Earlier characterization studies involved imaging of the spray produced by the injector. More recent studies focused on developing techniques to quantify spray behavior, which will allow observed injector behavior to be used for validation of spray simulations.

A patternator apparatus was used to evaluate distribution of the sprays resulting from the different micro-hole atomizers under a variety of conditions. In addition to using pure water, slurries of coal and petcoke, with different solids concentrations, were evaluated. Liquid and gas flows were varied over a range of conditions. Figure 26 shows the resulting spray distribution for an 8-microhole injector using a liquid flow rate and gas velocities typical of gasifier operation. As the solid loading increased, so did the suspension viscosity. Consequently, as the airflow increased from 0.65 kg/hr to 0.93 kg/hr, the spray became better dispersed. This behavior was more pronounced for the higher solids loadings.

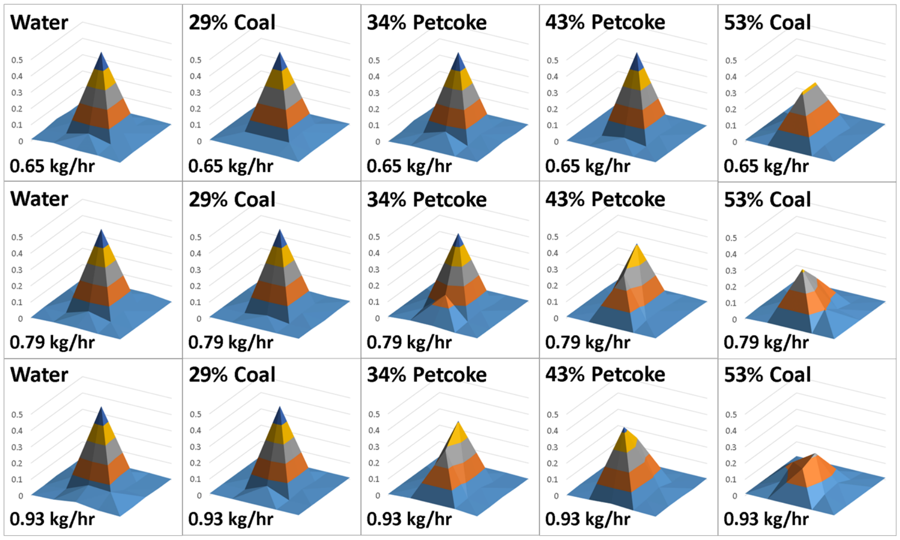

Figure 26. Patternation of various slurries at 45 liter per hour liquid flow using the 8-MH-0.023 injector. Mass flow rates of air are indicated on each plot.

Atomization can be enhanced by promoting disruption of the liquid column in the center of the injector before it experiences impingement by the high-velocity gas jets exiting the micro-holes. Industrial injectors achieve this by introducing a second gas stream in the center of the liquid column. The central gas forces the liquid into an annulus so that the gas jets break up a film rather than a column.

An 8-hole microhole injector (8-MH-0.025) was modified to function as a 3-stream injector by centering a narrow tube for central gas within the slurry tube. Testing was performed using only water. The effect of the inner tube position was evaluated on two levels, either flush with the face or recessed approximately 025 inches. Measured droplet diameter is shown in Figure 27. The x-axis indicates the inner airflow, while the different colors indicate the outer airflow. Clearly, droplet size was less for the case when the inner tube was recessed from the atomizer face. Two factors may contribute to this. First, by recessing the inner gas tube, the annular sheet is given more time to develop instabilities. These instabilities have more time to grow or are provided more amplitude by the fact that the liquid spends more time in the form of an annular sheet. Second, by recessing the inner gas tube, the gas and liquid are given space to mix before leaving the atomizer. This essentially turns the atomizer into an internal mixing atomizer with an outer, external gas annulus. These results are consistent with experience from others that both internal mixing atomizers and three-stream, annular liquid sheet atomizers to be efficient in atomizing a wide variety of liquids.

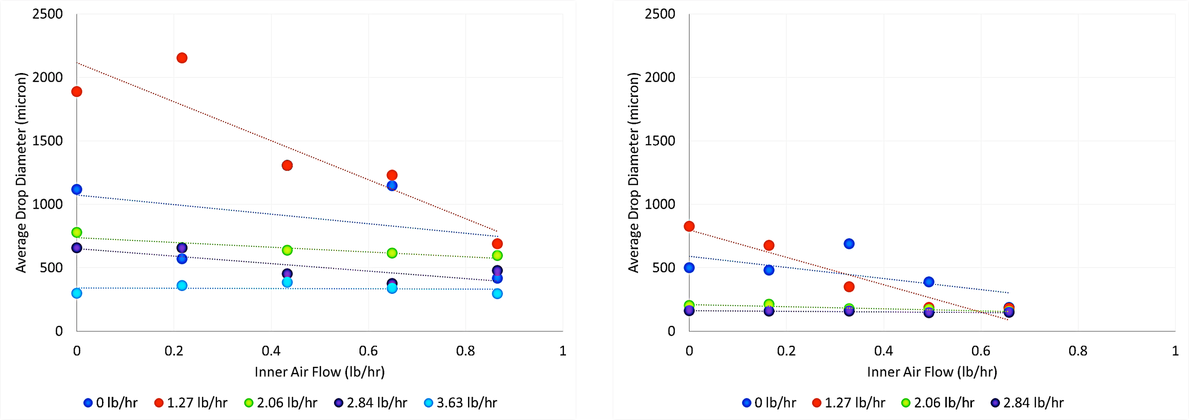

Figure 27. Effect of inner and outer airflow on the average droplet diameter with a level inner tube. The inner air flow is shown along the x-axis while the different colored curves represent the different outer air flows. The left chart shows results when the inner tube was flush with the face of the main body of the atomizer. The right chart shows results when the inner tube was recessed approximately 0.25 inches from the face.

Subtask 4.6b – Development of probe for in-situ measurements

During the most comprehensive sampling campaign, nineteen gas-phase samples from were taken from within the reaction chamber of the pilot gasifier. The probe was mounted to the third sample port down (approx. 30% of the distance through the gasifier) and samples were taken at three radial positions (near wall, centerline and midpoint between these two) during operation under three different oxygen/fuel ratios (temperatures) giving nine conditions total. Duplicate samples were taken at most conditions, and one triplicate was acquired. The dry gas phase compositions are shown in Figure 28 for carbon monoxide, hydrogen, and carbon dioxide. At higher temperatures, concentrations of CO and H_2 become less while the CO_2 concentration increases. This is expected, since higher temperatures are achieved by increasing the O_2/fuel ratio, which results in more combustion of the syngas.

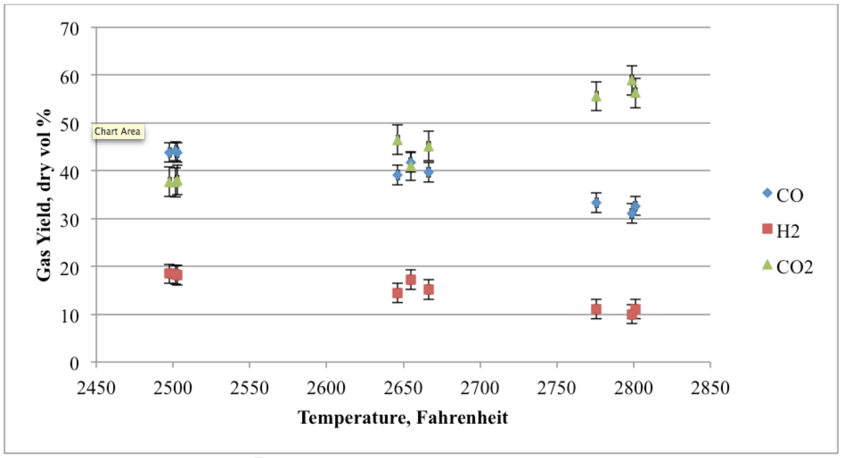

Figure 28. Measured gas compositions for carbon monoxide (◆), hydrogen (■), and carbon dioxide (▲), vol% dry. All radial locations are shown. Error bars represent standard error.

While there was a clear influence of oxygen/fuel ratio (temperature) on gas composition, the significance of radial sample location is not as apparent. This can be seen in Figure 29 for carbon monoxide, hydrogen, and carbon dioxide with varying target temperature. The dimensionless diameter coordinate corresponds to the location at which the sample was taken in the gasifier. The value indicates how far the probe has traveled in the reaction zone (e.g. 0 corresponds to the wall location and 0.5 corresponds to the centerline).

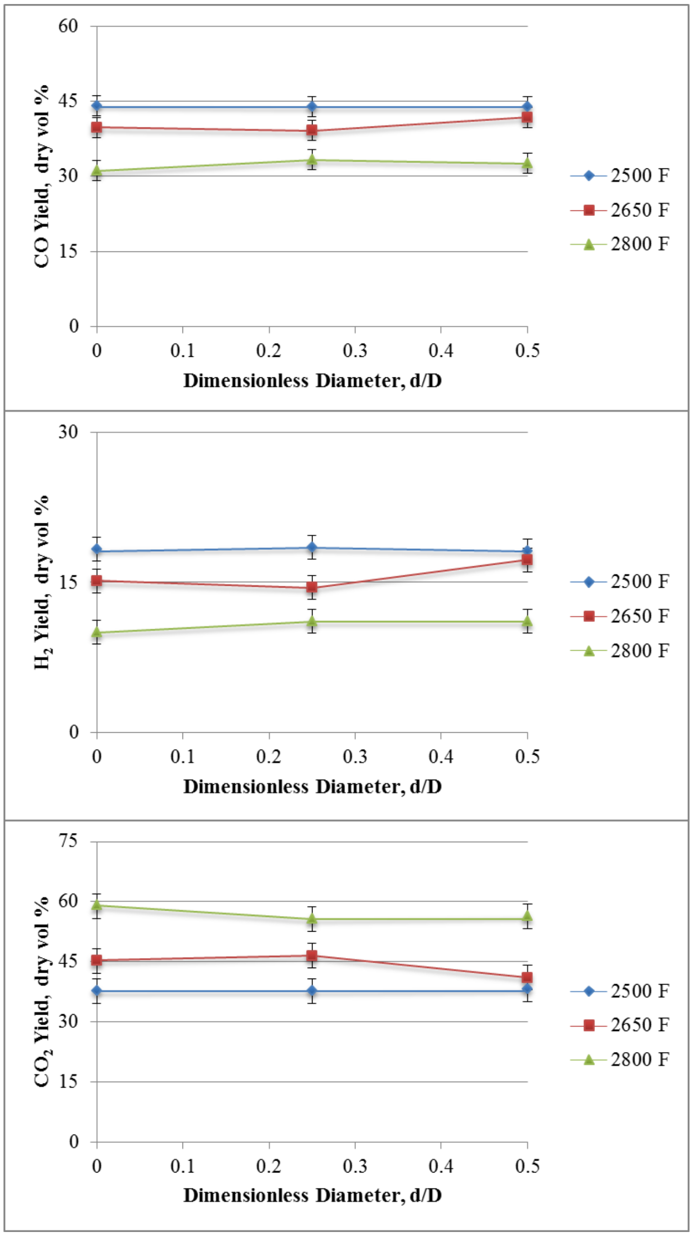

Figure 29. Radial gas compositions as a function of temperature, dry volume percent.

The heating value of the intermediate syngas was calculated from concentrations and heating values of the individual combustible components. The heating values for the intermediate (sample port 3) and final product gases differ. Centerline gas composition and gasifier outlet higher heating values (HHV) are shown in Table 12. As expected, syngas heating value decreases with temperature due to more combustion of the syngas. The syngas heating values compare reasonably well for the lower temperatures, but there was more disparity at the higher temperature. The results agree with expectations, since combustion occurs in the flame region of the gasifier, producing CO_2 and H_2O which subsequently convert the rest of the fuel through the gasification reactions $CO_2 + C \rightarrow 2\ CO$ and $H_2O + C \rightarrow H_2 + CO$.

Table 12. Heating values of intermediate and outlet syngas.

Target Temperature (°F)	2500	2650	2800
Centerline HHV (Btu/SCF)	196	187	138
Syngas Out HHV (Btu/SCF)	208	195	179

Operation of the entrained flow gasifier

The University of Utah's entrained flow gasifier was operated during several campaigns, and with many different fuels, over the course of this project. Coals tested included an eastern bituminous (Illinois #6), a PRB (North Antelope), a Utah (Sufco) and an Appalachian coal. Three different petroleum cokes were also tested. The range of conditions tested for each class of fuel is shown in Table 13.

Table 13. Range of operating conditions for solid fuel used.

Solid Fuel(s)	Temperature (°F)	Pressure (psig)	S.R. (λ)	Solid Fuel Feed Rate (lb/hr)
Coal (3+)	2250 – 3000	150 – 265	0.23 – 0.75	40 – 70
Petcoke (3+)	2400 – 2800	150 – 250	0.34 – 0.82	45 – 76

Operating a pressurized, oxygen-blown EFG at any scale is challenging, and performance is largely driven by the effectiveness and stability of the fuel injector. As this project progressed, performance of the reactor became more predictable and stable. The operating procedure, in particular the startup procedure, was refined and the operators became familiar with nuances of the reactor. Additionally, the progression of injector development allowed for more stable and predictable operation from one test to the next. Figure 30 illustrates the stable operation of the gasifier during a test with a petroleum coke over a period of approximately 3.5 hours. The figure shows stable operation at 250 psig and 2600°F for 4+ hours. The stoichiometric ratio was roughly 0.37, which is about the same as for an industrial gasifier. Aside from the initial 30-40 minutes as the reactor was brought to the target conditions, the temperature and pressure is extremely stable for the duration of the run.

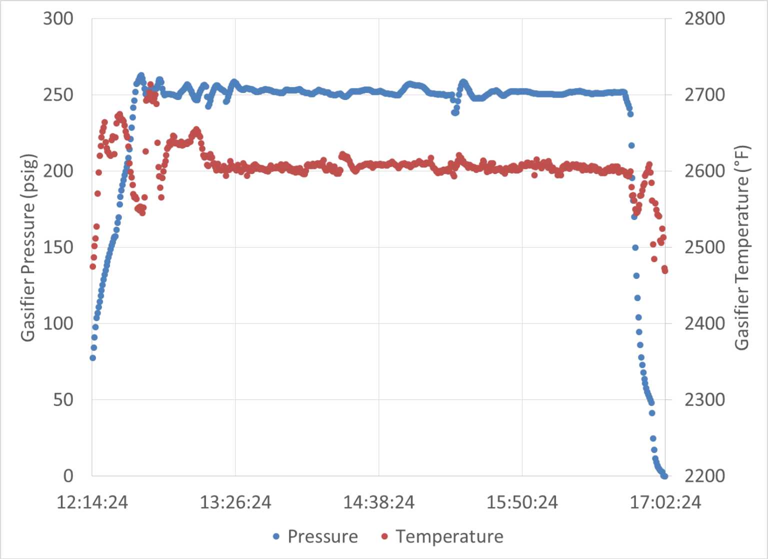

Figure 30. System temperature (maximum measured by thermocouples) and pressure during operation with petroleum coke at 2700 °F and 200 psi.

Task 5 – Chemical Looping Combustion

The following sections provide highlights of the CLC tasks. Additional detail can be found in the CLC topical reports (Sarofim et al. 2011, 2014).

Subtask 5.1 – Process Modeling and Economics

Under this subtask the investigators extracted kinetic expressions for CuO decomposition and Cu_2O oxidation from rate analyses of published literature data, which were subsequently used in the ASPEN PLUS simulations of the CLOU process. The CLOU process simulation used a fuel reactor temperature of 950°C and an air reactor is at 935°C.

They also developed an ASPEN PLUS process model for CLC using an iron-based oxygen carrier, and they considered two different temperatures. In the first scenario, the fuel reactor temperature was 950°C and the air reactor temperature was 935°C. Another scenario for the CLC process was investigated based on the design temperatures of the 1 MW_{th} pilot at Technische Universität, Darmstadt, Germany. The design temperature of the fuel reactor is 970°C and for the air reactor is 1050°C.

Relative economic comparison between CLC and CLOU

The investigators compared the capital and operating expenses for CLC and CLOU and found that:

- The cost of the reactor and the cyclone for CLC were greater than for CLOU due to the longer residence time associated with CLC reactions.
- The longer residence times in the CLC fuel reactor, due to gasification reactions, and CLC air reactor result in higher compression costs.

- CLC has a definite cost advantage in terms of the oxygen carrier (due to cost of iron versus copper based materials).
- For the 100 MW_{th} scale, two process trains for the fuel reactor in CLC and CLOU were selected. There are also two process trains for the air reactor in the CLC process but a single air reactor was for the CLOU process, which reduced the capital costs.

The comparison of relative operating costs for the CLC and CLOU processes, the total operating cost for CLC is at least twice as much as CLOU. This higher operating cost is attributed to the energy requirements associated with fluidizing oxygen carriers owing to large residence times in the CLC fuel reactor.

Subtask 5.2 – LES-DQMOM Simulation of a Pilot-Scale Fluidized Bed

This subtask compared simulation results with experimental data and explored the effects of physical parameters, superficial bed velocity and bed height, on the dynamic behavior of the bed. It also explores the effects of the particular model chosen, monodisperse, DQMOM with 3 classes, or DQMOM with 5 classes.

For all scenarios using monodisperse models, simulations captured correct orders of magnitude, but, in general, our simulations under-predict the pressure drop profiles when compared to the experimental data. There may be various reasons as to why our simulations do not replicate the experimental data. For instance, the drag models rely on calibration parameters, which are very hard to know a priori. Furthermore, these parameters change for different regimes of fluidization.

Effects of selected model

In the modeling parameter space, when we switched the model from monodisperse to DQMOM, we noticed several differences. While there was minimal difference between the monodisperse and the DQMOM model with 3 classes, there was a significant increase in pressure drop as predicted by simulation with DQMOM model with five classes. For the DQMOM model with three classes, the pressure drop in the reactor bed is under-predicted, while for DQMOM model with 5 classes, the pressure drop inside the reactor is over-predicted. This may signify a tradeoff between accuracy of the modeling approach (different drag model parameters for different phases) and number of solid stream classes. However, both DQMOM simulations are very computationally intensive, especially simulations using the DQMOM model with five classes. While these results were advanced as far as possible, there may be temporal effects, which were not resolved during the simulation time.

Previously computed simulations of the PSRI and NETL BFB serve as a good point of comparison. Our simulations perform very well in comparison to modeling work presented by NETL. They clearly capture the proper general behavior of the fluidized bed and are able to capture more of the physical behavior seen in the experiments than most of the previous models.

Effects of physical and modeling parameters

To evaluate the effects of variations in the physical parameter space (superficial bed velocity and bed height) on the pressure profile inside the reactor, several cases were run while fixing the model parameter space to the monodisperse model. The cases show that as the bed height increases, this also changes the fluidization velocity. At the same velocity of 4 m/s, the beds with larger bed heights did not yet enter the fluidization state, which translates into a chaotic pressure profile for the lower bed height and smoother pressure profile for the taller bed height. On the other hand, when a fully fluidized state is reached for the same respective bed height, increasing the velocity has little or no effect on the pressure drop profiles.

Computational costs

Computational effort required for each simulation case varied. Because of the simplicity of the model, simulations using the monodisperse model were the most computationally efficient. Computational efforts required for simulations using the monodisperse model were minimal in comparison to computational efforts required for simulations using the DQMOM model with three classes, and especially for simulations using the DQMOM model with five classes. The DQMOM model with five classes was the most computationally intensive, with computational costs three orders of magnitude greater than computational costs required for simulations using the monodisperse model for the same case. Simulations using the DQMOM model with 5 classes were run on anywhere between 480 and 600 computing cores, with computational times on the order of days to capture just 1 second of physical time.

Subtask 5.3 – Laboratory-Scale CLC Studies

This subtask focused on acquiring data in the laboratory that would useful for scale-up of CLC technology, in particular copper-based CLOU. This was achieved through four studies:

- Measurement and modeling of O_2 release rates by reduction of CuO in the fuel reactor
- Measurement and modeling of Cu_2O oxidation in the air reactor
- Evaluation of coal conversion by copper-based CLOU
- Evaluation of attrition rates for various copper-based carriers

Measurement and modeling of O_2 release by reduction of CuO

Several series of experiments were performed using the TGA, in which the oxygen partial pressure and sample temperature can be precisely controlled. The resulting range, from 58 to 67 kJ/mol, is considered the intrinsic activation energy of CuO decomposition.

The order for cupric oxide, α, was determined by analyzing the shape of the mass loss curve. The reaction may be determined graphically to be either zero, first or second order in CuO by integrating the rate expressions and plotting the term for concentration of CuO of the integrated rate expression versus time and identifying if any yield a straight line. Performing this analysis, the reaction order in CuO concentration appears to be approximately zero.

In industrial-scale fuel reactors where the bed material may be several feet deep, oxygen released from the particles may create an appreciable oxygen partial pressure either locally or in regions of little fuel. This in turn will reduce the driving force for decomposition, which may slow the decomposition rate. Tests were designed to isolate the influence the oxygen driving force has on the decomposition reaction and to determine the reaction order with respect to oxygen partial pressure, β. The reaction appears to be first order in ($P_{O2,eq} - P_{O2}$).

Finally, the investigators developed an overall expression for rate solely as a function of temperature and surrounding O_2 partial pressure:

$$rate\left(\frac{g}{s}\frac{1}{g_{Cu}}\right) = 3.90\times10^{-4}\exp\left(-\frac{62000}{\mathrm{R}\times\mathrm{T}}\right)\left[6.057\times10^{-11}exp^{0.02146\times(T-273)} - p_{O_2}\right]$$

This expression represents the final product of this study. Figure 31 compares the model presented above with rates obtained from experimental data from the titania- and zirconia-supported oxygen carriers tested over the temperature range 800 to 950°C. It also compares models derived using the two different activation energies. The model clearly does a good job predicting the rate of decomposition, and is considered suitable for modeling and scaling the fuel reactor of a copper-based CLOU system.

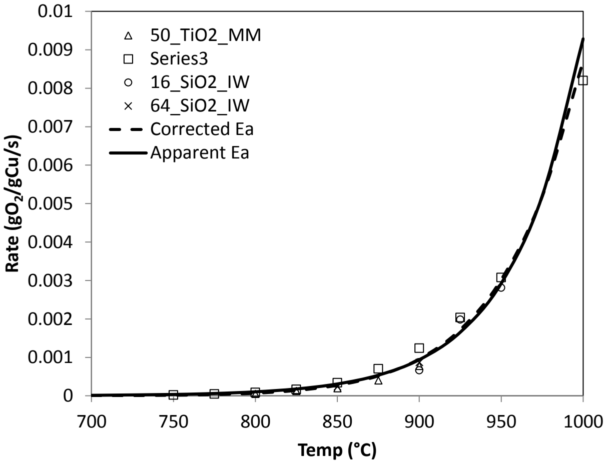

Figure 31. Reaction rate versus temperature for 4 different CuO-based oxygen carriers in TGA at four different temperatures along with the rates predicted by the rate expression determined in this study.

Modeling the oxidation of Cu_2O to CuO ($Cu_2O + ½\, O_2 \rightarrow 2\,CuO$) is challenging when trying to take into consideration all factors that influence the rate. As with the case of CuO decomposition described above, the dual influences of changing intrinsic kinetics and oxygen partial pressure driving force with temperature make experimentation and associated analysis challenging. The same type of approach of varying oxygen partial pressure simultaneously with temperature to maintain oxygen driving force was used for this component of the subtask.

Conversion of solid fuels with CLOU carriers

In order to gauge performance of the studied CLOU carriers for converting solid fuels in a fluidized bed, tests were performed in which small batches of fuel were added while the bed was fluidized with nitrogen, allowing oxygen uncoupling. Three different fuels (Illinois #6 coal, Black Thunder coal from the Powder River Basin (PRB), and petroleum coke) were used for this study and were converted in the fluidized bed using two different oxygen carriers (50_TiO2_MM and 45_ZrO2_FG). The reactivity of the tested fuels, from low to high, is petcoke < Illinois #6 < Black Thunder PRB. Not surprisingly, the PRB coal reacts very quickly reaching full conversion in just a few seconds. The Illinois #6 coal and petcoke, however, do not reach full conversion. From a stoichiometric standpoint, the oxygen supplied by the metal oxide carrier should be more than sufficient to fully combust all of the fuels. Additional tests revealed that the fuel is not being ejected from the reactor, but is simply not completely reacted within the fluidized bed. The full reaction profile obtained during the combustion of Illinois #6 coal is very similar to the petcoke, in that, it is not fully combusted until the air is once again cycled through the reactor.

Evaluation of attrition rates for various copper-based carriers

Attrition rates of four different CuO-based oxygen carriers were measured in the lab-scale fluidized bed system. The four carriers were the 50_TiO2_MM, 45_ZrO2_FG, 50_SiO2_IW and 70_SiO2_IW. The 50_TiO2_MM material clearly showed much worse loss due to attrition than the other three carriers. This is particularly apparent during the first two hours of testing. In addition, attrition rates decrease over time, even for the three carrier materials that had previously undergone several oxidation/reduction cycles in the fluidized bed. Considering just the final hours of testing, the 50_TiO2_MM lost an average of 0.0032% of the bed mass per hour over the range of conditions studied. The best performing material, the 45_ZrO2/MgO_FG lost just 0.0008% per hour during the final hours of testing.

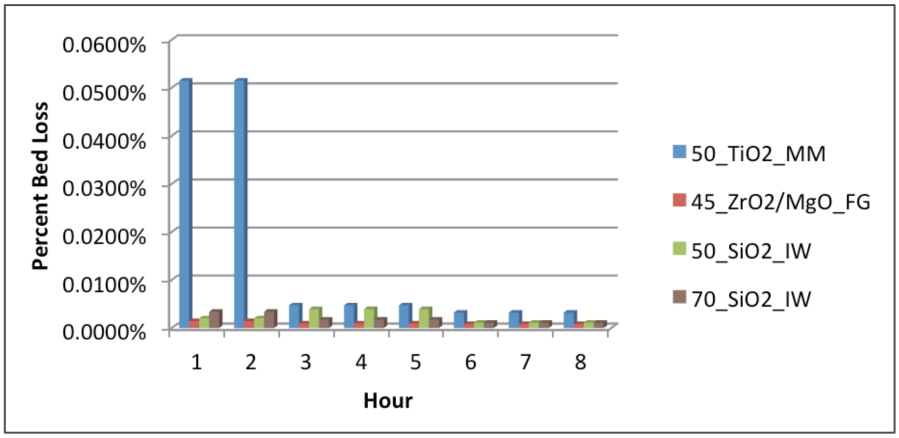

Figure 32. Measured mass loss per hour as a result of carrier attrition for the four carriers tested.

Subtask 5.4 – CLC Kinetics

TGA studies

First the experiments were carried out using the TA Q500 TGA in the 850 – 950 °C temperature range under isothermal conditions. The rates were evaluated assuming first-order kinetics, and the first-order model was found to be a reasonable fit. The 327 kJ/mol activation energy for the reduction was determined with the Arrhenius equation. This value is in good agreement with literature values. Their oxidation rate results obtained at temperatures below 550 °C indicating faster reaction at increased temperatures are clearly different from the observations at the high temperatures.

A further complication was identified by comparing the results obtained with the TA Q500 and TA Q600 instruments. The rate constants were found to be different depending on the TGA used to measure them. By considering the difference of between the sample holder pans of the TA Q500 and the cups used in the TA Q600, and normalizing the rate constants with the exposed surface area of the sample holder, the two sets of the experimental data were both brought into reasonable agreement as seen in Figure 33.

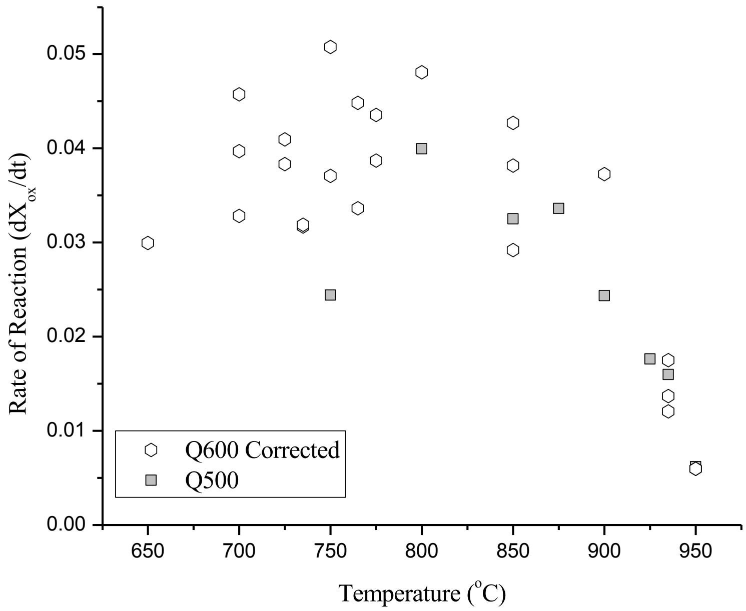

Figure 33. The combined set of rate constants.

Development of supported oxygen carriers

Copper-based oxygen carrier materials supported on alumina, titania, zirconia, silicon carbide, sand, and celite were investigated. The evaluation revealed that new material with a higher surface area and the mechanical strength necessary to resist agglomeration and attrition in fluidized-bed environments was needed. The investigators evaluated several methods for impregnating copper on the silicon carbide support and identified a coat then bake method that provided good copper loading and integrity. They were able to develop materials with 16 and 42% CuO loading for testing in fluidized-bed experiments, which showed no signs of agglomeration up to 1000°C. The 62% CuO sample showed signs of agglomeration at 900°C and was rejected.

Task 6 – Underground Coal Thermal Treatment

The following sections provide highlights of the UCTT subtasks. Additional detail can be found in the UCTT topical report (Smith et al. 2015).

Experimental Studies

Scoping studies

The scoping studies revealed that higher final temperatures provided more gas and water, as well as a higher conversion rate from coal to char. However, there is no clear difference between 500°C and 600°C, which can give an indication of the best conditions for return on investment. For the effect of pressure and heating rate, no clear conclusions can be derived based on the conditions studied and data obtained.

The gas-phase products included CH_4, CO, H_2 and CO_2. The liquid products contained more than 50% paraffins. Increasing the final temperature increased the percentage of aromatics, but the aliphatic content remained high. Increasing the pressure appears to increase the generation of lower molecular weight products, which is not unexpected.

RBR studies

Figure 34 shows typical gas-phase concentrations and the coal internal temperature profile. Note that the coal internal temperature used is located in the center of the middle coal chunk. The most abundant gas-phase products are methane and CO_2, followed by CO, ethane, ethylene, and hydrogen. Measured gas products included H_2, CO, CH_4, C_2H_4, C_2H_6, and CO_2. The results in Figure 34 are typical of the runs at ambient pressure and at temperatures above 500 C.

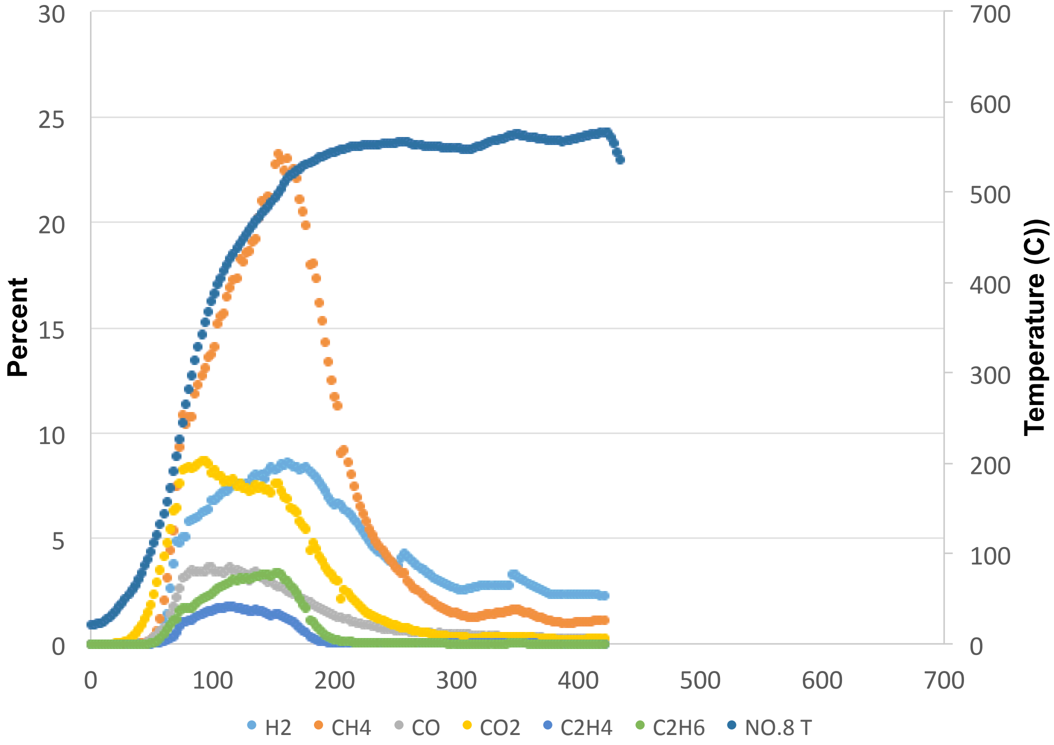

Figure 34. Temperature and gas-phase concentrations for run #8, heater setpoint at 800 C, ambient pressure, and a coal internal steady-state temperature of approximately 550°C (run #8). The percent on the y axis is volume percent.

Like the scoping studies, the RBR studies showed that yield increases with temperature, as expected, and that the yields for the scoping and the RBR studies agreed reasonably well. The effect of pressure on yield is less clear from the results. At temperatures of 500°C or greater, yields ranged from 20 – 28% (excluding water) on a dry basis.

The liquid products included C7 and heavier compounds. The simulated distillation results from the liquid product sample showed that the UCTT product is light-crude like but slightly less saturated with hydrogen than conventional crude. There are some products between C3 and C7, which are not captured by this system, but a brief study found these to be insignificant.

Figure 35 shows the mass balance for a RBR run and how the species partition between char, tar, gas-phase products, and water. Note that this balance uses the average coal composition (Table 4), elemental analysis of the liquid and gas-phase samples from RBR Run #3, and the char composition for all similar RBR runs. Approximately six percent of the hydrogen and twenty percent of the oxygen are from the original moisture in the coal (mole %). Approximately 3% of the carbon and 6% of the hydrogen are not accounted for in the balance. Because nitrogen was not measured in the liquid product, the investigators assumed that any remaining nitrogen partitions to the tar. Both the oxygen and the sulfur balances slightly over-account for these species. This result is likely due to the inhomogeneity of the coal. This figure shows that carbon tends to partition to the char, while hydrogen tends to partition to the gas and tar products. Oxygen tends to be found in the water and gas products, while sulfur tends to partition to the char and tar products.

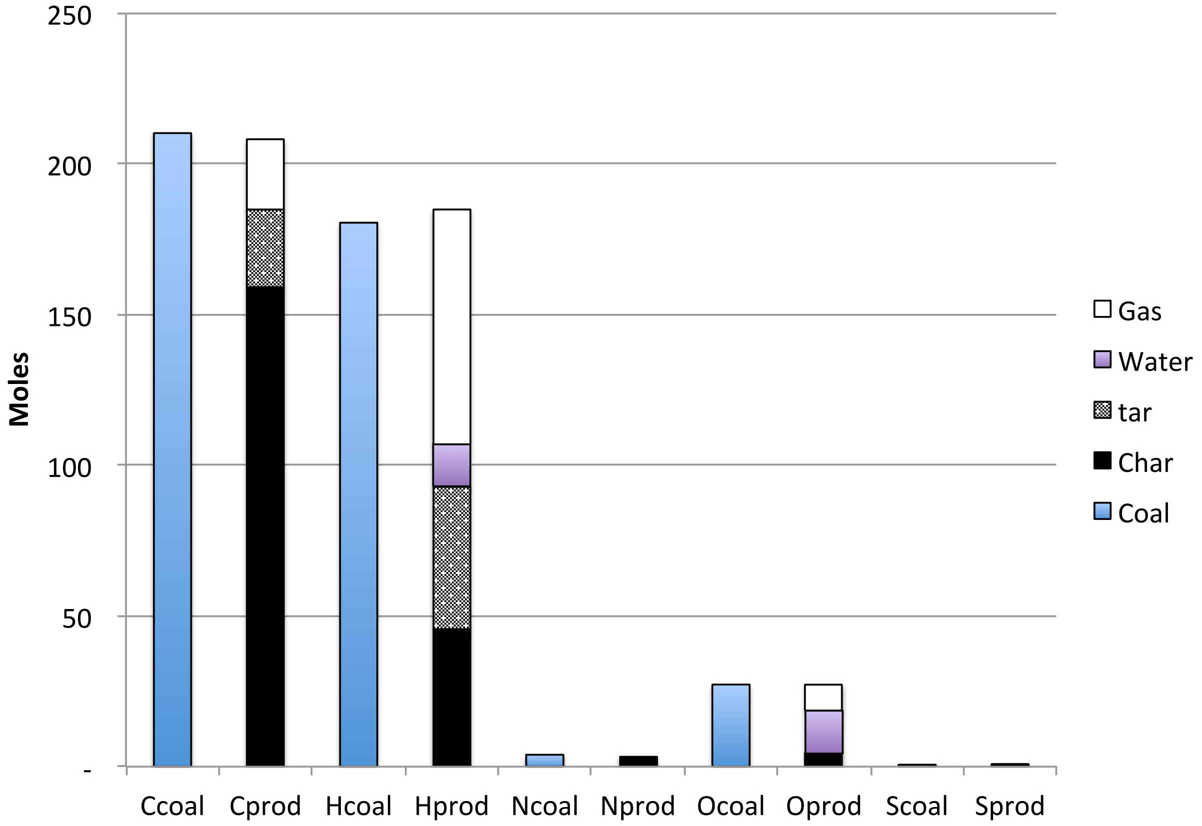

Figure 35. Moles of carbon (C), hydrogen (H), nitrogen (N), oxygen (O), and sulfur (S) in the original coal (as received) and in the char, tar, and gas.

Simulation Studies

The investigators ran five simulations comparing the various yield models as well as seam thicknesses and heater temperatures. An example temperature distribution after 1,800 days of heating is shown in

Figure 36. These simulations showed that differences in the yield model and heater temperatures can have a significant impact on the overall NER of the process.

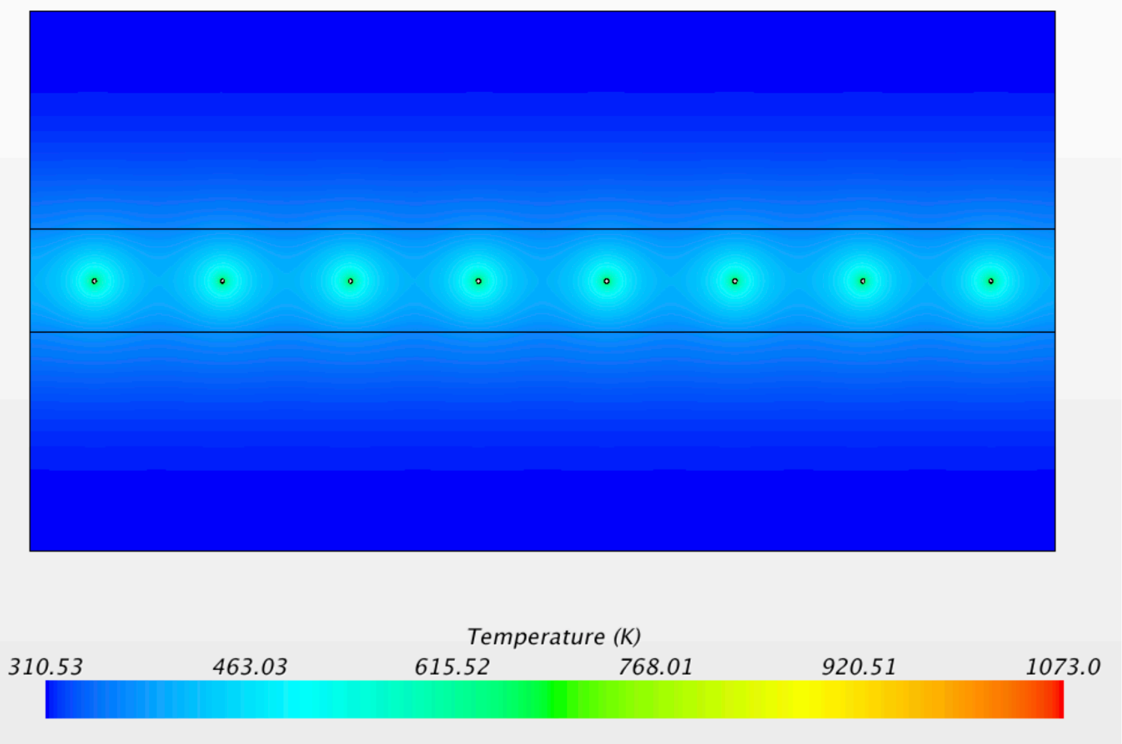

Figure 36. Front view of temperature distribution for Yield 3 model with lower heater temperature of 675 K after 1,800 days of heating.

The mass of product plays a significant role in determining the overall NER for the process. These studies assumed that 1 kg of product mixture has energy equivalent of 30.4 MJ. Using this conversion and by tracking the amount of heat provided by the heaters, we can calculate the equivalent energy out versus the energy requirement in to determine the overall NER for the process. As expected, the NER for the optimistic yield model shows the greatest net energy return, while the least optimistic yield model coupled with the lower heater temperature of 675 K shows the lowest NER.

Another noticeable trend is that for all simulations the NER decreases after about 400 days of heating. The NER continues to further decrease the longer the formation is heated. This declining trend in NER can be attributed to the increasing heat losses from the heater to the overburden and underburden as the heating continues.

CO_2 Storage Studies

Pyrolysis mass losses

Coals from the Carlinville mine in Utah, the Carlinville mine in Illinois, and the North Antelope mine in Wyoming were pyrolized in a tube furnace in an anoxic environment. The coals were heated to final temperatures of 325, 450, or 600°C with heating rates of 10 or 0.1°C per minute. As part of the pyrolysis procedure, masses of the coals were recorded before and after each experiment.

Pore size distributions

Pore size distributions were performed using a combination of two different methods, density functional theory to characterize micropores (<20Å) and Barrett-Joyner-Halenda (BJH) was used for pores larger than 20Å. Sohxlet extraction with acetone was employed to determine the effects of residual tars on the pores.

Sufco coal

Pore volumes increased with treatment temperature after 325°C. Like the surface area for the coals treated to 325°C being less than that of the fresh coal, there is a slight reduction in pore volumes from that of the unreacted coal over the entire range of pores measured. This reduction in pore volumes occurred regardless of heating rate. Coals treated to 450°C showed an increase in the mesopore ranges for both heating rates with a larger increase in mesopores. Coals treated to 450°C with a heating rate of 0.1°C/min showed little increase in micropores while the coal treated to the same temperature with a heating rate of 10°C/min showed a noticeable increase. Both coals treated to 600°C showed large increases over the entire range of measured pore sizes. The coal treated to 600°C with a heating rate of 10°C/min showed larger increases in the micro- and mesopore regions than the coal heated with a rate of 0.1°C/min.

Carlinville coal

The pore size distributions on the Carlinville coals showed some major differences when compared to the Sufco coal. While the Sufco coal showed large increases in the range greater than 20Å, the Carlinville coal showed more changes in the micropore region. The shift between the largest pore abundances between these two coals is not great and is likely the result of differences in the original coal matrix structure. With the unreacted Carlinville coal, the largest amount of pore volume occurs around 20Å with solvent extraction showing increases in both the micro- and mesopore regions. Like the Sufco coal, pore volumes tend to increase with treatment temperature. The Carlinville coal treated to 325°C with a heating rate of 0.1°C/minute had pore size distributions almost identical to the untreated coal even after solvent extraction implying that little physical change occurred in the coal structure. Carlinville coal treated to 325°C with a heating rate of 10°C/minute showed an increase in the high micropore/ low mesopore region with solvent extraction showing only slight differences. The coal treated to 450°C with a heating rate of 10°C/minute showed a shift into the mesopore region with the largest increase around 20Å. The increase in this coal remained after solvent extraction but shifted into the micropore region. The coal treated to 450°C with the slow heating rate had a large increase over the entire range of pore sizes after solvent extraction. Both coals treated to 600°C showed a significant increase across the entire pore distribution with solvent extraction increasing those pore volumes.

North Antelope coal

The North Antelope coal pore size distributions shared a similar trend with the Carlinville and Sufco coals in that the pore volumes increased with the extent of thermal treatment and that the coals treated to a final temperature of 325°C showed similar or lesser pore volumes than the unreacted coal. This trend seems to be universal across all the coals and shows that at low pyrolysis temperatures pore changes are largely dominated by plastic deformation. When the unreacted coal was treated with acetone extraction, a large increase in the micropore region was observed implying that pre-existing hydrocarbons were blocking these pores. Solvent-treated coals heated to 325°C showed increases in the micro- and mesopore regions, but both were still less than the solvent extracted untreated coal. This lends credibility to the hypothesis of small pores swelling shut at lower treatment temperatures. The North Antelope coal treated to 450°C with the fast heating rate showed a net increase over that of the unreacted coal and coals treated to 325°C and solvent extraction caused little change in pore volumes.

Adsorption isotherms

Isotherm measurements were performed at temperatures of 50 or 70°C with CH_4 or CO_2. Results of the isotherm measurements were fitted to the Langmuir equation. In this study, the results of 84 individual isotherms were presented with each individual isotherm requiring about one week to process.

Sufco coal

Like the surface area measurements and pore size distributions, the high-pressure isotherm measurements on the Sufco coal showed trends dependent on the treatment temperature but not so much with heating rate. For each of the coals used in this study, there are eight unique plots. Each plot shows the three coal samples treated at a given heating rate plus the untreated coal for comparison. The results of the adsorption isotherm measurements for the fresh and thermally treated Sufco coal (heat rate of 0.1°C/minute) can be found in Figure 37.

High-pressure isotherms for the thermally treated coals showed similar trends to those observed with the pore size distributions and surface area measurements. Isotherms on coals treated to 325°C showed less adsorptive capacity than the fresh coals, and the capacity of the coals increased with treatment temperature. The adsorptive capacity of the coals increased with treatment temperature. The effect of heating rate on adsorptive capacity is less pronounced than the effect of pore size distributions. As expected, the adsorptive capacity for CO_2 exceeded that of CH_4, and the volume adsorbed decreased with measurement temperature.

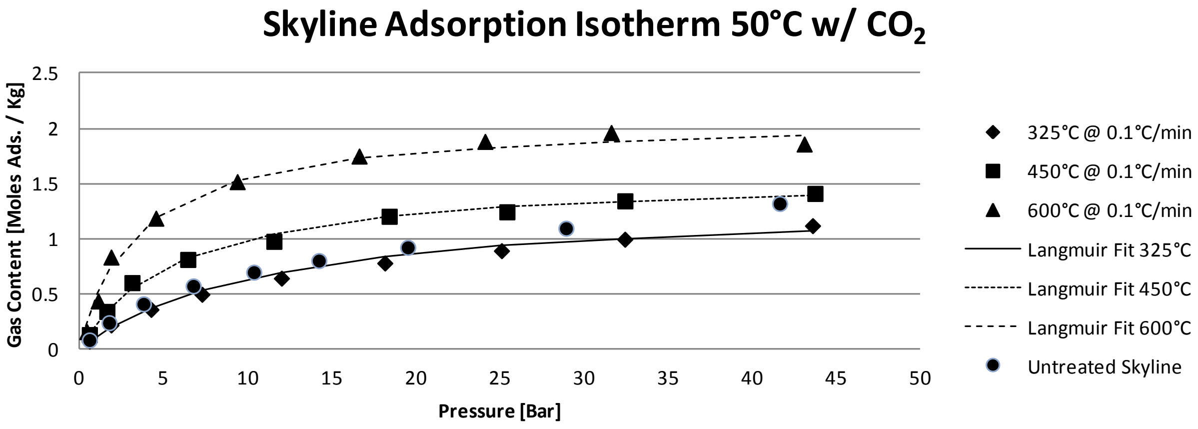
Skyline Adsorption Isotherm 50°C w/ CO_2
Gas Content [Moles Ads. / Kg]
0
0.5
1
1.5
2
2.5
Pressure [Bar]
0
5
10
15
20
25
30
35
40
45
50
◆ 325°C @ 0.1°C/min
■ 450°C @ 0.1°C/min
▲ 600°C @ 0.1°C/min
Langmuir Fit 325°C
Langmuir Fit 450°C
Langmuir Fit 600°C
● Untreated Skyline

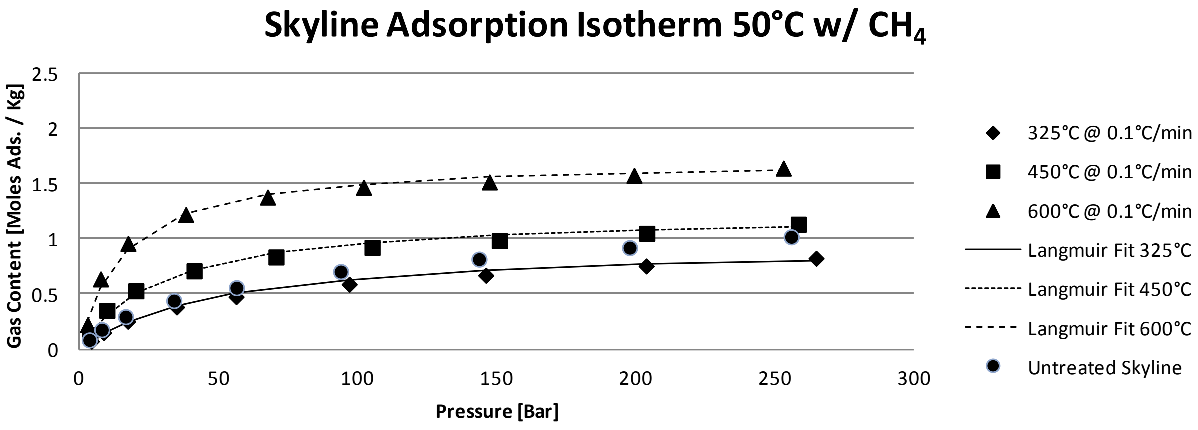
Skyline Adsorption Isotherm 50°C w/ CH_4
Gas Content [Moles Ads. / Kg]
0
0.5
1
1.5
2
2.5
Pressure [Bar]
0
50
100
150
200
250
300
◆ 325°C @ 0.1°C/min
■ 450°C @ 0.1°C/min
▲ 600°C @ 0.1°C/min
Langmuir Fit 325°C
Langmuir Fit 450°C
Langmuir Fit 600°C
● Untreated Skyline

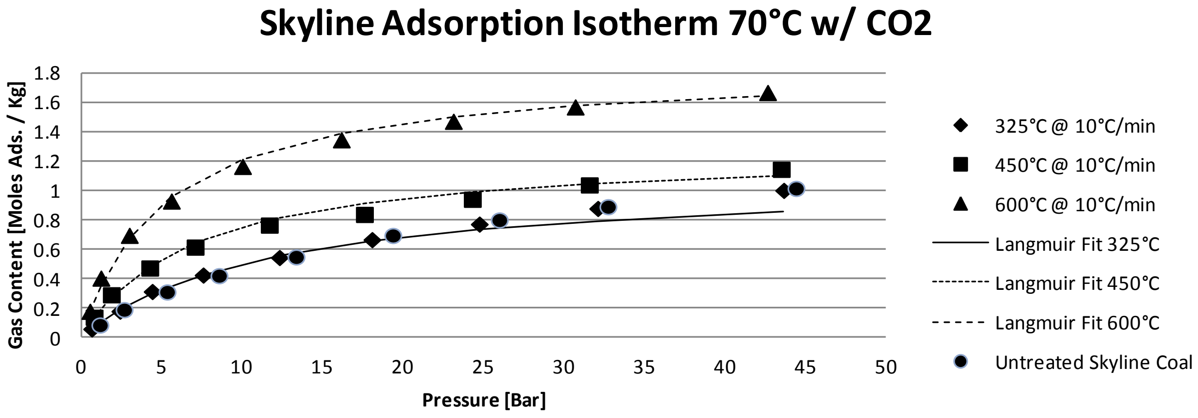
Skyline Adsorption Isotherm 70°C w/ CO2
Gas Content [Moles Ads. / Kg]
0
0.2
0.4
0.6
0.8
1
1.2
1.4
1.6
1.8
Pressure [Bar]
0
5
10
15
20
25
30
35
40
45
50
◆ 325°C @ 10°C/min
■ 450°C @ 10°C/min
▲ 600°C @ 10°C/min
Langmuir Fit 325°C
Langmuir Fit 450°C
Langmuir Fit 600°C
● Untreated Skyline Coal

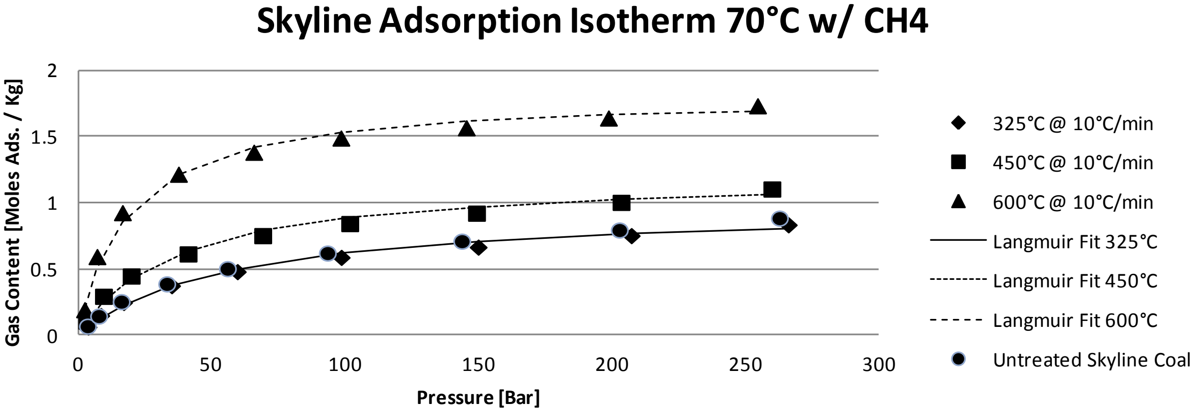

Figure 37. Example of high-pressure adsorption isotherms for thermally treated Sufco coal treated with a heating rate of 0.1°C/minute. The figures say Sufco coal, but it was later confirmed to be Sufco coal. Adsorption values reported in moles of adsorptive per kilogram of coal (dry basis).

Adsorption values were fitted to the Langmuir adsorption equation which provides theoretical maximum adsorptive capacities and curvature of the isotherm. The Langmuir equation defines the adsorbed phase as a single layer; with coals this is not the case. The Langmuir equation, however, does fit the adsorption data with a good degree of agreement and is commonly used to model adsorption on coals. The R^2 value from the linear regression fitting data to the Langmuir equation was at least 0.97 and very commonly 0.99 or better. An example of Langmuir fitting parameters for treated coals can be found in Table 14.

Table 14. Langmuir fitting parameters for coals treated with a 0.1°C/minute heating rate. V∞ is in moles adsorbed per kilogram, β is in 1/bar.

Coal	*Langmuir Fit*	*CH_4 @ 50°C*	*CH_4 @ 70°C*	*CO_2 @ 50°C*	*CO_2 @ 70°C*
Skyline	V∞	1.174	0.885	1.590	1.213
	β	1.972E-02	2.425E-02	8.600E-02	6.490E-02
325@10	V∞	1.034	1.072	1.267	1.742
	β	2.473E-02	1.341E-02	8.938E-02	3.561E-02
450@10	V∞	1.404	1.393	1.666	1.742
	β	4.884E-02	2.952E-02	1.237E-01	8.366E-02
600@10	V∞	1.957	1.742	1.947	1.990
	β	6.289E-02	4.434E-02	1.392E-01	9.679E-02

Carlinville coal

The isotherms measured on the Carlinville coals showed trends very similar to those shown by the Sufco coals. The measured values of the adsorbed gas on the Carlinville coals were similar in magnitude to the Sufco coals. Like the Sufco coals, the Carlinville coals treated to 325°C showed capacities rarely greater than unreacted coal. Also like the Sufco coal, the Carlinville coals showed increases in capacity with the extent of thermal treatment temperature. And as expected, the capacity for CO_2 exceeded that of methane, and adsorptive capacity decreased with measurement temperature.

North Antelope coal

Isotherms on the unreacted and thermally treated North Antelope coals showed trends identical to those of the Sufco and Carlinville coals. Coals treated to 325°C showed reduced capacity compared to the unreacted coal, and adsorptive capacity increased with final treatment temperature. Also, like the previous coals, the North Antelope coal showed little difference in capacity with either heating rate.

Task 7 – Mercury

This subtask focused on understanding the effects of oxy-firing on gas-phase mercury oxidation by chlorine and bromine and the effects of SO_2 in an oxy-firing environment. Additional detail can be found in the mercury topical report (Buitrago et al. 2010).

In the absence of SO_2, the oxy-firing environment caused a remarkable increase in oxidation of mercury by chlorine. At 400 ppm chlorine (as HCl equivalent), air-firing results in roughly 5 percent oxidation. At the same conditions as oxy-firing, oxidation levels are roughly 80 percent. Figure 38 shows gas-phase oxidation levels with oxy-firing of 70 to 80 % at 100 and 400 ppm chlorine (as HCl equivalent). Oxidation levels with bromine at 25 and 50 ppm (as HBr equivalent) ranged from 80 to 95 percent and were roughly the same for oxy- and air-firing conditions.

Kinetic calculations of levels of oxidation at air- and oxy-conditions captured the essential features of the experimental results but have not revealed a mechanistic basis for the oxidative benefits of oxy-firing conditions.

At all conditions, the effects of quench rate were not significant.

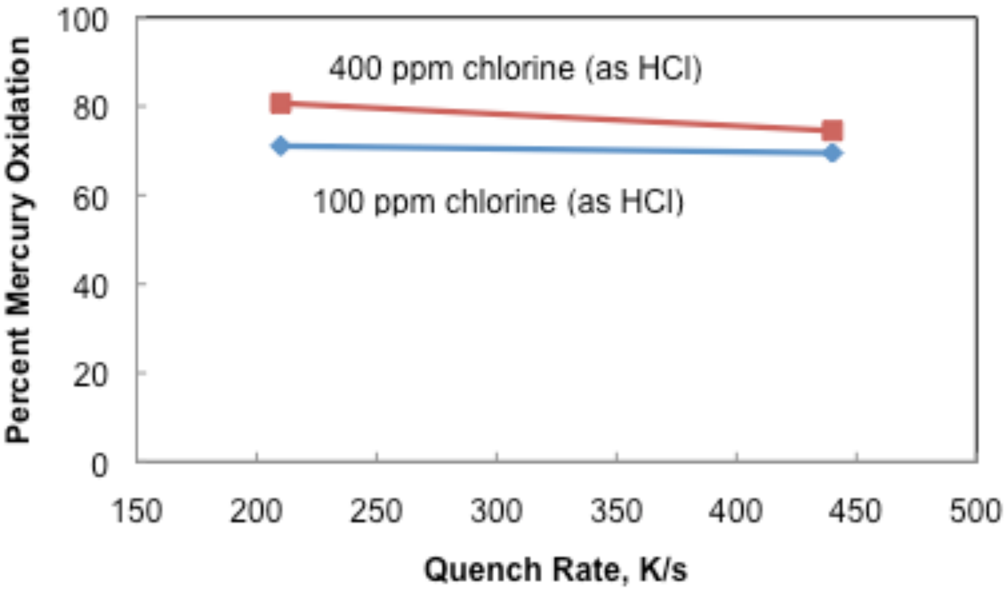

Figure 38. Extents of oxidation with oxy-firing, chlorine, and no SO_2.

The presence of 500 ppm SO_2 caused a dramatic decline in the levels of oxidation at all oxy-fired conditions examined. This effect suggests that SO_2 may be preventing oxidation in the gas phase or preventing oxidation in the wet-conditioning system that was used to quantify elemental and oxidized mercury concentrations. Similar effects of SO_2 have been noted with air-firing. The addition of sodium thiosulfate to the hydroxide impingers that are part of wet-conditioning systems may prevent liquid-phase oxidation from occurring.

Task 8.0 – Strategies for Coal Utilization in the National Energy Portfolio

The following sections provide highlights of the policy subtasks. Additional detail can be found in Davies et al. (2012, 2013, 2014), Reitze (2011a, 2011b) and Reitze and Durrant (2011a, 2011b, 2011c).

8.1 – Existing Regulatory Framework and Emerging Policy Issues

Federal regulations

EPA regulates underground carbon injection through the Safe Drinking Water Act. Recently finalized regulations require permits for underground carbon injection, project monitoring and reporting, and proof of fiscal responsibility. Parts of the CAA will also impact CCS, including sequestration as a trigger for Prevention of Significant Deterioration or New Source Review requirements, the possibility that CCS or other clean coal technologies might be required as the Best Available Technology, and the potential for sequestration facilities to be subject to other regulations applicable to stationary sources. At the time of this work, EPA had not yet proposed their NSPS for new and existing coal-fired power plants. The

National Environmental Policy Act (NEPA) the Endangered Species Act, and other applicable federal pollution, planning, and leasing laws may also apply to carbon capture and sequestration.

The subtask also examined recent federal legislative proposals that would impact CCS. Cap-and-trade legislation introduced in 2009 would have placed a price on carbon emissions, which would have made CCS a more economically feasible option. However, proposed bills in the House and the Senate were not enacted.

Further discussion of federal regulation of CCS can be found in Reitze (2011a, 2011b).

State regulations

In the absence of comprehensive federal legislation regulating CO_2, regional and state actions are becoming increasingly important voices in the policy discussion of how best to implement effective control of CO_2. Regional bodies and state governments are responding to concerns about climate change and energy sustainability by enacting laws, regulations, and economic incentives to promote differing energy strategies that will impact CCS efforts. This subtask considered how several regional bodies and eighteen western states have approached CO_2 regulation—including the various capture, transport, and storage aspects of CCS. The Interstate Oil and Gas Compact Commission is a regional body that represents the oil and gas interests of its thirty-eight member states and nine international affiliates. It has produced a comprehensive model legal and regulatory framework for geologic storage of CO_2 that advocates state and provincial level regulation of stored CO_2. Other efforts to control GHG emissions and influence federal policy were led by three different regional programs. Although each program emphasized different goals and used different paths to regulate and enforce its policies, these regional bodies offer insights into the impacts of varying levels of cooperation, investment, and direction on both climate change issues and CCS deployment strategies. Since 2005, cap-and-trade programs have been the main approach favored by these regional programs. The Regional Greenhouse Gas Initiative is the oldest of the three and has held auctions of CO_2 allowances for electric power generators since 2005. The Midwest Regional Greenhouse Gas Reduction Accord takes a very favorable view of CCS and has finalized recommendations for a cap- and-trade program, but the member states have yet to ratify the recommendations. The Western Climate Initiative also has developed model rules and supporting regulations. Two member states, California and New Mexico, have passed legislation to begin the cap-and-trade program in 2012, but New Mexico's program may not continue because of the opposition. There is speculation that because federal legislation has stalled, the three regional programs may combine forces in an effort to pressure and incentivize other states to adopt climate change strategies. However the political changes that have curtailed federal action may also hinder future state efforts.

Individual states are also enacting legislation and regulatory processes for CCS. The review of western states' initiatives shows that even states with such different stances on climate change and government regulation as California and Texas have indicated governmental support for CCS and enacted extensive and often similar legislation to regulate it. Funding has increased dramatically over the past decade, and although CCS still faces substantial technological and financial hurdles, efforts have been made in several states to address some of the political and legal hurdles. Adoption of a GHG cap-and-trade program by either states or regional bodies would make carbon emissions a significant cost item for electricity generators. This in turn would make CCS more attractive and economically practical for sources under such a program. While the fate of national and global actions to combat climate change are uncertain, much time, money, and planning has been invested by several states and regional bodies to define, regulate, and promote CCS.

Further discussion of state regulation of CCS can be found in Reitze and Durrant (2011b,c).

8.2 – Barriers to and Regulatory Promotion of Emergent CCS Technology

The survey results identified several important lessons about barriers to CCS commercialization, and what regulatory measures might address these barriers. The eight primary points are:

- There are four primary, interrelated barriers to CCS commercialization: cost; lack of a price signal or other financial incentive for CCS use; liability; and lack of comprehensive CCS regulation.
- Of these, cost and cost-recovery are the greatest obstacles. Survey participants ranked these obstacles as the "most significant" to CCS commercialization, and cost received the overwhelming number of responses to the open-ended questions.
- Although insufficient technology is often cited as a barrier to CCS, this seems not to be the case. Survey participants expressed relative confidence in CCS technology compared to other possible CCS barriers, and the more often respondents work with the technology, the more confidence they are likely to have in it.
- Incentives for CCS commercialization are strongly favored by the CCS community. The four most favored are economic and regulatory: tax/financial incentives; liability limits; a comprehensive CCS regulatory framework; and a carbon tax. There is, however, little consensus regarding which incentive is best. Virtually every sector of the CCS community has a different preferred path forward. A combined approach may be necessary.
- The CCS community wants clear, comprehensive regulation of its processes. The most desired regulation is liability limits, followed by a general preference for comprehensive CCS regulation.
- The preferred form of liability protection is for the government to take legal custody of sequestered CO_2 at some point after site closure.
- All six sectors of the CCS community representatives believe that cooperative federalism, where the federal government sets uniform standards and the states implement them, is the best approach for CCS regulation.

Further analysis of the survey results can be found in Davies et al. (2012, 2013).

Regulatory promotion

Policymakers have many options at their disposal to address the barriers identified in the survey. Often these options are lumped into a single category, referred to as "technology-forcing" regulation. A critical initial distinction, however, is in how policy seeks to "force" technology. For those technologies that are still nascent, "technology push" measures that seek to incentivize innovation and research and development investment tend to be the appropriate response. For technologies farther along the development spectrum, however, "market pull" policies that seek to deploy technologies commercially by creating greater demand for them should be the policy of choice. The survey results, plus recent assessments both by DOE and the EPA, make clear that CCS is such a technology. It is ready for deployment now, and thus the policy of choice should be some brand of “market pull” measure.

Of the various available “market pull” or “technology diffusion” policies, the investigators’ analysis shows that whatever is chosen for CCS must bear two characteristics. First, it should be CCS-specific, so that it clearly aims to promote CCS itself rather than any type of climate mitigation technology. Second, it should maintain flexibility, so that industry is not compelled to employ one certain brand or type of CCS technology. In all likelihood, this means a technology performance standard should be used, in very much the same way EPA proposes. However, a market-based regime also could be used, so long as it remains CCS-specific in a meaningful way, such as solar “carve out” provisions are currently used in state renewable portfolio standards. Our conclusion in this regard comports with the survey results, a mathematical study modeling CCS policies, and prior performance of technology forcing regulation in other areas.

Another important observation is that a “market pull” policy for CCS alone will not be sufficient. While the CCS community very much supports governmental incentives for CCS, four are specifically believed to be most effective in spurring diffusion of CCS technology: carbon pricing; caps on liability arising from CCS; economic incentives for CCS deployment; and a comprehensive CCS regulatory scheme. The survey results also demonstrate a CCS community preference for tax incentives, such as production tax credits, over alternative economic supports, such as technological mandates, CCS subsidies, and R&D funding. Thus, at a minimum, a technology performance standard for CCS should be combined with a comprehensive regulatory regime and liability limits if government is serious about promoting the technology. Other options, such as adoption subsidies or tax credits, might also be considered.

EPA has opted to utilize a performance standard in its recent proposed mandate of partial CCS. While EPA’s regulatory model may be legally feasible, it is unclear how EPA’s proposed NSPS would succeed in addressing the questions of carbon pricing and liability. Further, an EPA-mandated emissions standard standing alone constitutes neither a holistic nor a cooperative federalist regulatory framework for CCS.

Further discussion of regulatory promotion can be found in Davies et al. (2014).

Task 9 – Validation/Uncertainty Quantification for Large Eddy Simulations of the Heat Flux in the Tangentially Fired Oxy-Coal Alstom Boiler Simulation Facility

Additional details of the results for this task can be found in Smith et al. (2014).

Subtask 9.1 – LES Simulation and V/UQ for Heat Flux in Alstom Oxy-coal-Fired BSF

Predictions of time-averaged temperature and heat flux were compared with the measured data. Figure 39 shows the comparison between the heat flux measured with a suction probe and the time-averaged temperature with LES simulation for the standard case. In Figure 39(a), measured temperatures near the wall are 300K lower than the predicted data. The reason is due to the water jacket’s wall cooling effects in the near probe region, where LES does not consider such detailed geometries. Fortunately, comparisons at all other ports show that LES simulation predicts heat flux close to the measured data.

The simulations results show that the temperature on a plane is generally evenly distributed for the same height above the burner region. For example, the maximum temperature difference through Plane-141 is only 202K, while the maximum temperature difference through Plane-273 is no more than 100K. The predictions show that the temperature profile exhibits an apparent tangential flame region, where the highest temperature appears. However, the measured data shows that the highest temperature is generally in the central region of the furnace, and the temperature is even distributed especially at Plane-273. Such difference reveals that CFD simulation may over predict the centrifugal force in the furnace. The possible reason is that the burner structure in the simulation is simplified compared to the real burner design. Fortunately, the predictions still agree well with the measurements.

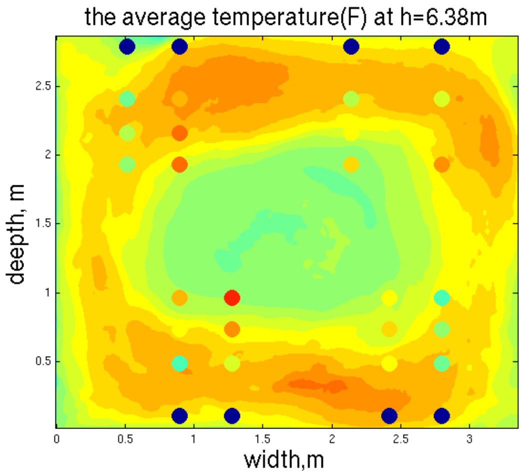

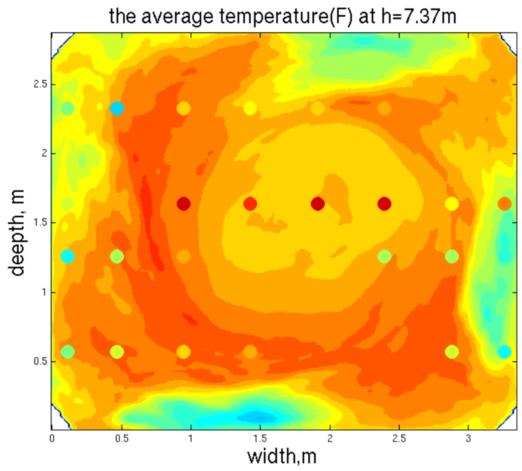

-
- (a) Plane 141 (b) Plane 180

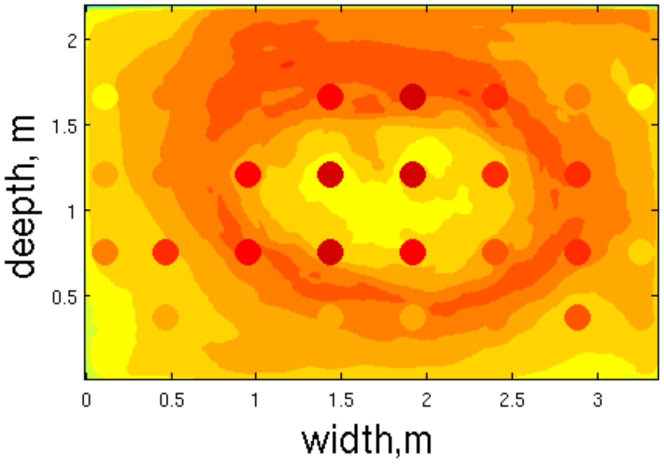

-
- (c) Plane 273

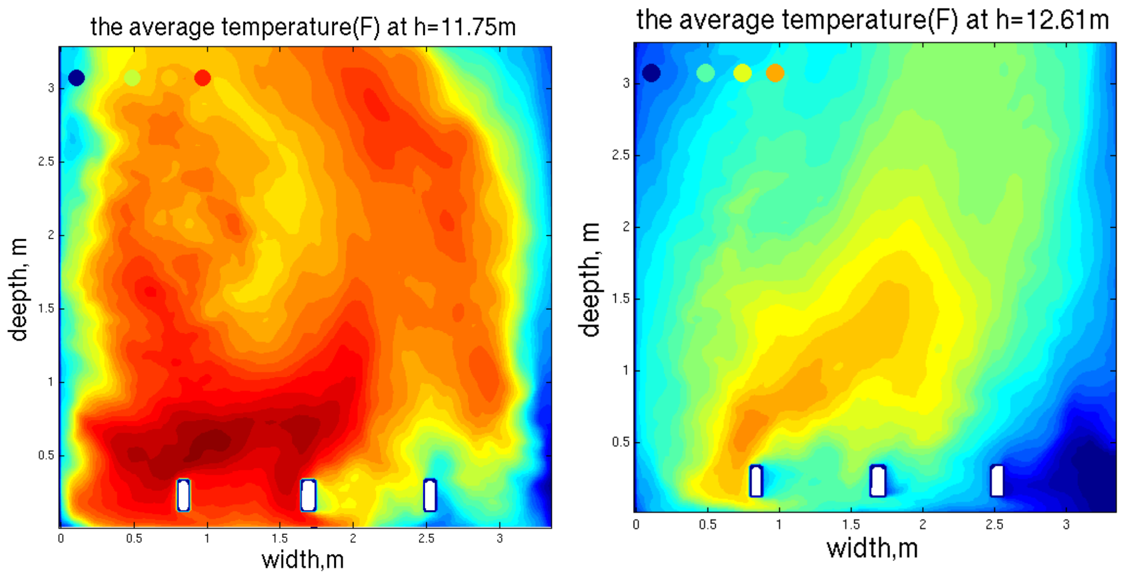

-
- (d) Plane 380 (e) Plane 464

Figure 39. Measured temperature vs. predicted temperature at different heights.

Figure 40 shows the comparison of all measured temperatures among the measured data and the predicted data under different thermal conductivities. This figure presents normalized temperatures. The standard deviation of the measured temperature is ± 4%. As k increases, predicted temperature drops quickly at all measurement ports. When *k* increases from 2.6 W/(m-K) to 4.33 W/(m-K), the temperature difference is in the range of 90~110K. This indicates that the wall thermal boundary conditions have a strong effect on temperature.

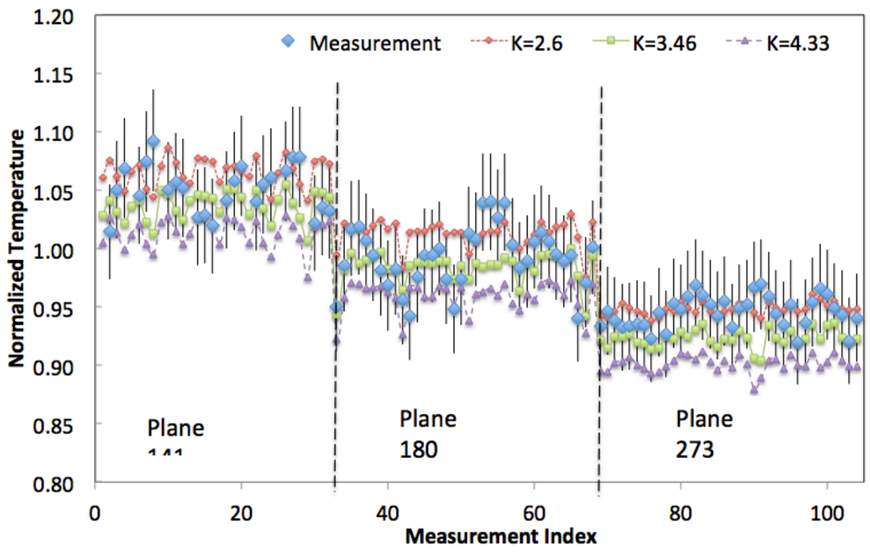

-

Figure 40. *k* effects of main furnace on temperature prediction.

-

The term *k* in the main furnace also has a strong effect on heat flux to the wall.

Figure 41 shows the normalized plane-averaged temperature change along boiler heights under different wall thermal boundary conditions. In the test case (*k*=test), the main furnace thermal conductivity is k=4.2

W/(m-K), while the upper furnace thermal conductivity is only half of the value that is adopted in the standard case. Comparing with the red dashed line (*k*=test) and black solid line (*k*=4.33), the only difference appears at the upper furnace region. This comparison shows that the thermal boundary conditions of the upper furnace only affect temperature in the upper furnace region but have no effects on temperature in the main furnace region.

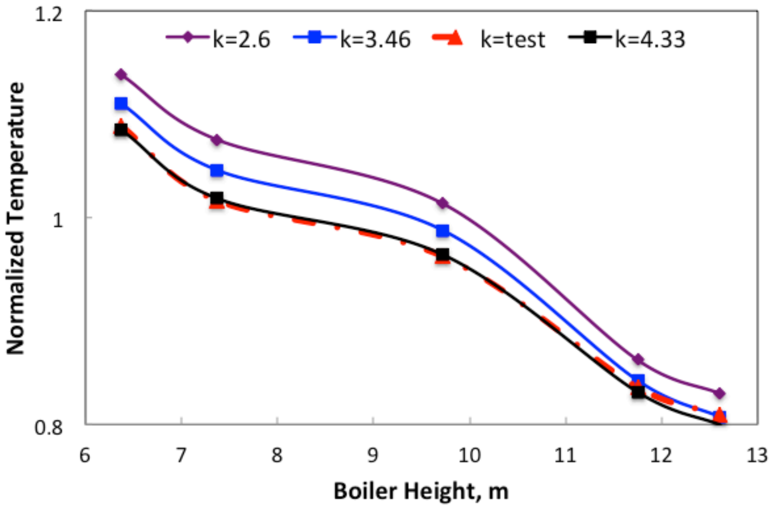

•

Figure 41. *k* effects of upper wall furnace on heat flux prediction

Volume rendered images of heat flux in the BSF is shown in Figure 42.

Effect of particle size

This distribution of Stokes Numbers as a function of particle size and eddy size results in a segregation of particles in the pulverized coal boiler. HPC with LES can capture this effect.

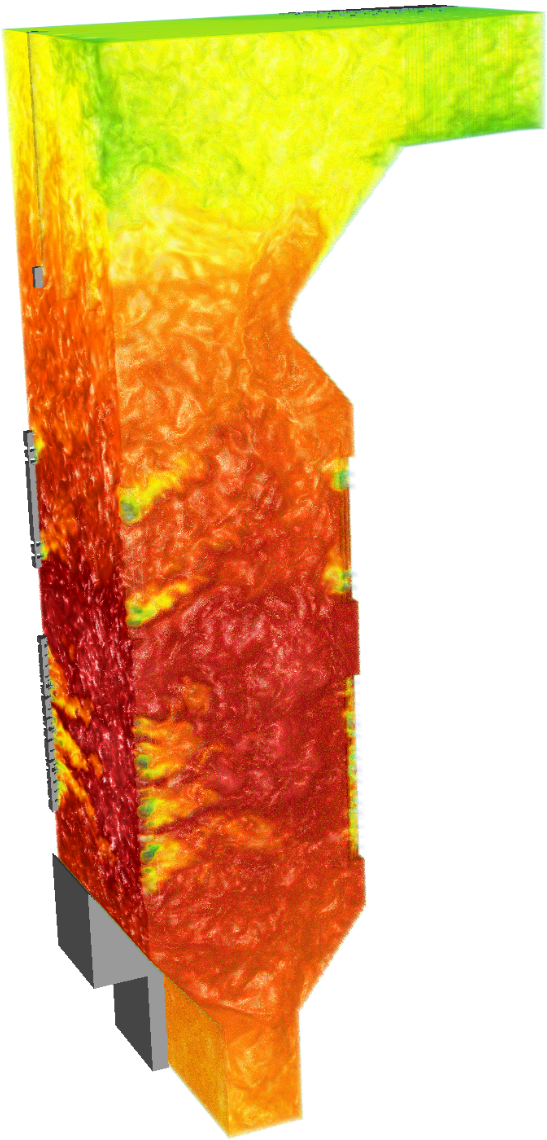

Figure 42. Volume rendered image of the local heat flux field in the BSF simulation.

V/UQ results

This formal V/UQ produces uncertainty bounds on the observed QOI (the measurements) that could not be achieved without concurrent simulation and validation. The information gain from this analysis is shown for heat flux in Figure 43.

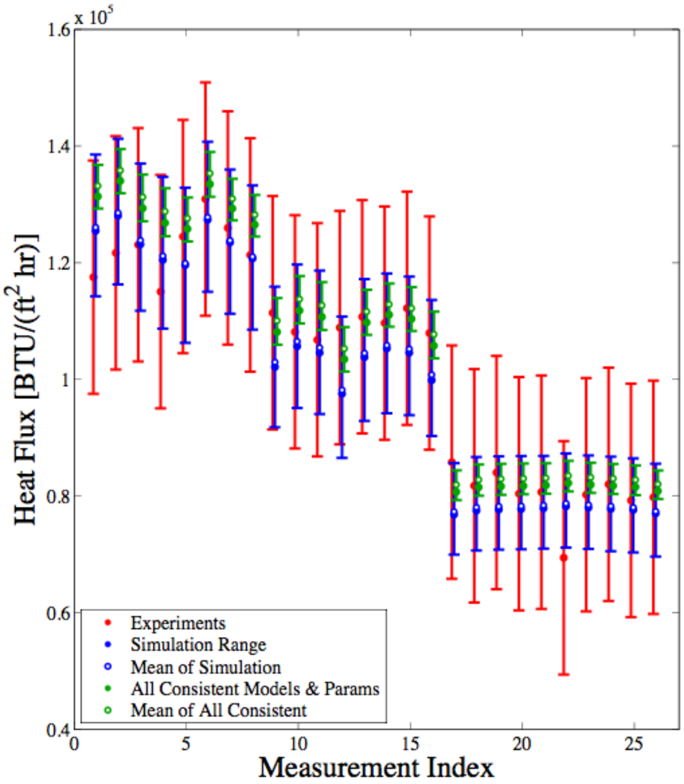

Figure 43. Validation from Alstom BSF experiments for heat flux with uncertainty before and after simultaneous consistency between heat flux, temperature and oxygen experimental data and LES simulation data.

For the heat flux measurements, the simulation (blue) error bars are largely encompassed within the experimental (red) error bars, so that the consistency band (green) is closer to the central portion of the experimental error bars for most of the measurement port locations. The initial experimental uncertainty for the heat flux was estimated to be +/- 6.3x10^4 W/m^2 (or +/- 2.0x10^4 Btu/hr-ft^2), and that value was apparently deemed reasonable and appropriate to ensure the existence of a consistency region.

Rather than use averaged planar temperatures in the overall consistency analysis, the next step in complexity was to increase the number of individual data set units by using all of the local temperature data (available at 104 measurement locations on levels L1, L2 and L3) instead of the averaged planar data. The incident heat flux data (available at 26 ports) was retained in the analysis. A consistency analysis was performed on all of the point-wise data (simultaneously). In order to achieve consistency using all of the temperature data, the temperature error bars had to be+/- 600 K. This degree of error was deemed unreasonable. Examining the data, we first eliminated all data points that were at least 500 K lower than the body of the data. On Plane L1, there are 8 points near the front and rear walls that exhibit very low temperatures; this is presumably due to ambient cold air leaking through the measurement ports. These low-temperature data points are not mutually consistent with the rest of the data (planar and local temperature, heat flux and oxygen concentration) and thus were determined to be outliers / bad data. In this way a total of 93 temperature points (out of the available 104 points) were determined to be consistent.

The V/UQ analysis made it possible to identify a few oxygen data points which were inconsistent with all measurements and simulations. In other words, since the thermal conductivity is the only active variable in this study, other active variables may also have a significant impact on the oxygen at L1. The data deemed to be "inconsistent" in the present analysis, may be found to be mutually consistent when other active variables are appropriately accounted for.

Subtask 9.2 – LES Simulation and V/UQ for Heat Flux in Subscale UofU Oxy-coal-Fired OFC

An initial base case (referred to as Case 1) was created using all of the geometric specifications and the boundary conditions mentioned in the Methods Section for this subtask. The thermal conductivity was selected as the QOI for this case. A best guess for the thermal conductivity of the walls was determined by modeling the 1D heat transfer through the walls of the system, given a typical incoming flux, and average outside wall temperature of 355 K.

The simulation was run for ~150,000 cpu hours resulting in 10.4 simulated seconds in order to reach steady state. Figure 44 shows the temperature and density profiles through the interior of the OFC reactor near 10 seconds of simulated time. It is clear from the images that the simulation predicts a substantial flame standoff distance, which is consistent with the experimental results. The image of density shows the dense purge streams flowing downwards along the sidewall of the reactor. Video rendering of the density field shows that a large recirculation zone forms within the burner. This recirculation zone tends upward on the side opposite the radiometers and downward on the side of the radiometers being dragged by the radiometers purge CO_2 gas. Figure 45 shows the inner-wall temperatures within the reactor. In general temperatures near 1000 K are observed. Figure 46 shows the raw coal mass as well as the char mass in the reactor.

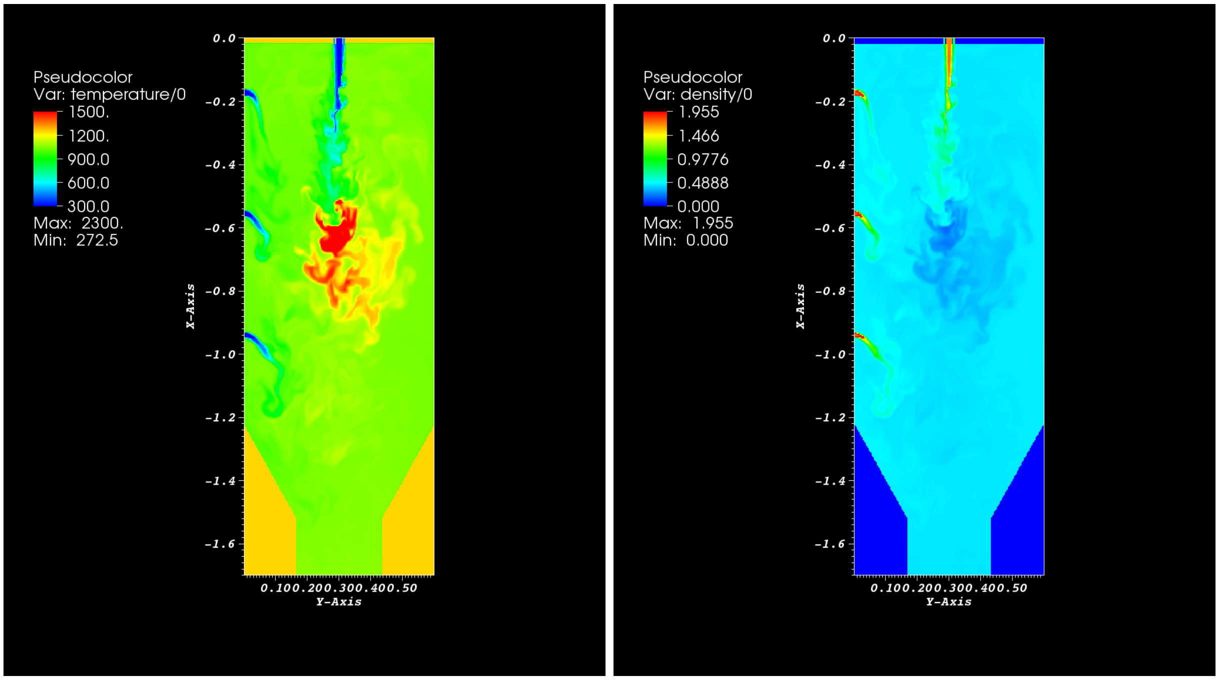

Figure 44. Temperature profile through the interior of the OFC burner.

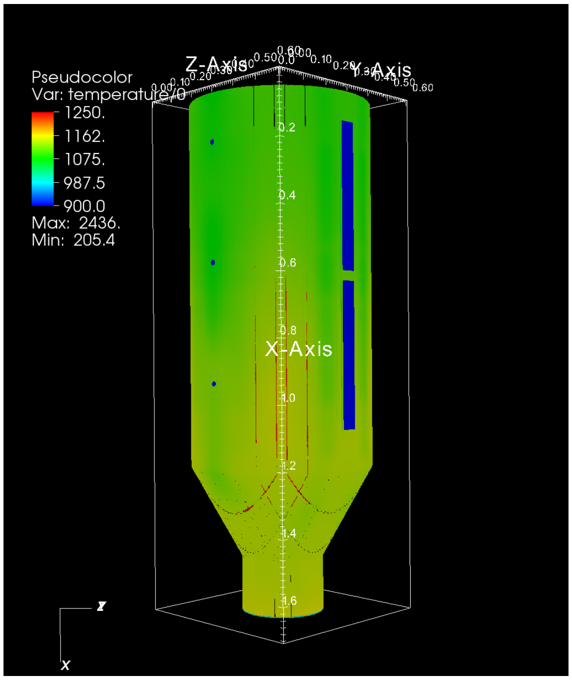

Figure 45. Shell temperature of the reactor.

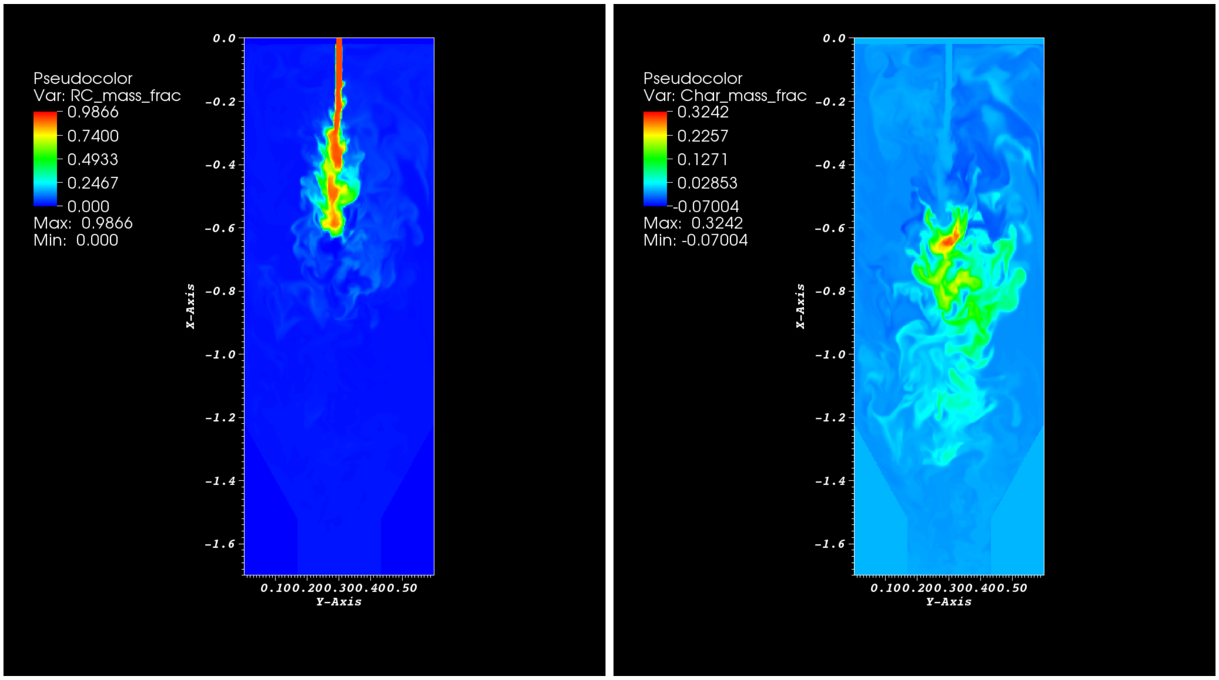

Figure 46. Raw coal mass and char mass profiles through the interior of the OFC burner.

Table 15 shows a comparison of the mean experimental measurements with the values obtained from Case 1. When looking at the QOI the predicted heat flux is very low. Accordingly, an initial sensitivity analysis was performed in order to assess the sensitivity of the thermal conductivity and make an educated guess on the range of thermal conductivity that may be interesting to investigate for the V/UQ analysis.

Table 15. Experimental measurements vs. Case 1 summary.

Location	Variable	Experiment	Case 1
Port 1	Heat Flux [W/(mK)]	53	31
Port 2	Heat Flux [W/(mK)]	72	36
Port 3	Heat Flux [W/(mK)]	58	39
Window	Temperature [K]	1499	1290

V/UQ analysis

After investigating sensitivity of the thermal conductivity in the walls and the shell side temperature for the windows, four cases were run on the University of Utah's supercomputer, Ash, in order to better understand, and quantify the uncertainty in the thermal boundary parameters of the system. Each case required over 130,000 cpu hours.

A consistency analysis was done based on the four cases for the heat flux. Figure 47 shows the results for the consistency analysis for heat flux. The blue marker give the mean value for the simulation, and the blue bars are bound by the upper and lower values found from the various cases that were run. The red marker gives the experimental mean, and the red bars show the range of uncertainty based on the posterior estimate of the uncertainty as given by Bayes theorem. The green bar shows the region of consistency that was found. The green marker shows the most consistent value within the bounds of consistency.

These results show that simultaneous consistency was achieved over the three heat flux measurements. Over a range of 0.1 to 0.2 W/(mK) for the thermal conductivity in the walls consistency was met, while varying the shell temperature on the outside of the windows from 1050-1125 Kelvin. It appears that better consistency is met with the largest value of thermal conductivity and the largest value for the outside shell temperature. These results give good insight into what values should be used for these uncertain parameters in order to better predict the simulation results. Although the results here showed consistency for the given ranges of experimental error, it is clear that other model or scenario parameters need to be changed in order to achieve better consistency.

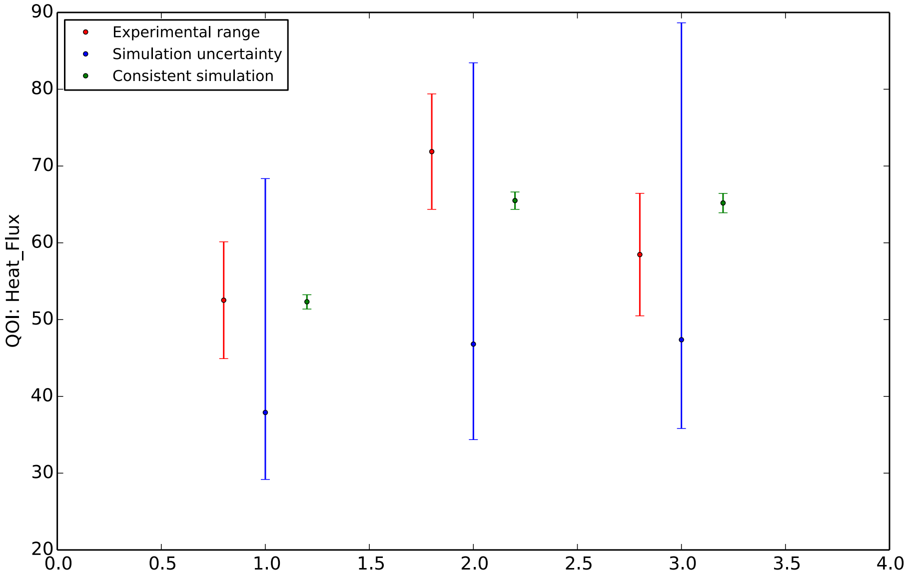

Figure 47. Heat Flux results from V/UQ analysis.

CONCLUSIONS

The conclusions are organized by task.

Oxycoal studies:

- LES can resolve turbulence effects directly and can lead to more accurate simulations than traditional RANS methods. In addition, the consistency analysis revealed consistency between the simulation and experimental OFC results. The simulations were consistent with the experimental data but did not predict any sensitivity to the primary P_{O2}. These results do not agree with experimental results described by Wendt et al. (2009).
- The investigators determined that the steam and CO_2 gasification reactions are important processes during oxy- and conventional combustion, but neglecting gas-phase reactions is an acceptable approximation. In addition, the kinetic model developed by the investigators showed that the sub-bituminous coal char was more reactive than the two bituminous coal chars. The model and experiments also highlighted the fact that both bituminous coal chars have similar combustion behaviors and the combustion characteristics can be well approximated using one set of kinetic parameters.
- The experimental studies in the OFC found that subtle variations in coal composition had a significant effect on coal ignition, and this was supported by TGA studies. In addition, it is possible to support axial turbulent diffusion oxy-coal flames using streams of pure, directed oxygen. Furthermore the pure oxygen stream should be introduced through the inner annulus of a triple concentric burner, rather than in the center.
- The oxy-CFB studies found no difference in SO_2 emissions between oxy- and air-fired combustion in the bench-scale BFB. In contrast, for the pilot-scale CFB, the SO_2 emissions were

substantially higher under the oxy-fired conditions in terms of concentration, but were slightly lower than air-fired conditions in terms of mass-based emissions. The reason for the higher SO_2 concentrations during oxy-firing at pilot-scale were due to the use of flue-gas recycle, which allowed accumulation of sulfur species in the main combustion zone. The single-particle CFB studies found that under air-firing conditions, the limestone sulfation rate was not strongly affected by temperature. In contrast, under oxy-firing conditions, the presence of CO_2 suppresses limestone decomposition and the limestone sulfation displays notable temperature dependence, indicating that the reaction is more kinetically controlled.

- The ash partitioning subtask found that temperature was the driving mechanism for increasing the amount of ultrafine formation with an increase in mass at higher temperatures. For fine particles, the temperature relationship was less pronounced. In addition, the OFC experiments showed that different RFG cleanup options did not affect PSDs. However, different RFG amounts had a significant effect on both PSDs and aerosol elemental chemistry.

Gasification studies:

- The LES simulations revealed that the gasification of coal is close to equilibrium and the equilibrium assumption is reasonable although the carbon conversion is low. The single-particle simulation studies showed that increased initial furnace temperature decreases the ignition delay, which matched experimental observations. Furthermore, studies on the impact of particle size on ignition phase revealed that decreasing the particle size shifts the phase of ignition from homogenous to heterogeneous. The RMCRT model for radiation allowed for the computation of radiative flux divergences, fluxes to boundary surfaces, interior surfaces, and surfaces with arbitrary view angles and orientations. Good agreement between benchmark solutions and computed solutions was obtained. In addition, the RMCRT model scaled well in parallel.
- Good agreement between measured and modeled mass release was obtained for Illinois #6 coal char when using a first-order model and regressed kinetic parameters. The EFG studies focused on improving fuel atomization, and the investigators developed a system, which was able to provide more stable performance. The EFG also provided several data sets for validation of computational simulation models. The data sets included gas composition extracted at three radial positions. Replicate samples at the same position showed good repeatability of syngas composition measurement. Little variation in composition between the centerline and near-wall region was observed, suggesting that the reactor experiences relatively little internal recirculation.

CLC studies:

- Comparing the process model results of CLOU with those of CLC employing an iron-based oxygen carrier revealed that the CLOU process has the potential to reduce reactor size and oxygen carrier inventory. As copper-based oxygen carriers cost significantly more than iron-based oxygen carriers, the lifetime of the oxygen carrier is the key factor for developing CLOU technology.
- The high-performance simulations compared favorably with experimental BFB behavior. They were able to capture the transition of the stationary bed into the fluidized regime and replicate proper behavior of the bed as a function of bed height and superficial bed velocity.

- The laboratory-scale studies determined that both oxidation and decomposition (O_2 release) of the copper oxygen carrier depend on the so-called “driving force” associated with the difference between the O_2 partial pressure in the reactor environment and the equilibrium O_2 partial pressure. In addition, the influence of Cu_2O concentration (degree of conversion) was analyzed and found to best be modeled by considering two regimes, a low temperature regime in which the rate at high conversion slows due to pore blocking and a high temperature regime (>700°C) which is best modeled by considering grain nucleation and growth. Finally, the reaction order in oxygen driving force was concluded to be 1.3. The resulting models reasonably describe oxidation of copper-based oxygen carriers.
- CLC kinetics team developed kinetic data for various supported copper material and found that the samples prepared by the coat and bake method on silicon carbide provided good copper loading and performed well in TGA and fluidized-bed experiments.

The UCTT studies:

- The experimental studies revealed that the most important factor in predicting product yield is final temperature. Higher final temperatures, ranging from 500 – 600°C produced yields in the range of 20 – 28%. Despite the large difference in scale, the FBR and RBR yield and composition results agree reasonably well. The effect of pressure was not as pronounced as the effect of temperature, and the results were somewhat inconclusive. The carbon in the UCTT products tended to partition to the char, while the hydrogen tended to partition to the gas and liquid-phase products.
- The simulation studies showed the importance of the yield model and heater temperature.
- The CO_2 storage capacity of UCTT-treated coals declined for coals treated to 325°C, compared to the untreated coals. Above these temperatures adsorptive capacity generally increased with treatment temperature.

Mercury studies:

- In the absence of sulfur dioxide, the oxy-firing environment caused a remarkable increase in oxidation of mercury by chlorine. The presence of 500 ppm SO_2 caused a dramatic decline in the levels of oxidation at all oxy-fired conditions examined. Similar effects of SO_2 have been noted with air firing.

Policy studies:

- There have been great advances in the technology, implementation, and legal and policy foundations for CCS in the United States at both the federal and regional levels over the past several years, but whether this technology becomes broadly accepted will depend on whether its costs can be reduced and how domestic energy policy evolves. This is supported by the results of the survey, which revealed that CCS community is predominantly concerned with cost/carbon pricing, liability, and a desire for comprehensive regulation.
- If government is to promote greater use of CCS as a climate mitigation measure, any policy adopted must address cost/carbon pricing, liability, and the desire for comprehensive regulation. In doing so, policymakers have many tools at their disposal to aid in policy diffusion. The

analysis suggests that whatever is chosen for CCS must bear two characteristics. First, it should be CCS-specific, so that it clearly aims to promote CCS itself rather than any type of climate mitigation technology. Second, it should maintain flexibility, so that industry is not compelled to employ one certain brand or type of CCS technology.

V/UQ for LES of the heat flux in the tangentially fired oxy-coal Alstom BSF:

- HPC of the BSF was able to resolve more of the physics and chemistry in the coal combustion boiler as well as to resolve more spatial and temporal time scales than previous boiler simulations. Simulations of the Alstom BSF using ~3000 processors allowed for spatial resolution of 1 to 2 cm and temporal resolution of ~10^{-6} seconds.
- The BSF simulation results demonstrated that LES can predict oxy-coal boiler performance (i.e., local temperature, heat flux, oxygen concentration) that is consistent with BSF measurements through formal V/UQ by using HPC with thousands of processors. Specifically, the heat flux measurements and predictions yielded an uncertainty of $\pm$ 1e4 W/m^2.
- The OFC experiments produced much more stable mass flow rates and reactor wall temperatures were much more than anticipated, and these data were used in the simulations. After correction, the MWIR camera and radiometer measurements agreed well. The OFC studies also revealed that burning coal under oxy-combustion conditions with no flue gas recycle, other than that required to transport the coal, is possible, and does not necessarily lead to extraordinary high radiant heat fluxes in the combustion chamber.

LIST OF PEER-REVIEWED PUBLICATIONS

J. Ahn, R. Okerlund, A. Fry, E. Eddings, "Sulfur trioxide formation during oxy-coal combustion”, International Journal of Greenhouse Gas Control, Vol. 5(S-1), 2011, S127-S135.

M.J. Bayarri, J.O. Berger, R. Paulo, et al. “ Computer Model Validation with Functional Output” *Technometrics*, 49, 2007, 138-154.

A. Biglari, J.C. Sutherland, "A filter-independent model identification technique for turbulent combustion modeling", Combustion & Flame, 159(5), 2012, 1960-1970.

C.K. Clayton, H.Y. Sohn, K.J. Whitty, “Oxidation kinetics of Cu2O in oxygen carriers for chemical looping with oxygen uncoupling”, Industrial & Engineering Chemistry Research, 53, 2014, 2976-2986.

C.K. Clayton, K.J. Whitty, “Measurement and modeling of decomposition kinetics for copper-based chemical looping with oxygen uncoupling", Applied Energy, 116, 2014, 416-423.

L.L. Davies, K. Uchitel, J. Ruple "Understanding barriers to commercial-scale carbon capture and sequestration in the United States." Energy Policy, 59, 2013, 745-761.

E.M. Eyring, G. Konya, J.S. Lighty, A.H. Sahir, A.F. Sarofim, K. Whitty, "Chemical looping with copper oxide as carrier and coal as fuel", Oil & Gas Science and Technology - Rev. IFP Energies nouvelles, 66(2), 2011, 209-221.

B. Goshayeshi, J. Sutherland, "A comparison of various models in predicting ignition delay in single-particle coal combustion", Combustion and Flame, 161, 2014, 1900-1910.

B. Goshayeshi, J. Sutherland, "Prediction of oxy-coal flame stand-off using high-fidelity thermochemical models and the one-dimensional turbulence model", Proceedings of the Combustion Institute, in press.

E.S. Hecht, C.R. Shaddix, M. Geier, A. Molina, B.S. Haynes, "Effect of CO2 and steam gasification reactions on the oxy-combustion of pulverized coal char", Combustion and Flame, 159(11), 2012, 3437-3447.

E.S. Hecht, C.R. Shaddix, J.S. Lighty, "Analysis of the errors associated with typical pulverized coal char combustion modeling: assumptions for oxy-fuel combustion", Combustion and Flame, 160(8), 2013, 1499-1509.

Y. Jia, J.S. Lighty, "Ash particulate formation from pulverized coal under oxy-fuel combustion conditions", Environmental Science & Technology, 46(9), 2012 5214-5221.

S. Li, Y. Wu, K. Whitty, "Ash deposition behavior during char-slag transition under simulated gasification conditions", Energy & Fuels, 24(3), 2010, 1868-1876.

P. Mandalaparty, M. Deo, J.N. Moore, “Gas-compositional effects on mineralogical reactions in carbon dioxide sequestration”, SPE Journal, 16(4), 2011, 949-958.

W.J. Morris, D. Yu, J.O.L. Wendt, “A comparison of soot, fine particle and sodium emissions for air-and-oxy-coal flames, with recycled flue gases of various compositions”, Proceedings of the Combustion Institute, 34(2), 2013, 3453-3461.

W.J. Morris, D. Yu, J.O.L. Wendt, “Soot, unburned carbon, and ultrafine particle emissions from air and oxy-coal flames”, Proceedings of the Combustion Institute, 33(2), 2011, 3415-3421.

A. Parente, J.C. Sutherland, B.B. Dally, L. Tognotti, P.J. Smith, "Investigation of the MILD combustion regime via principal component analysis", 33rd International Symposium on Combustion Beijing, China, August 1-6, 2010.

J. Pedel, J.N. Thornock, P.J. Smith, "Ignition of co-axial turbulent diffusion oxy-coal jet flames: experiments and simulations collaboration", Combustion & Flame, 160(6), 2013, 1112-1128.

J. Pedel, J.N. Thornock, P.J. Smith, "Large eddy simulation of pulverized coal jet flame ignition using the direct quadrature method of moments", Energy and Fuels, 26(11), 2012, 6686-6694.

S.B. Peterson, G. Konya, C.K. Clayton, R.J. Lewis, B.R. Wilde, E.M. Eyring, K.J. Whitty, "Characteristics and CLOU performance of a novel SiO2-supported oxygen carrier prepared from CuO and beta-SiC", Energy & Fuels, 27(10), 2013, 6040-6047.

N. Punati, J.C. Sutherland, A.R. Kerstein, E.R. Hawkes, J.H. Chen, "An evaluation of the one-dimensional turbulence model: comparison with direct numerical simulations of CO/H2 jets with extinction and reignition", Proceedings of the Combustion Institute, 331(1), 2010, 1515-1522.

D. Rezaei, Y. Zhou, J. Zhang, K.E. Kelly, E.G. Eddings, R.J. Pugmire, M.S. Solm, J.O.L. Wendt, "The effect of coal composition on ignition and flame stability in coaxial oxy-fuel turbulent diffusion flames", Energy and Fuels, 27, 2013, 4935-4945.

A.W. Retize Jr., "Federal control of carbon capture and storage", Environmental Law Reporter, 41(9), 2011, 10796-1082.

A.W. Reitze Jr., M.B. Durrant, "Control of geological carbon sequestration in the Western United States", Environmental Law Institute, 41(5), 2011, 10455.

A. W. Reitze Jr., M.B. Durrant, "State and regional control of geological carbon sequestration (Part I)", Environmental Law Reporter, 41(4), 2011, 10348-1037.

A.H. Sahir, J.K. Dansie, A.L. Cadore, J.S. Lighty, "A comparative process study of chemical-looping combustion (CLC) and chemical-looping with oxygen uncoupling (CLOU) for solid fuels", International Journal of Greenhouse Gas Control, 22, 2014, 237-243.

A.H. Sahir, H.Y. Sohn, H. Leion, J.S. Lighty, "Kinetics of copper oxidation in the air reactor of a chemical looping combustion system using the law of additive reaction times", Industrial and Engineering Chemistry Research, 50(23), 2011, 13330-13339.

A.H. Sahir, H.Y. Sohn, H. Leion, J.S. Lighty, "Rate analysis of chemical-looping with oxygen uncoupling (CLOU) for solid fuel", Energy and Fuels, 26(7), 2012, 4395-4404.

A. Sanchez, E.G. Eddings, F. Mondragon, "FTIR on line Monitoring of NO, N2O and CO2 during Oxygen-enriched Combustion of Carbonaceous Material", Energy and Fuels, 24(9), 2010, 4849-4853.

R.C. Shurtz, T.H. Fletcher, "Coal char-CO2 gasification measurements and modeling in a pressurized flat-flame burner", Energy and Fuels, 27, 2013, 3022-3038A.

R.C. Shurtz, J.W. Hogge, K.C. Fowers, G.S. Sorensen, T.H. Fletcher, "Coal swelling model for pressurized high particle heating rate pyrolysis applications", Energy and Fuels, 26(6), 2012, 3612-3627.

P. Toth, Z. Zhan, Z. Fu, A. Palotas, E. Eddings, T. Ring, "Optical flow velocimetry for the real-time monitoring and control of luminous flames"' Experiments in Fluids, 55, 2014, 1727.

Y. Wu, P.J. Smith, J. Zhang, J.N. Thornock, G. Yue, "Effects of turbulent mixing and controlling mechanisms in an entrained flow coal gasifier", Energy & Fuels, 24(2), 2010, 1170-1175.

J. Zhang, K.E. Kelly, E.G. Eddings, J.O.L. Wendt, "CO2 effects on near field aerodynamic phenomena in 40 kW, co-axial, oxy-coal, turbulent diffusion flames", International Journal of Greenhouse Gas Control, 5(1), 2011, S47-S57.

J. Zhang, K.E. Kelly, E.G. Eddings, J.O.L. Wendt, "Ignition in 40 kW co-axial turbulent diffusion oxy-coal jet flames", Procedings of the Combustion Institute, 33(2) 2011, 3375-3382.

Z. Zhan, A. Fry, Y. Zhang, J.O.L. Wendt, "Ash aerosol formation from oxy-coal combustion and its relation to ash deposit chemistry", Proceedings of the Combustion Institute, in press.

REFERENCES

P.A. Buitrago, G.D. Silcox, C. L. Senior, The Effects of Oxy-firing Conditions on Gas-phase Mercury Oxidation by Chlorine and Bromine, Topical Report, 2010. Available at: http://repository.icse.utah.edu/dspace/handle/123456789/11006

L.L. Davies, K. Uchitel, J. Ruple, H. Tanana (2012) Carbon Capture and Sequestration: A Regulatory Gap Assessment. Topical Report, April 2012. Available at: http://www.uc3.utah.edu/assets/for_download/pdfs/CCSFinalReportApril2012.pdf

L.L. Davies, K. Uchitel, J. Ruple "Understanding barriers to commercial-scale carbon capture and sequestration in the United States." Energy Policy, 59, 2013, 745-761, July 2013. Available at: http://www.sciencedirect.com/science/article/pii/S0301421513002838

L.L. Davies, K. Uchitel, D. Johnson "Regulatory Promotion of Emergent CCS Technology". Topical Report, January 2014. Available at: http://www.uc3.utah.edu/assets/for_download/pdfs/RegulatoryPromotionofEmergentCCSTechnology.pdf

A.W. Reitze Jr., (2011a) Federal Control of Geological Carbon Sequestration Topical Report. Available at: http://repository.icse.utah.edu/dspace/handle/123456789/11058

A.W. Reitze Jr., "Federal Control of Carbon Capture and Storage", Environmental Law Reporter, 41(9), 2011b, 10796-1082. Available at: http://repository.icse.utah.edu/dspace/handle/123456789/11102

A.W. Reitze Jr., M.B. Durrant, "Control of Geological Carbon Sequestration in the Western United States", Environmental Law Institute, 41(5), 2011a, 10455. Available at: http://elr.info/news-analysis/41/10455/control-geological-carbon-sequestration-western-united-states

A. W. Reitze Jr., M.B. Durrant, "State and regional control of geological carbon sequestration (Part I)", Environmental Law Reporter, 41(4), 2011b, 10348-1037. Available at: http://elr.info/news-analysis/41/10348/state-and-regional-control-geological-carbon-sequestration-part-1

A.W. Reitze, Jr., M.B. Durrant, (2011c) State and Regional Control of Geological Carbon Sequestration, Topical Report March 2011. Available at: http://repository.icse.utah.edu/dspace/handle/123456789/11093

A.F. Sarofim, J.S. Lighty, P.J. Smith, K.J. Whitty, E. Eyring, A. Sahir, M. Alvarez, M. Hradisky, C. Clayton, G. Konya, R. Baraki, K. Kelly, Chemical Looping Combustion Reactions and Systems, Task 5 Topical Report, March 2014. Available at: http://content.lib.utah.edu/utils/getfile/collection/ir-eua/id/3116/filename/3117.pdf

A.F. Sarofim, J.S. Lighty, P.J. Smith, K.J. Whitty, E. Eyring, A. Sahir, M. Alvarez, M. Hradisky, C. Clayton, G. Konya, R. Baraki, and K. Kelly, Chemical Looping Combustion Reactions and Systems, Task 5 Topical Report, August 2011. Available at: http://repository.icse.utah.edu/dspace/handle/123456789/11092

P.J. Smith, E.G. Eddings, T. Ring J. Thornock, T. Draper, B. Isaac, D. Rezeai, P. Toth, Y. Wu, K. Kelly, Validation/Uncertainty Quantification for Large Eddy Simulations of the Heat Flux in the Tangentially Fired Oxy-Coal Alstom Boiler Simulation Facility, Task 9 Topical Report, October 2014. Available at: http://www.osti.gov/scitech/servlets/purl/1163847

P.J. Smith, M. Deo, E.G. Eddings, M. Hradisky, K.E. Kelly, R. Krumm, Adel F. Sarofim, D. Wang, Underground Coal Thermal Treatment, Task 6 Topical Report, January 2015.

J.O.L. Wendt, E.G. Eddings, J.S. Lighty, T. Ring, P.J. Smith, J. Thornock, Y. Jia, W. Morris, J. Pedel, D. Rezeai, L. Wang, J. Zhang, K. Kelly, Oxy-coal Combustion Studies, Task 3 Topical Report, July 2011. Available at: http://www.osti.gov/scitech/servlets/purl/1045472/

J.O.L. Wendt, E.G. Eddings, J.S. Lighty, T. Ring, P.J. Smith, J. Thornock, E. Hecht, J. Pedel, D. Rezeai, L. Wang, P. Toth, Z. Zhan, K. Kelly, Oxy-coal Combustion Studies, Task 3 Topical Report, August 2014. Available at: http://www.uc3.utah.edu/assets/for_download/pdfs/OxycoalTopicalReport.pdf

K. Whitty, T. Fletcher, R. Pugmire, P. Smith, J. Sutherland, J. Thornock, I. Hunsaker, S. Li, K. Kelly, N. Punati, C. Reid, and R. Schurtz, Gasification Studies, Task 4 Topical Report, October 2011. Available at: http://repository.icse.utah.edu/dspace/bitstream/123456789/11105/1/gasification_final_oct10_2011.pdf

K. Whitty, T. Fletcher, R. Pugmire, P. Smith, J. Sutherland, J. Thornock, B. Goshayeshi, I. Hunsaker, A. Lewis, T. Waind, and K. Kelly, Gasification Studies, Task 4 Topical Report, February 2014. Available at: http://content.lib.utah.edu/utils/getfile/collection/ir-eua/id/3117/filename/3118.pdf